Università degli Studi di Cagliari

PhD DEGREE

Civil Engineering and Architecture

Cycle XXXIII

TITLE OF THE PHD THESIS

Stochastic inversion of time domain electromagnetic data with non-trivial prior

Scientific Disciplinary Sector(s)

GEO/11

PhD Student:	Peng Bai
Supervisor	Prof. Giulio Vignoli
Co-Supervisors	Prof. Thomas Mejer Hansen Prof. Andrea Viezzoli

Final exam. Academic Year 2019/2020

Thesis defence: February 2022 Session

Abstract

Inversion deals with inferring information about the subsurface (by reconstructing its physical properties), given: 1) observed data (usually collected at the surface) and 2) available forward modelling tools (describing physics of the used geophysical methodology). Inevitably, these forward modelling tools are always characterized by some level of approximation, and, in turn, this inaccuracy, unavoidably, affects the inversion results. This thesis presents, in particular in the context of airborne electromagnetic data, the impact and relevance of quantifying this source of (coherent) error. Specifically, a possible strategy to quantify the modelling error is discussed in the thesis.

The adopted strategy for the estimation of the modelling error makes use of prior knowledge about the investigated system. The same prior knowledge is necessary in stochastic inversion frameworks. Stochastic inversion provides a natural way for 1) the assessment of the uncertainty of the final results and 2) for incorporating complex prior information into the inversion, from sources that are not the geophysical observations. Since the assessment of the modelling error is based on prior information that is also used in the stochastic inversion approaches, it is a natural choice to adopt these probabilistic strategies.

By taking into account the modeling error, the stochastic inversions can eliminate or, at least, minimize, the effects of the forward approximation in the inversion results. In this thesis, through synthetic and field tests, we discuss the stochastic inversion considering the modeling error.

What is called prior in the framework of stochastic inversion is assimilable to the training dataset in the context of Neural Networks: to some extent, in both cases, the final solution is by construction “stationary” with respect to the initially provided ensemble used to feed (or train) the inversion algorithm. Based also on these premises, and in the attempt to find a way to address the “definitive” problem of a fully 3D stochastic inversion, we verify the possibility of extremely efficient Neural Network strategy for the inversion of massive airborne geophysical datasets. Some preliminary, but, still, very promising results on this matter are discussed in the second last chapter of this thesis. Also in this case, the conclusions are drawn based on synthetic and experimental data.

Keyword: inversion, modeling error, stochastic, neural network.

Content

Thesis outline

Chapter 1: For the inversion of the large airborne geophysical datasets, deterministic approaches are usually considered the standard strategies; this despite extremely efficient stochastic algorithms are available. In Chapter 1, we briefly discuss different inversion approaches in which the modelling error estimation will be, later on, incorporated.

Chapter 2: We discuss a possible way to quantify the modelling error caused by forward modelling approximation, and to incorporate this estimated modeling error into a stochastic framework. Synthetic and field tests are performed and the results and the inversion parameters are discussed.

Chapter 3: Motivated by the correspondence between the concepts of prior distribution and training dataset, we implemented a Neural Network inversion scheme for airborne electromagnetic data inversion. The discussed approach provides geophysical models that are largely compatible with the outputs of state-of-the-art full-nonlinear 1D deterministic inversions. But the Neural Network results can be obtained in seconds rather than in hours (as in the deterministic case).

Chapter 4: Conclusions about the stochastic inversion incorporating modeling error and the Neural Network approach are summarized and discussed.

Chapter 1. Introduction

1.1. Airborne Electromagnetics overview

Airborne electromagnetic (AEM) technology was originally developed for the mining industry where it continues to be used extensively. There is no need for the transmitter or the receiver to touch the ground, so electromagnetic systems can be mounted on aircraft and used to cover large areas quickly and efficiently. For this reason, airborne electromagnetic surveys could provide high-density data economically over large areas. Because of these big advantages, AEM methods are also used in geological and groundwater mapping, and environmental investigations..

AEM techniques have been used in the industry for more than seven decades. The early systems were utilized in Canada in the early 1950s and were firstly used for the prospection of base metal deposits (Palacky, 1993). During the last years, AEM applications have started to increasingly move towards also environmental investigations (for example, groundwater mapping). Because of the dependency of the conductivity on both the lithology and the salinity of the water, AEM methods could potentially provide useful information about the water quality and aquifer structures (Siemon et al., 2009). The earliest tests concerning the hydrogeological investigations via AEM systems can be traced back to 1978, on the island of Spiekeroog, Germany, using an early Helicopter-borne electromagnetic (HEM) system operated by the German Federal Institute for Geosciences and Natural Resources (BGR) (Siemon et al., 2009). Other examples of groundwater studies via AEM systems are documented in Paterson and Bosschart (1987), Sengpiel and Fluche (1992). The review paper Paine and Minty (2005) discusses further applications and examples of AEM data collections.

AEM theory is based on Faraday's law of induction: a current can be induced to flow by a changing magnetic field and vice versa. Based on this, time-domain AEM systems generate a primary time-varying EM field via a time-dependent current flowing in the transmitting loop. In turn, the time-varying EM field generates eddy currents in the subsurface. These eddy currents cause a secondary electromagnetic (EM) field, which can be detected by the receiver coils of the AEM systems (Figure 1-1). The primary EM field can be caused by "pulse" or more complex current waveforms (Karshakov et al., 2017; Moilanen et al., 2013; Palacky, 1993; Volkovitsky and Karshakov, 2013). The secondary field can be recorded in frequency-domain (over several frequencies) or in time-domain (tens of time-gates, generally after the shutdown of the transmitter current). The secondary field response clearly depends (mainly) on the subsurface conductivity. Hence, the secondary field measurements can be used to infer the underground electrical property distribution. For example, the secondary responses of good conductors decay slowly, whereas their decay over resistivity bodies can be extremely fast.

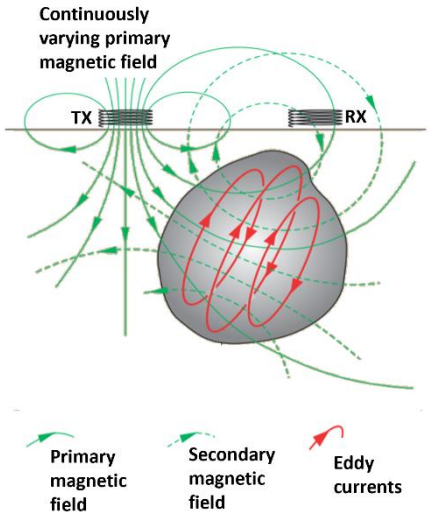

Figure 1-1 Schematic illustration of the principles of electromagnetic surveys: the chances in the primary field induce eddy currents in the conductors in the subsurface; the eddy currents, in turn, generate a secondary magnetic field whose evolution is recorded by the receiver coil.

AEM exploration consists of three phases: data collection, data processing and, finally, inversion. Despite the common practice of a purely sequential implementation, these three phases of the translation of the raw measurements into physical property distribution should be iterative (Dzikunoo et al., 2020). During the data collection, the aircraft is equipped with a coil that is suspended below it (Figure 1-2) or that is running from nose to wingtips to tail (Figure 1-3), through which, the electrical current is made flowing. The secondary EM field measurements are collected by a receiver located on the transmitting loop (Figure 1-2) or towed behind the aircraft (Figure 1-3) along the flight lines.

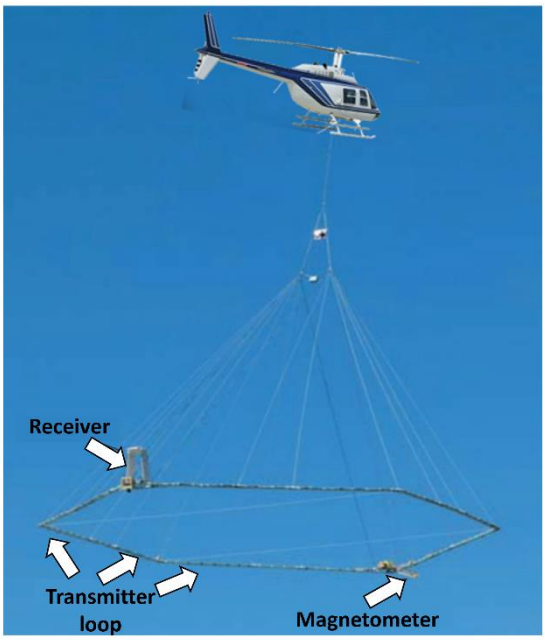

Figure 1-2 The aircrafts equiped with a coil draw below it (Dentith and Mudge, 2014).

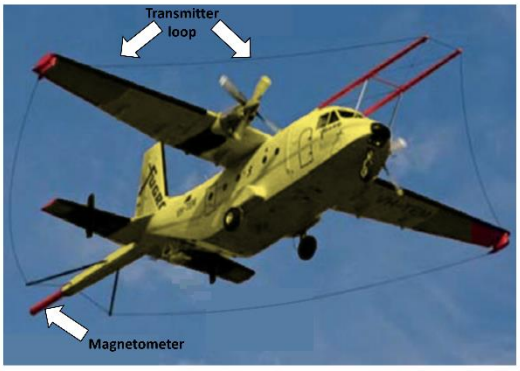

Figure 1-3 The aircraft equiped with a coil running from nose to wingtips to tail (Dentith and Mudge, 2014).

After the data collection in the field, the raw data not only include the information of the subsurface, but, in general, also anthropic noise produced by, for example, power lines, pipes, metal fences, windmills. Thus, the data processing procedure is indispensable – especially, in populated areas – to eliminate or, at least, to minimize, the noise effects and to obtain good quality data effectively representative of the earth conditions. In general, data processing includes four steps: navigation data (GPS, altitude and tilt measurements) processing; voltage data processing; further refinement of voltage data; and a fast, preliminary, inversion (Siemon et al., 2009). In the navigation data processing, navigation data are filtered and averaged automatically even if, occasionally, manual corrections may need to be applied to the altitude data (Siemon et al., 2009). In the voltage data processing, raw data are filtered and “averaged” by “square” or “trapezoid” stacking window. After the voltage data processing, voltage data conditioning needs to be further refined manually, especially in the area with infrastructures affecting the measurements. At the end, a fast inversion is necessary to fine-tune and quality check the processing steps done before

(Siemon et al., 2009).

The processed data can be used to obtain information about the subsurface as the recorded responses depend on the physical properties and contrasts in the earth. Inversion provides a mathematical framework for reconstructing physical property models consistent with those data. Generally, the processed data are inverted into conductivity and depths using a layered half-space model (Siemon et al., 2009). Usually, 1D inversion of AEM data is sufficient (even if it can be demonstrated that this common practice can produce misleading results: in fact, 1D reconstruction of even mild 3D conductivity distribution may lead to wrong, but very certain, reconstruction – kindly, see the following and Bai et al. (2021). In the framework of 1D inversions, spatially constrained inversion (SCI) schemes have gained popularity as, despite their rough 1D forward approximation, enforce spatial coherency in the reconstruction. The bond between adjacent 1D models can be formalized by "smooth" (Viezzoli et al., 2008) or "sharp" (Vignoli et al., 2017) regularizations. Clearly, in the case of complex, severely 3D environments (as those often typical in mineral exploration), it is hard to believe that 1D approaches can produce satisfactory results. This is the main reason for the research to focus more and more often on truly 3D approaches. In this respect, the seminal works by Oldenburg et al. (2013) and Cox et al. (2010, 2021) are worth being highlighted. Still, because of their computational costs, 3D algorithms are far from being applicable (especially to stochastic inversion schemes).

1.2. Modelling error and inversion, in Airborne Electromagnetics

In the deterministic framework, the inversion problem is solved by minimizing an objective function that consists of a data misfit and a stabilizer, with a trade-off parameter controlling their relative contributions (Tikhonov and Arsenin, 1977). Eq.1-1 is a possible mathematical expression of this objective function:

$$\phi(\boldsymbol{m}) = \phi_d(\boldsymbol{m}) + \beta\phi_m(\boldsymbol{m}) \qquad 1\text{-}1$$

where $\phi_d(\boldsymbol{m})$ is data misfit, $\phi_m(\boldsymbol{m})$ is regularization and β is the trade-off parameter. Specifically, AEM inversion consists of finding a model of the earth conductivity distribution that is consistent with the observed data and the prior (possibly, geological) information. For the evaluation of the consistency between the hypothetical solution and the observed data, the data misfit is calculated between the observed and the predicted data produced by the forward modeling when applied to the hypothetical conductivity distribution. Therefore, for the AEM inversion, we may write the data misfit in Eq.1-1 as:

$$\phi_d(\boldsymbol{m}) = \frac{1}{2}\|\boldsymbol{W}_d(\boldsymbol{d}_{obs} - F(\boldsymbol{m}))\|_{L2}^2 \qquad 1\text{-}2$$

where $\boldsymbol{d}_{obs}$ consists of observed data, $F(\boldsymbol{m})$ is a forward modeling that simulates the predicted data of the guessed model $\boldsymbol{m}$. $\boldsymbol{W}_d$ is a matrix connected to the estimated noise in the data (or, as it will be clear in the following, also to the noise associated with the used forward approximation – Bai et al. (2021)).

Currently, the minimization of the objective functions that are commonly used in standard AEM inversions are deterministic, gradient-based approaches. These approaches start with an initial

model and updates it iteratively along the gradient direction of the objective function; this minimization process proceeds until the difference between the observed and the predicted data is less than a predetermined tolerance.

Because AEM surveys may include thousands of flight lines (Ley-Cooper et al., 2020), the inversion process must be fast enough to deal with these kinds of massive datasets. Clearly, 1D forwards have been, for their computational efficiency, the first choice for the minimization of the objective function in Eq.1-1. The theory behind the 1D time-domain AEM forward is based on solving Maxwell's equation given a set of conditions and assumptions. The mathematical formulation is presented in Ward and Hohmann (1988). Accordingly, for most of the earth problems, the physical properties can be assumed to be (locally) changing in the vertical direction (depth). For this "layered earth", the Maxwell's equation can be solved in the Fourier transform space. The final solution, in the time-domain is obtained by the inverse Fourier or Hankel transformation.

Although 1D inversions have been proved effective in many practical cases, significant inaccuracies may occur when true geoelectrical structures are essentially multidimensional (Goldman et al., 1994). And 1D solutions can only be regarded as an approximate calculation (having said this, in any case, we will always deal with approximation, even in the case of very sophisticated 3D forward as, for example, the discretization and parameterization will be always finite). Even with an (ideal) perfect forward, when problem is linearized - e.g., at every iteration of the iterative minimization, an error is introduced. With the rough 1D forward approximation, the inaccuracy is even more severe.

The problem caused by approximate calculation in 1D inversion has been investigated, for example, by Goldman et al., (1994): there, several synthetic tests are performed and are summarized in Figure 1-4. Indeed, Figure 1-4 shows both the true geoelectric model and the recovered one obtained by using a 1D inversion. In both cases, the depth and the resistivity of the first layer are accurately reconstructed far from the lateral resistivity changes, whereas portions of the model close to the horizontal heterogeneities (where the true structure cannot be assumed as "layer earth") are misestimated. These synthetic tests directly and vividly remind us the approximate calculation problem cannot be ignored especially in those multidimensional geoelectrical structures survey.

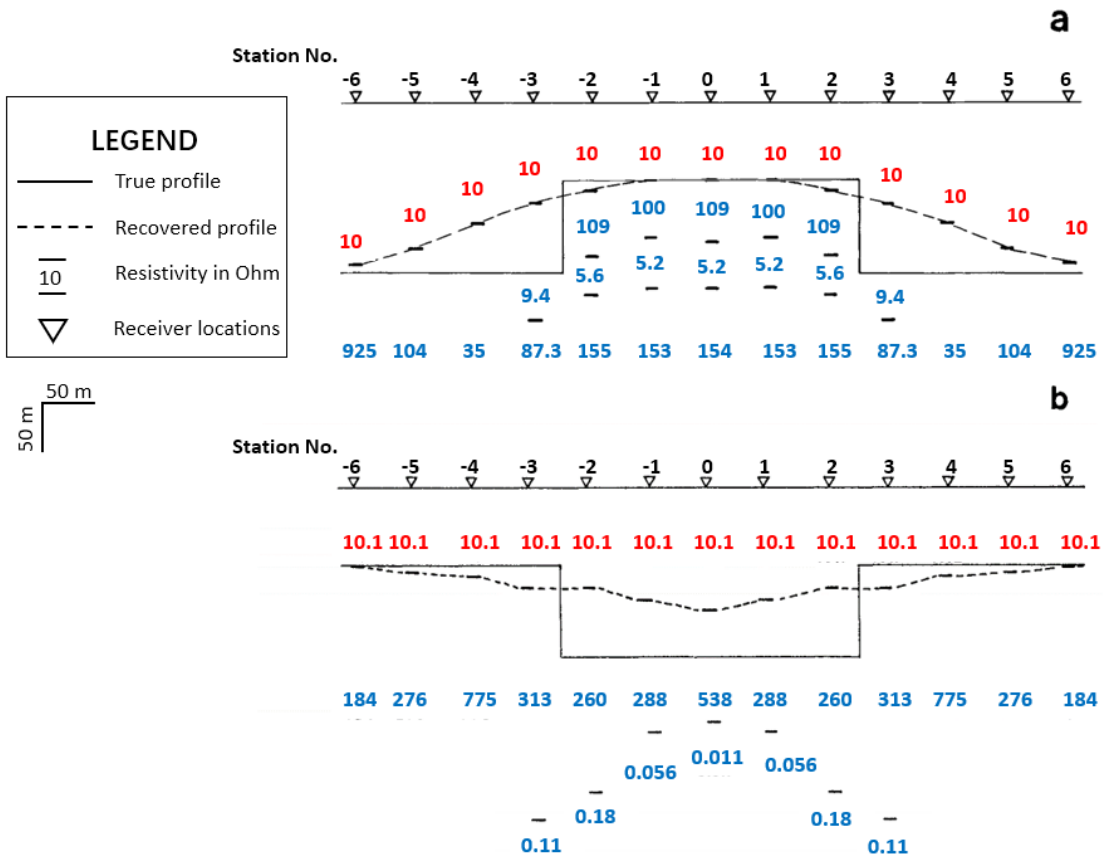

Figure 1-4 1D inversions of two different synthetic datasets: (a) the first dataset corresponds to a 2-layer resistivity model with a 10 Ohm-m for the upper layer and 300 Ohm-m for the bottom one; (b) the second to a 2-layer resistivity model with 10 ohm-m for the upper layer and 300 ohm-m for the bottom (after Goldman et al., 1994).

1.3. Possible (deterministic) inversion strategies: pseudo-3D, full-3D, and 1D inversion with modeling error

From the beginning of the new century, there are several attempts to improve the accuracy of the inversion result, such as full-3D inversion with moving footprint (e.g., Cox et al., 2010), lateral/spatial constrains in 1D version (pseudo-3D inversion) (e.g., Viezzoli et al., 2008).

Obviously, the most direct way to deal with modeling error introduced by poor approximations is to use 3D forward instead of 1D schemes in the inversion process (however we will always be dealing with some approximation error, even in case of very sophisticated 3D forward algorithms). In the early attempts, such as in Haber et al. (2007), the authors developed an inversion algorithm that allowed the 3D inversion of data from at the maximum a very few transmitter locations. The forward problem was solved using an iterative Krylov space method, and the computation time increased linearly with the number of transmitter locations (Oldenburg et al., 2013). Therefore, for a typical ground or airborne survey which includes many source locations, the algorithm was too

computationally expensive to be practically used. Also, similar problems are described in Zaslasky et al. (2011). More recently, Oldenburg et al. (2013) presented another 3D inversion methodology for time-domain electromagnetic data. In Oldenburg et al. (2013), depending on the availability of matrix-factorization software (the package Multifrontal Massively Parallel Solver or MUMPS) and high-performance (parallel calculation) computing, the 3D time-domain EM problem solution can be found by using direct solvers. By solving the forward problem with finite volume or finite integration techniques, they transform the Maxwell's equations into the expression (more details of the derivation process in Oldenburg et al., 2013):

$$A(\sigma, \delta t)\vec{H}^{i+1} = rhs \qquad 1\text{-}3$$

where A is a symmetric positive definite forward modeling matrix that can be rewritten via Cholesky decomposition as $A = LL^T$, σ is the conductivity, δt is the time step, $\vec{H}$ is the magnetic field and $rhs$is the right hand side of the equation. The core idea of the direct solver is: by using the same time step δt, the linear system above is identical for all time and all sources, hence, a single factorization can be used to solve all the linear systems. In practice, several factorizations were calculated by MUMPS, since several different time steps needed to be used. This direct solver has a big advantage with respect to the iterative ones when it is used in the inversion process Since it obviously removes the need for numerous iterations. Oldenburg et al. (2013) declare that, by the above-mentioned direct solver approach, small and midsized problems can be handled on a single node having six cores and 16 GB per core. However, larger problem requires multi-nodes with extended memory.

Another 3D inversion technique was tested by Cox et al. (2010). It is widely known that AEM data are sensitive to a limited footprint (Liu and Becker, 1990). The footprint is defined as the lateral extent of the sensitivity of the AEM system. Cox et al. (2010) introduced the concept of moving footprint for practical 3D inversions. They used a 3D volume integral equation method (Hohmann, 1975) to solve 3D forward modeling, and a regularized conjugate gradient method for minimizing objective function.

Because of moving footprint, each data point is sensitive to a limited number of components of the 3D model parameterization. Therefore, at each iteration step of the inversion process, the sensitivity matrix of the entire AEM survey could be a sparse matrix. In this sparse matrix, the number of non-zero elements corresponds to the size of each footprint (Cox et al., 2010). Consequently, the computation time and memory requirements reduced by several orders of magnitude. The moving footprint approach has been tested on several dataset. For example, in Cox et al. (2010), the authors claim that their 3D reconstruction (based on the moving footprint approach) is more consistent with the actual geology of the investigated area when compared against alternative 1D reconstructions. However, as it is clear, for example, from the results in Ley-Cooper et al. (2015), 3D inversions might have convergence problems and might not be able to fit the data adequately. So, in general, a starting model quite close to the final solution could be necessary. And it clearly not trivial to provide a decent starting model to feed the 3D inversion.

Alternatives based on 1D forward modelling but designed to enforce some level of spatial consistency via regularization terms connecting adjacent 1D model locations have still performances competing with the available 3D approaches. In this respect, focusing on the Bookpurnong area, Viezzoli et al. (2010) show that pseudo-3D approaches based on Spatially Constrained Inversion (SCI) strategies are still valuable. Similar conclusions are drawn, for example, also in the recent work by Munday et al. (2018).

SCI is a least-squares inversion of a layered earth regularized through spatial constraints, which give smooth lateral transitions (Viezzoli et al., 2008). In the following, the principles of the Spatially Constrained Inversion are discussed briefly. By the first term of the Taylor expansion, in the inversion process, the observed data can be written as:

$$\boldsymbol{d}_{obs} - \boldsymbol{e}_{obs} \cong \boldsymbol{G}\delta\boldsymbol{m} \quad + \boldsymbol{g}(\boldsymbol{m}_{ref}) \tag{1-4}$$

where $\boldsymbol{d}_{obs}$ is the observed data vector, $\boldsymbol{e}_{obs}$ represents the error on the observed data, $\boldsymbol{g}$ is the forward modelling, and $\delta\boldsymbol{m}$ is the difference between the selected model $\boldsymbol{m}$ and the reference model$\boldsymbol{m}_{ref}$. In SCI, the spatial constraints help to resolve model parameters using the information coming from the neighboring soundings. Instead of inverting the observed data individually, SCI inverts all data soundings synchronously.

The elements of Jacobian matrix $\boldsymbol{G}$ can be written as:

$$\boldsymbol{G}_{ij} = \frac{\partial \boldsymbol{d}_i}{\partial \boldsymbol{m}_j} \tag{1-5}$$

for the i-th data component and the j-th model (Viezzoli et al., 2008). In short, Eq.1-4 can be written as

$$\boldsymbol{G}\delta\boldsymbol{m} = \delta\boldsymbol{d}_{obs} - \boldsymbol{e}_{obs} \tag{1-6}$$

where $\delta\boldsymbol{d}_{obs} = \boldsymbol{d}_{obs} - \boldsymbol{g}(\boldsymbol{m}_{ref})$. The constraints connecting adjacent models (associated with adjacent measurement sounding locations) can have the following form:

$$\boldsymbol{R}\delta\boldsymbol{m} \quad = -\boldsymbol{R}\boldsymbol{m}_{ref} + \boldsymbol{e}_r \tag{1-7}$$

where $\boldsymbol{e}_r$ is the "error" in the constraints (it provides an estimation of how much reliable we consider the constraints; they are related to the model covariance (Bai et al.,2021) and $\boldsymbol{R}$ is the roughening matrix which contains 1 and -1 for the constrained parameters:

$$\boldsymbol{R} = \begin{bmatrix} 1 & 0 & \dots & 0 & -1 & 0 & \dots & 0 & 0 & 0 \\ 0 & 1 & 0 & \dots & 0 & -1 & 0 & \dots & 0 & 0 \\ \vdots & & & & & \vdots & & & & \vdots \\ 0 & 0 & 0 & \dots & 0 & 1 & 0 & \dots & 0 & -1 \end{bmatrix} \tag{1-8}$$

By the Eq.1-6 and 1-7, the objective function of SCI can be written as:

$$\begin{bmatrix} \boldsymbol{G} \\ \boldsymbol{R} \end{bmatrix} \delta\boldsymbol{m}_{true} = \begin{bmatrix} \delta\boldsymbol{d}_{obs} \\ -\boldsymbol{R}\boldsymbol{m}_{ref} \end{bmatrix} + \begin{bmatrix} \boldsymbol{e}_{obs} \\ \boldsymbol{e}_r \end{bmatrix} \tag{1-9}$$

or, more compactly,

$$\boldsymbol{G}'\delta\boldsymbol{m} \quad = \delta\boldsymbol{d}' + \boldsymbol{e}' \tag{1-10}$$

The covariance matrix becomes

$$\boldsymbol{C}' = \begin{bmatrix} \boldsymbol{C}_{obs} & 0 \\ 0 & \boldsymbol{C}_R \end{bmatrix} \tag{1-11}$$

where $\boldsymbol{C}_{obs}$ refers to observed noise and $\boldsymbol{C}_R$ refers to the constraint's uncertainty. Hence, the objective function

$$Q = \left(\frac{1}{N+A}[(\delta \boldsymbol{d}'^{T} \boldsymbol{C}'^{-1} \delta \boldsymbol{d}')]\right)^{\frac{1}{2}} \quad 1\text{-}12$$

where A is the number of constraints and N is the number of data (Viezzoli et al., 2008), can be minimized by

$$\delta \boldsymbol{m} = (\boldsymbol{G}'^{T} \boldsymbol{C}'^{-1} \boldsymbol{G}')^{-1} \boldsymbol{G}'^{T} \boldsymbol{C}' \delta \boldsymbol{d}' \quad 1\text{-}13$$

Because of the lateral constraints factor, the information from adjacent sounding could migrate to the closest ones. Hence, in SCI, not only the inversion problem is solved by minimizing an objective function that consists of a data misfit and a stabilizer, but also the inversion problem is constrained by neighboring information. Additionally, prior information, e.g., originating from electric logs, can be added at any point of the profile and migrates. Often a 1D solution with spatial constraints is sufficient in quasi-layered sedimentary environment (Auken and Christiansen, 2004).

In this thesis, instead of deterministic inversions, we choose stochastic strategies. For our approach, we directly estimate the modeling error caused by approximate calculation of forward modeling. The assessment of the modeling error is performed via the evaluation of the responses of a set of realizations of the prior. On the other hand, one of the advantages of the stochastic inversion is in the possibility of introducing "arbitrary" prior information for constraining the inversion. So, the same (potentially complex) prior information can be used to feed the stochastic inversion and, at the same time, to calculate the appropriate modelling error. This does not mean that the assessment of the modeling error cannot be used in deterministic approaches, but, since a complex prior is needed for the modeling error assessment, why not take full advantage of it (via the utilization of statistical approaches)?

1.4. Stochastic inversion approaches

Tarantola and Valette (1982) is generally considered the seminal paper concerning the development of stochastic inversion of geophysical data. In that framework, all information (described by a distribution $p(\mathbf{m})$) must be qualified probabilistically through a likelihood function $L(\mathbf{m})$. The prior probability distribution $p(\mathbf{m})$ is the probability distribution representing prior knowledge about the model parameters which can be derived, for example, from geological expert knowledge (Mosser et al., 2020; Nawaz and Curtis, 2016), rock-physics (de Figueiredo et al., 2018; Grana, 2016), nearby outcrops (Pereira et al. 2016), previous surveys (Høyer et al., 2017) and similar sources. This prior knowledge can be formalized in different ways; for example via single Gaussian distribution (de Figueiredo et al., 2017), Gaussian mixture (Grana et al., 2017), multivariate Gaussian priors (Chen et al., 2012) or Multiple Point Statistics (Høyer et al., 2017). The likelihood function $L(\mathbf{m})$ represents the expected data residual $L(\boldsymbol{m}) = L(\boldsymbol{d} - F(\boldsymbol{m}))$ (Hansen, 2021). Once the available information is quantified, the combined state of information (in form of the prior distribution and the likelihood) can be obtained. Therefore, the solution of stochastic inversion is a probability density (posterior probability distribution $p(\mathbf{m}|\mathbf{d})$, which can be written as:

$$p(\boldsymbol{m}|\boldsymbol{d}) = kp(\boldsymbol{m})L(\boldsymbol{m}) \quad 1\text{-}14$$

where $k^{-1} = \int p(\boldsymbol{m})L(\boldsymbol{m})\, d\boldsymbol{m}$ is a normalizing constant such that $\int p(\boldsymbol{m}|d)\, d\boldsymbol{m} = 1$, $\boldsymbol{d}$ is the observed data vector.

Generally, it is impossible to find an analytical expression for $p(\mathbf{m}|\mathbf{d})$. Instead, the posterior

distribution $p(\mathbf{m}|\mathbf{d})$ can be efficiently described by a set of samples generated by the adopted sampling method.

In the airborne geophysical surveys, the observed data (secondary EM field) collected by the recording equipment are finite in number (e.g., limited time gates) with contaminated noise. Because of this, even the relatively simple 1D deterministic inversion of EM data (in presence of noisy measurements and a limited amount of data points) is an ill-posed problem. Hence, for the deterministic inversion, regularization is an indispensable part of finding the optimal solution.

However, it is not easy to estimate the impact of regularization parameters on model uncertainty, and they are difficultly related to geological information (Hauser et al., 2015). Consequently, the solution reliability of the deterministic inversion cannot be evaluated.

On the contrary, stochastic inversion has an advantage to estimate the reliability of the solution. Because the solution of stochastic inversion is the posterior probability density, it can be naturally used to infer the result uncertainty (Minsley et al., 2021). Moreover, stochastic inversions could also account for the uncertainty associated to each step of the modeling workflow (Fjeldstad and Grana, 2018; Grana and Della Rossa, 2010).

1.5. Reference

Auken, E., and Christiansen, A. V., 2004, Layered and laterally constrained 2D inversion of resistivity data: Geophysics, v. 69, no. 3, p. 752-761.

Bai, P., Vignoli, G., and Hansen, T. M., 2021, 1D stochastic inversion of airborne time-domain electromagnetic data with realistic prior and accounting for the forward modeling error: Remote Sensing, in press.

Chen, J., Hoversten, G. M., Key, K., Nordquist, G., and Cumming, W., 2012, Stochastic inversion of magnetotelluric data using a sharp boundary parameterization and application to a geothermal site: Geophysics, v. 77, no. 4, p. E265-E279.

Cox, L. H., Wilson, G. A., and Zhdanov, M. S., 2010, 3D inversion of airborne electromagnetic data using a moving footprint: Exploration Geophysics, v. 41, no. 4, p. 250-259.

-, 2012, 3D inversion of airborne electromagnetic data: Geophysics, v. 77, no. 4, p. WB59-WB69.

de Figueiredo, L. P., Grana, D., Bordignon, F. L., Santos, M., Roisenberg, M., and Rodrigues, B. B., 2018, Joint Bayesian inversion based on rock-physics prior modeling for the estimation of spatially correlated reservoir properties: Geophysics, v. 83, no. 5, p. M49-M61.

de Figueiredo, L. P., Grana, D., Santos, M., Figueiredo, W., Roisenberg, M., and Schwedersky Neto, G., 2017, Bayesian seismic inversion based on rock-physics prior modeling for the joint estimation of acoustic impedance, porosity and lithofacies: Journal of Computational Physics, v. 336, p. 128-142.

Dentith, M., and Mudge, S. T., 2014, Geophysics for the mineral exploration geoscientist, Cambridge University Press.

Dzikunoo, E. A., Vignoli, G., Jørgensen, F., Yidana, S. M., and Banoeng-Yakubo, B., 2020, New regional stratigraphic insights from a 3D geological model of the Nasia sub-basin, Ghana, developed for hydrogeological purposes and based on reprocessed B-field data originally collected for

mineral exploration: Solid Earth, v. 11, no. 2, p. 349-361.

Fjeldstad, T., and Grana, D., 2018, Joint probabilistic petrophysics-seismic inversion based on Gaussian mixture and Markov chain prior models: Geophysics, v. 83, no. 1, p. R31-R42.

Goldman, M., Tabarovsky, L., and Rabinovich, M., 1994, On the influence of 3-D structures in the interpretation of transient electromagnetic sounding data: Geophysics, v. 59, no. 6, p. 889-901.

Grana, D., 2016, Bayesian linearized rock-physics inversion: Geophysics, v. 81, no. 6, p. D625-D641.

Grana, D., and Della Rossa, E., 2010, Probabilistic petrophysical-properties estimation integrating statistical rock physics with seismic inversion: Geophysics, v. 75, no. 3, p. O21-O37.

Grana, D., Fjeldstad, T., and Omre, H., 2017, Bayesian Gaussian Mixture Linear Inversion for Geophysical Inverse Problems: Mathematical Geosciences, v. 49, no. 4, p. 493-515.

Haber, E., Oldenburg, D., and Shekhtman, R., 2007, Inversion of time domain 3D electromagnetic data: Geophys. J. Int, v. 171.

Hansen, T. M., 2021, Efficient probabilistic inversion using the rejection sampler—exemplified on airborne EM data: Geophysical Journal International, v. 224, no. 1, p. 543-557.

Hansen, T. M., 2021a, Efficient probabilistic inversion using the rejection sampler—exemplified on airborne EM data: Geophysical Journal International, v. 224, no. 1, p. 543-557.

Hansen, T. M., 2021b, Probabilistic inverse problems using machine learning-applied to inversion of airborne EM data.

Hansen, T. M., Cordua, K. S., Jacobsen, B. H., and Mosegaard, K., 2014, Accounting for imperfect forward modeling in geophysical inverse problems—exemplified for crosshole tomography: Geophysics, v. 79, no. 3, p. H1-H21.

Hauser, J., Gunning, J., and Annetts, D., 2015, Probabilistic inversion of airborne electromagnetic data under spatial constraints: Geophysics, v. 80, no. 2, p. E135-E146.

Høyer, A.S., Vignoli, G., Hansen, T.M., Vu, L.T., Keefer, D.A. and Jørgensen, F., 2017. Multiple-point statistical simulation for hydrogeological models: 3-D training image development and conditioning strategies. Hydrology and Earth System Sciences, 21(12), pp.6069-6089.

Hohmann, G. W., 1975, Three-dimensional induced polarization and electromagnetic modeling: Geophysics, v. 40, no. 2, p. 309-324.

Karshakov, E. V., Podmogov, Y. G., Kertsman, V. M., and Moilanen, J., 2017, Combined frequency domain and time domain airborne data for environmental and engineering challenges: Journal of Environmental and Engineering Geophysics, v. 22, no. 1, p. 1-11.

Ley-Cooper, A. Y., Brodie, R. C., and Richardson, M., 2020, AusAEM: Australia's airborne electromagnetic continental-scale acquisition program: Exploration geophysics, v. 51, no. 1, p. 193-202.

Liu, G., and Becker, A., 1990, Two-dimensional mapping of sea-ice keels with airborne electromagnetics: Geophysics, v. 55, no. 2, p. 239-248.

Minsley, B. J., Foks, N. L., and Bedrosian, P. A., 2021, Quantifying model structural uncertainty using airborne electromagnetic data: Geophysical Journal International, v. 224, no. 1, p. 590-607.

Moilanen, E., Karshakov, E., and Volkovitsky, A., Time domain helicopter EM system Equator: Resolution, sensitivity, universality, *in* Proceedings 6th International AEM Conference & Exhibition2013, European Association of Geoscientists & Engineers, p. cp-383-00041.

Mosser, L., Dubrule, O. and Blunt, M.J., 2020. Stochastic seismic waveform inversion using generative adversarial networks as a geological prior. Mathematical Geosciences, 52(1), pp.53-79.

Munday, T., Soerensen, C., Marchant, D., Silic, J., Paterson, R., Viezzoli, A., Kunzmann, M., and Spinks, S., 2018, 1, 2.5 and/or 3D Inversion of Airborne EM data-options in the search for sediment-hosted

base metal mineralisation in the McArthur Basin, Northern Territory: ASEG Extended Abstracts, v. 2018, no. 1, p. 1-8.

Nawaz, M.A. and Curtis, A., 2016. Bayesian inversion of seismic attributes for geological facies using a hidden Markov model. Geophysical Journal International, p.ggw411.

Oldenburg, D. W., Haber, E., and Shekhtman, R., 2013, Three dimensional inversion of multisource time domain electromagnetic data: Geophysics, v. 78, no. 1, p. E47-E57.

Paine, J. G., and Minty, B. R., 2005, Airborne hydrogeophysics, hydrogeophysics, Springer, p. 333-357.

Palacky, G., 1993, Use of airborne electromagnetic methods for resource mapping: Advances in space research, v. 13, no. 11, p. 5-14.

Pereira, Â., Nunes, R., Azevedo, L., Soares, A. and Guerreiro, L., 2016, April. Seismic inversion using analogs for reservoir characterization and uncertainty assessment in early stages of exploration. In International Conference and Exhibition, Barcelona, Spain, 3-6 April 2016 (pp. 304-304). Society of Exploration Geophysicists and American Association of Petroleum Geologists.

Sapia, V., Oldenborger, G. A., Jørgensen, F., Pugin, A. J.-M., Marchetti, M., and Viezzoli, A., 2015, 3D modeling of buried valley geology using airborne electromagnetic data: Interpretation, v. 3, no. 4, p. SAC9-SAC22.

Sengpiel, K.-P., and Fluche, B., 1992, Application of airborne electromagnetics to groundwater exploration in Pakistan: Zeitschrift der Deutschen Geologischen Gesellschaft, p. 254-261.

Siemon, B., Christiansen, A. V., and Auken, E., 2009, A review of helicopter-borne electromagnetic methods for groundwater exploration: Near Surface Geophysics, v. 7, no. 5-6, p. 629-646.

Tarantola, A., 2005, Inverse problem theory and methods for model parameter estimation, SIAM.

Tarantola, A., and Valette, B., 1982, Inverse problems= quest for information: Journal of geophysics, v. 50, no. 1, p. 159-170.

Tikhonov, A. N., and Arsenin, V. Y., 1977, Solutions of ill-posed problems: New York, v. 1, no. 30, p. 487.

Viezzoli, A., Christiansen, A. V., Auken, E., and Sørensen, K., 2008, Quasi-3D modeling of airborne TEM data by spatially constrained inversion: Geophysics, v. 73, no. 3, p. F105-F113.

Viezzoli, A., Munday, T., Auken, E., Christiansen, A. V., and Wilson, G. A., 2010, Accurate quasi 3D versus practical full 3D inversion of AEM data–the Bookpurnong case study: Preview, v. 2010, no. 149, p. 23-31.

Vignoli, G., Dzikunoo, E. A., Jørgensen, F., Yidana, S. M., Banoeng-Yakubo, B., and Bai, P., Geophysical Modelling of a Sedimentary Portion of the White Volta Basin (Ghana), *in* Proceedings International Conference on Computational Science and Its Applications2020, Springer, p. 891-902.

Vignoli, G., Sapia, V., Menghini, A., and Viezzoli, A., 2017, Examples of improved inversion of different airborne electromagnetic datasets via sharp regularization: Journal of Environmental and Engineering Geophysics, v. 22, no. 1, p. 51-61.

Volkovitsky, A., and Karshakov, E., Airborne EM systems variety: what is the difference?, *in* Proceedings 6th International AEM Conference & Exhibition2013, European Association of Geoscientists & Engineers, p. cp-383-00014.

Ward, S. H., and Hohmann, G. W., 1988, Electromagnetic theory for geophysical applications, Electromagnetic Methods in Applied Geophysics: Voume 1, Theory, Society of Exploration Geophysicists, p. 130-311.

Zaslavsky, M., Druskin, V., and Knizhnerman, L., 2011, Solution of 3D time-domain electromagnetic problems using optimal subspace projection: Geophysics, v. 76, no. 6, p. F339-F351.

Zhdanov, M., Vignoli, G., and Ueda, T., 2006, Sharp boundary inversion in crosswell travel-time tomography: Journal of Geophysics and Engineering, v. 3, no. 2, p. 122-134.

Chapter 2. 1D stochastic inversion of AEM data with realistic prior and accounting for the forward modelling error

This Chapter is largely based on the material discussed in the manuscript Bai et al. (2021). As mentioned in the introduction, airborne electromagnetic surveys may consist of hundreds of thousands of soundings. In most cases, this makes 3D inversions unfeasible even if it would be necessary because of the high level of heterogeneity of the subsurface. Instead, approaches based on 1D forwards are routinely used as they are extremely computational efficient. However, it is relatively easy to fit 3D responses with 1D forward modelling and retrieve apparently well-resolved conductivity models. But those detailed features may simply be caused by fitting the modelling error connected to the approximate forward. In addition, it is, in practice, difficult to identify this kind of artifacts as the modeling error is correlated. Chapter 2. demonstrates a possible strategy to assess the modelling error introduced by the 1D approximation and how to include this additional piece of information into a probabilistic inversion. Not surprisingly, it turns out that incorporating the modeling error into the inversion provides not only much better reconstructions of the targets but, maybe more importantly, guarantees a correct estimation of the corresponding reliability.

2.1. Methodology

The calculation of the response of a physical system is always characterized by some level of modelling error. For example, even in the case of very sophisticated 3D forward modelling tools used to calculate the dB/dt responses of an electrical conductivity distribution caused by the excitation induced by a "perfectly" described ATEM system (is it really possible to characterize a priori an acquisition system? (Christiansen et al., 2011; Moilanen et al., 2013; Sørense and Auken, 2004; Volkovitsky and Karshakov, 2013)), the parameterization used and the size of the discretized domain might affect the retrieved response. In this respect, every time we use a 1D forward modelling approximation (Auken et al., 2015) for the inversion of ATEM data (inherently 3D), we introduce some errors that need to be handled; neglecting this source of additional uncertainty would inevitably lead to artifacts paving the road to successive geological misinterpretations. In the best scenario, the magnitude of the modeling error will be negligible compared to uncertainty in the data, and can be ignored (Tarantola, 2005). More often, modeling errors will be significant, and must be taken into account.

Here, we briefly recall a formal framework in which the modelling error is described through a multivariate normal correlated probability distribution, that can be naturally used when the measurement errors are also Gaussian (Tarantola, 2005). In probabilistic formulations of inverse problems, the goal is to retrieve the posterior probability density function $p(\mathbf{m}|\mathbf{d})$ measuring the

probability of having the model $\mathbf{m}$ compatible with the measurements $\mathbf{d}$. In accordance with Bayes' theorem, $p(\mathbf{m}|\mathbf{d})$ is proportional to the product between the prior probability density function of the model parameters $p(\mathbf{m})$, and the conditional probability density function $p(\mathbf{d}|\mathbf{m})$. Hence, $p(\mathbf{m}|\mathbf{d}) \propto p(\mathbf{d}|\mathbf{m})p(\mathbf{m})$, with $p(\mathbf{d}|\mathbf{m})$ connecting the measured data and the model parameters, and, in the specific case of a Gaussian noise distribution, that can be written as

$$p(\boldsymbol{d}|\boldsymbol{m}) = k_d \, exp\left(-\frac{1}{2}(\boldsymbol{d} - F(\boldsymbol{m}))^T \boldsymbol{W}_d^T \boldsymbol{W}_d (\boldsymbol{d} - F(\boldsymbol{m}))\right) \qquad 2\text{-}1$$

where: (i) k_d is just a normalization factor, (ii) F is the forward modeling operator used during the inversion, and (iii) $\mathbf{W}_\mathrm{d}$ is related to the data covariance $\mathbf{C}$, and, often, by assuming mutually independent data, can be considered equal to $\mathbf{W}_d = \mathrm{diag}(\boldsymbol{\sigma}_\mathrm{d})^{-1} = \mathbf{C}^{-1/2}$ where the i-th component of the vector $\boldsymbol{\sigma}_\mathrm{d}$ is the standard deviation of the i-th data component (in the specific case of the ATEM data, $[\boldsymbol{\sigma}_\mathrm{d}]_i$ is the standard deviation of the dB/dt value associated with the i-th time-gate).

If also the model parameters are assumed to follow a Gaussian distribution, then, the prior information about the solution can be formalized as follows: $p(\mathbf{m}) = k_m \exp\left(-\frac{1}{2}(\mathbf{m} - \mathbf{m}_0)^T \mathbf{W}_m^T \mathbf{W}_m (\mathbf{m} - \mathbf{m}_0)\right)$, in which: (i) k_m is another normalization factor and (ii) the Gaussian is centered on the reference model $\mathbf{m}_0$. In this specific case of Gaussian distributions assumed both for the data noise and the model parameters, we obtain that the maximizer of the probability $p(\mathbf{m}|\mathbf{d})$ is also the minimizer of the regularized inversion objective functional $\left\|\boldsymbol{W}_d\,(\mathbf{d} - F(\boldsymbol{m}))\right\|_{L_2}^2 + \left\|\boldsymbol{W}_m(\mathbf{m} - \mathbf{m}_0)\right\|_{L_2}^2$. In fact, this is a very well-known result (e.g., Tarantola and Valette, 1982; Vignoli et al., 2021; Zhdanov, 2002), to some extent, reconciling probabilistic and deterministic approaches; in particular, if $\mathbf{C}_m^{-1}$ is taken equal to $\lambda^2 \boldsymbol{L}^T \boldsymbol{L}$ with λ being the Tikhonov parameter controlling the relative importance of the regularization term with respect of the data misfit, and $\boldsymbol{L}$ a discrete approximation of the spatial derivative – then, the minimization of the objective functional coincides with the standard Occam's inversion (Constable et al., 1987).

However, the approach discussed in the present research loosens several of these ansätze, and, in the following:

1) we do not restrict ourselves to the Gaussian assumption for the model parameters distribution $p(\mathbf{m})$ as we are going to consider quite general prior distributions defined through the realizations of those distributions and that will be generated via a geologically informed procedure;
2) the $\mathbf{W}_d = \mathbf{C}^{-1/2}$ will not consist uniquely of the component attributable to the noise in the observations, but it will include also a term incorporating the modelling error. In particular, the modelling error will be assumed to be consistent with a Gaussian probability density $\mathcal{N}(\mathbf{d}_\Delta, \boldsymbol{C}_\Delta)$ defined by the mean $\mathbf{d}_\Delta$ and the covariance $\boldsymbol{C}_\Delta$. Hence, the $p(\mathbf{d}|\mathbf{m})$ in Eq.2-1 will have now the following expression (Hansen et al., 2014)

$$p(\boldsymbol{d}|\boldsymbol{m}) = k_d \, exp\left(-\frac{1}{2}(\boldsymbol{d} + \boldsymbol{d}_\Delta - F(\boldsymbol{m}))^T \boldsymbol{W}_\Delta^T \boldsymbol{W}_\Delta (\boldsymbol{d} + \boldsymbol{d}_\Delta - F(\boldsymbol{m}))\right) \qquad 2\text{-}2$$

with $\mathbf{W}_\Delta = (\mathbf{C} + \boldsymbol{C}_\Delta)^{-1/2}$. By construction, as it will be detailed in what follows, also these new terms $\mathbf{d}_\Delta$ and $\boldsymbol{C}_\Delta$ will depend on the prior geological knowledge available about the investigated area.

It is important to stress that despite we demonstrate the effects of taking into account the modelling error within a probabilistic framework, the $\mathbf{W}_\Delta = (\mathbf{C} + \boldsymbol{C}_\Delta)^{-1/2}$ can actually, be, in a very immediate way, incorporated into a deterministic framework as well. The evident advantage of using a stochastic approach is that we can naturally incorporate complex prior information (rather than enforcing simple - e.g., smooth or sharp - constraints) and those pieces of complex information need to be available in any case since they are used for the assessment of the modelling error. As a matter of fact, given the arbitrariness we can benefit from by defining the prior directly via its samples, in general, we could potentially have the maximum flexibility and even use very powerful strategies as, for example, those based on Multiple-point statistics (MPS) approaches (Høyer et al., 2017); in that case, the prior geological information can be formalized by means of the so-called Training Image (TI) that is, basically, representing the conceptual geological model of the expected target subsurface; MPS algorithm can then generates samples of the prior that are statistically stationary with respect to the original TI and that can be used as detailed in the following Subsection 2.1.1. In the present research, however, we use other geostatistical strategies to populate the prior (and consistently estimate the associated modelling error). They will be described in the following as well.

2.1.1. Estimation of Gaussian correlated modeling errors

Here we follow the strategy detailed in Hansen et al. (2014) to (i) simulate and (ii) quantify modeling errors caused by using a 1D forward as opposed to a full 3D forward for simulating ATEM data.

Firstly, a sample of the underling probability distribution representing the modeling errors is generated. This is done by generating a relatively large sample of N_Δ realizations of the prior distribution $p(\mathbf{m})$ as $\boldsymbol{M} = [\boldsymbol{m}'_1, \boldsymbol{m}'_2, \dots, \boldsymbol{m}'_{N_\Delta}]$. The forward response is then calculated by using the approximate 1D forward model, F_{app}, and the (assumed) exact 3D forward model, F_{ex}. This provides a set of 'approximate' and 'exact' data in form of $\boldsymbol{D}_{app} = \left[F_{app}(\boldsymbol{m}'_1), F_{app}(\boldsymbol{m}'_2), \dots, F_{app}\left(\boldsymbol{m}'_{N_\Delta}\right)\right]$ and $\boldsymbol{D}_{ex} = \left[F_{ex}(\boldsymbol{m}'_1), F_{ex}(\boldsymbol{m}'_2), \dots, F_{ex}\left(\boldsymbol{m}'_{N_\Delta}\right)\right]$. Hence, the difference between the approximate and the exact forward models represents a realization, $\left[\boldsymbol{D}_{diff}\right]_i = \left[\boldsymbol{D}_{ex} - \boldsymbol{D}_{app}\right]_i$, of the modelling error associated to the specific i-th sample of the prior.

As it will be discussed also in the following, to feed the 1D forward F_{app}, unidimensional conductivity models have been extracted from the original 3D realizations of the prior in the location just below the acquisition system.

Assuming that the modeling error can be characterized by a multivariate Gaussian distribution $\mathcal{N}(\mathbf{d}_\Delta, \boldsymbol{C}_\Delta)$, the mean and covariance can be trivially computed from the samples $\boldsymbol{D}_{diff}$. Finally,

the assessment of the 1D modeling error can be plugged into Eq.2-2. The number of realizations needed, N_Δ, and the validity of the Gaussian assumption on the modeling errors will be addressed below.

In the present research, as the best approximation F_{ex}, it has been considered an implementation of the forward modelling discussed in detail in Haber (2014). Clearly, the actual simulation has been preceded by a checking phase, in which the 3D forward modelling results have been compared against known solutions assumed to be exact. In our specific case, we performed preliminary tests of the 3D forward against semi-analytical solutions for unidimensional conductivity distributions; the chosen 3D simulation settings have led to mismatches of a few percentage points (generally around 5%). Consequently, as it will be shown later in the chapter, the modelling error inherited from the 3D modelling has been assumed negligible with respect to the other noise sources and it has not been further considered in our analysis.

2.1.2. Inversion strategies

Concerning the deterministic inversion results discussed in the following, as mentioned, we use an Occam's inversion scheme (Vallée and Smith, 2009) in which each individual dB/dt sounding is inverted independently from the adjacent ones and, so, the roughness operator in the regularization terms acts only vertically. To be fair, it is true that this specific kind of prior information, formalized by the stabilizer, is not in accordance with the investigated models (as it will be clear in the descriptions of the tests, characterized by abrupt conductivity changes). Nevertheless, the deterministic algorithm retrieve (smooth) models whose 1D responses are in almost perfect agreement with the inverted 3D dB/dt data. The level of data fitting used for the inversion of the noise-free data is, for all synthetic tests, 0.01%.

The stochastic inversion consists of an independent extended Metropolis algorithm simply obtained by a slight modification of the SIPPI toolbox (Hansen et al., 2013) to make the pro-posed samples independently drawn from the prior ensemble. The 10^5 realizations of the prior are generated in advance since a subset of them needs to be used for the modelling error assessment; the appropriateness of this choice, and the convergency properties will be discussed in the Section "2.3 Analysis of the inversion parameters".

2.2. Synthetic tests

In this section, we perform two synthetic tests of increasing complexity to investigate the effects of including in the inversion process: (i) the proper prior information, and (ii) an estimation of the modelling error. In both cases, we compare our results against a solution provided by a more standard 1D deterministic inversion.

2.2.1. Test 1: 3D conductivity distribution with homogeneous layers

The first test (test 1 – Figure 2-1) consists of a conductivity distribution mimicking possible glacial geological settings typical, for example, of Denmark (Høyer et al., 2015; Jørgensen and Sandersen, 2006; Kehew et al., 2012) and characterized by an intricated network of paleo valleys.

Figure 2-2 compares, for the sounding locations considered in Figure 2-1, the 3D responses calculated for the entire 3D model against the corresponding 1D measurements that would be obtained by considering exclusively the 1D portion of the original distribution just below the acquisition position. The acquisition parameters are those of a typical VTEM system (Kwan et al., 2016; Legault et al., 2015) (e.g., each sounding consists of 54 measurements). Not surprisingly, the 1D responses (Figure 2-2b) are characterized by abrupt lateral changes associated with the lateral variations of the conductivity model (Figure 2-2a), whereas, in accordance with the physics, the 3D dB/dt data are much smoother (Figure 2-2c). Here, we treat the 3D calculated responses as the 'observed data', and invert them by means of both deterministic and probabilistic inversion methods.

In all cases, we assume negligible measurement errors during the inversion as the main purpose is to focus on the modeling error effects. In this respect, it is important to highlight the level that the modelling error can reach: the difference in the 1D and 3D responses (blue line in Figure 2-2b) can be as big as ~20%, and, very seldom, smaller than several percentage points! So, the size of this mismatch should make accounting for the modelling error unavoidable whereas, on the contrary, as mentioned before, the common practice is to tackle it by discretionally increase the measurement noise. Actually, by properly including the modelling error in the inversion, the assumed measurement error could be potentially reduced.

2.2.1.1 Deterministic Occam's inversion.

Figure 2-3 shows the result of 1D deterministic inversion – implementing an Occam's regularization strategy. Clearly, the deterministic result fits the observations extremely well (blue line in Figure 2-3b) and is capable to retrieve the major features of the true model whereas, in some cases, infers deceptive discontinuous reconstructions of the true interfaces (e.g., ~1600 to ~2000 m). It is worth mentioning that the data sensitivity to the model parameters drops below the first reconstructed conductive interface; hence, eventually, all the conductivity variation below that retrieved deep interface would not be considered reliable by skilled interpreters. In this respect, the deterministic result cannot be considered, at least from a practical point of view, much different from the probabilistic result obtained without accounting for the modelling error (and discussed in-depth in the following sub-section). Nevertheless, it is true that the retrieved (laterally discontinuous) features (caused by fitting the coherent modelling error – as it will be clear later) might be challenging to be correctly deciphered and lead to erroneous conclusions.

2.2.1.2 Stochastic inversion without modelling error assessment

The stochastic approach allows incorporation of (in principle) arbitrarily complex prior information, as long as realizations from the prior can be generated. In the present research, we generates independent realizations of $p(\mathbf{m})$ representing buried valley structures (similar to those in Figure 2-1) by means of a Fast Fourier Transform Moving Average (FFT-MA) (Le Ravalec et al., 2000) strategy providing unconditional realizations of a Gaussian random field of the interfaces' locations; in particular, the corresponding mean values are chosen to be uniformly distributed: (i) between 20 and 30 m for the shallowest interface, and (ii) between 65 and 85 m for the deepest, whereas the associated covariance models are characterized by a standard deviations and ranges, respectively, of: (i) 5 m and 100 m, for the first interface, and (ii) 80 m and 500 m for the second. More details about a possible way of constructing the samples can be found in (Hansen and Minsley, 2019) including, for example, some details about the above-mentioned MPS strategies.

Whilst the geometry is varying, the conductivity values of each layer are kept constant realization-by-realization. For clarity, two examples of prior distribution realizations can be seen in Figure 2-4. It is evident that the parameters defining the realizations of the prior have been selected to be in agreement with our expectations about the geological structures we are dealing with.

It is worth highlighting that, since the inversion is one-dimensional, the actual (1D) models used to feed the inversion algorithm are the individual columns (and the corresponding 1D response) of each 3D realization (e.g., in Figure 2-4). So, each single 1D prior model can be described by five parameters (the depths to the interfaces and the three conductivities).

Undoubtedly, the stochastic inversion, with such an informative prior is quite facilitated and is basically reduced to the inference of the locations of the interfaces. As a matter of fact, as Figure 2-5 shows, by using the Metropolis algorithm (Hansen and Minsley, 2019; Mosegaard and Tarantola, 1995), we can reconstruct quite satisfactorily the first interface at about 25-30 m depth, whereas we generally underestimate the depth of the second layer (except for the last ~1500 m on the right). But what is most disturbing is that, even in this simple case, the misleading features reconstructed by the stochastic inversion (here, performed without accounting for the modelling error) appear to be almost certain.

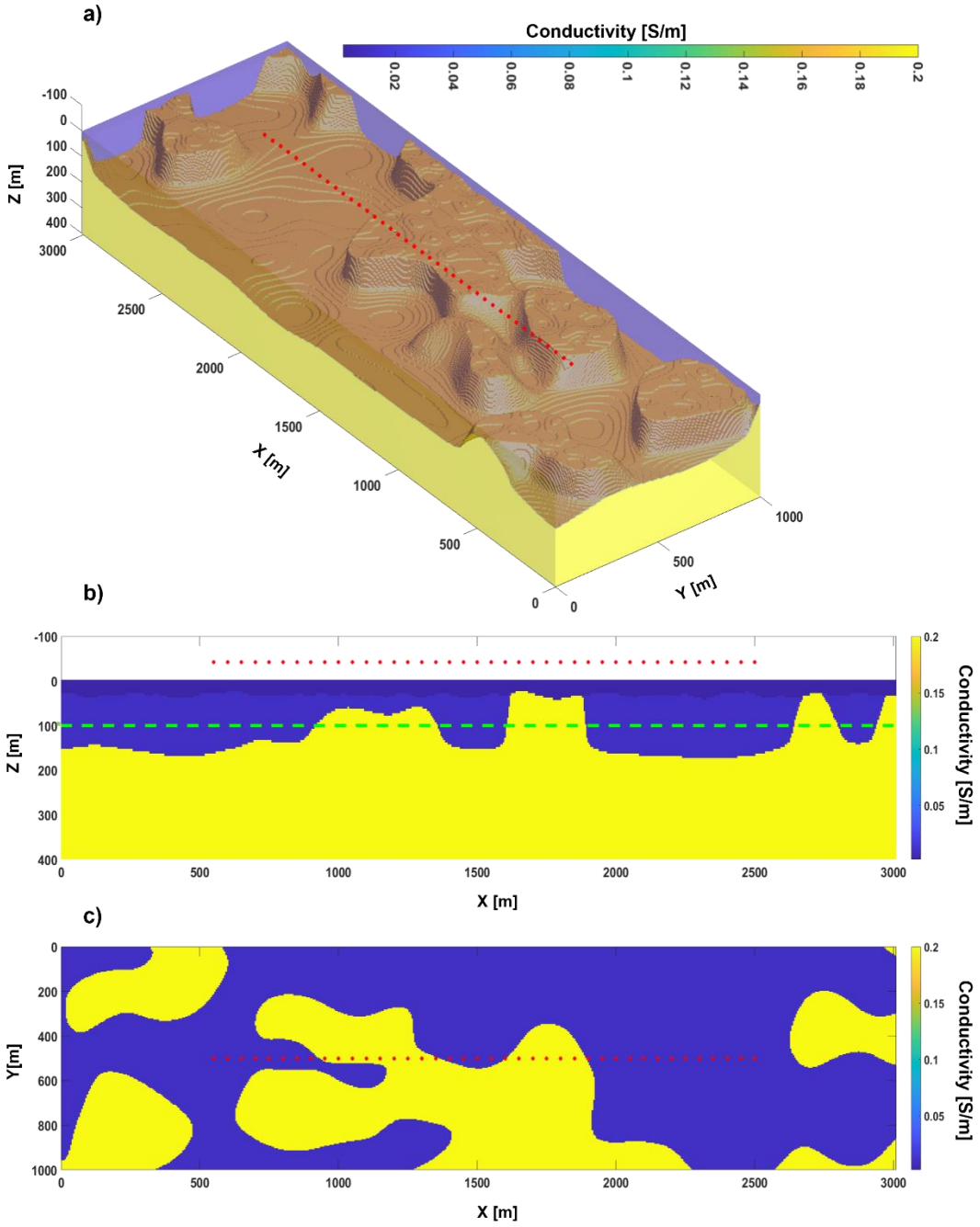

Figure 2-1. Conductivity distribution for test 1: (a) 3D view of the model consisting of a sequence of three homogeneous layers with varying thicknesses; (b) Vertical section of the model in panel (a), along the survey line highlighted by the red dots indicating the locations of the ATEM soundings; (c) Plain view at 100 m depth (dash green line in panel (b)).

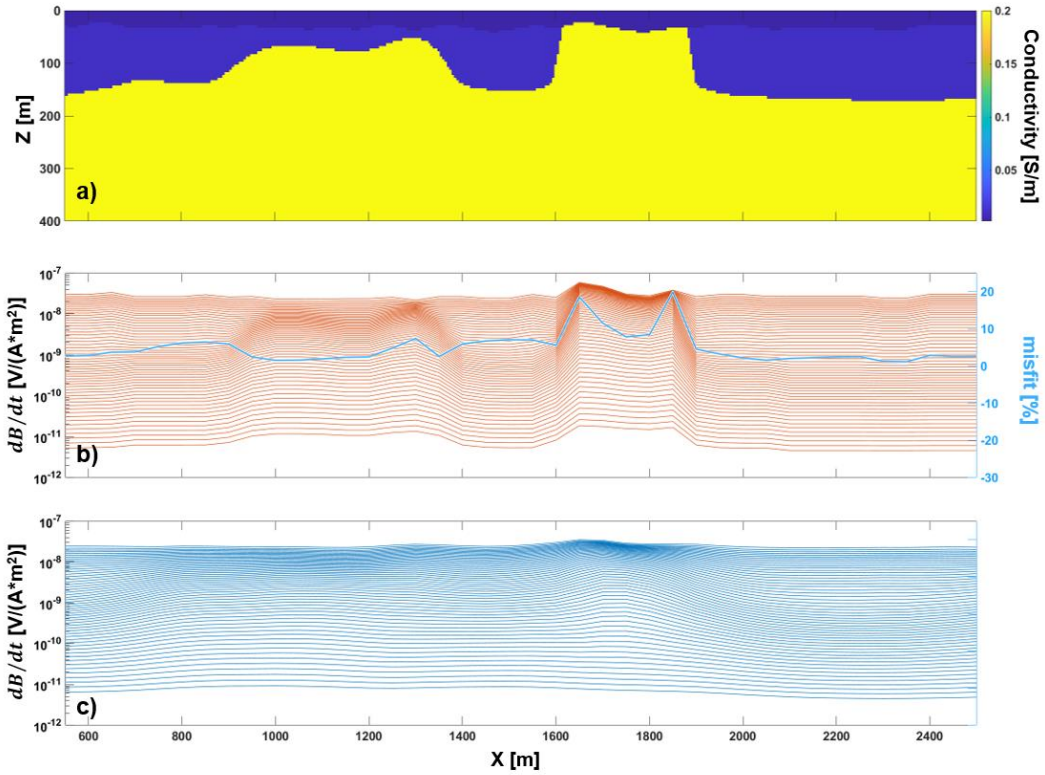

Figure 2-2. Comparison of the 3D and 1D responses for the conductivity model of test 1: (a) Vertical section of the 3D conductivity model in Figure 2-1a (it is a portion of the section in Figure 2-1b); (b) 1D responses calculated for the 1D portions of the original model in Figure 2-1a taken at the locations of the ATEM soundings (red dots in Figure 2-1b) – the blue line represents, sounding-by-sounding, the relative misfit between the 1D and 3D responses (the corresponding axis is on the right, in blue); (c) 3D responses measured at the same location in panel (b), but, here, calculated for the entire 3D conductivity model (Figure 2-1a).

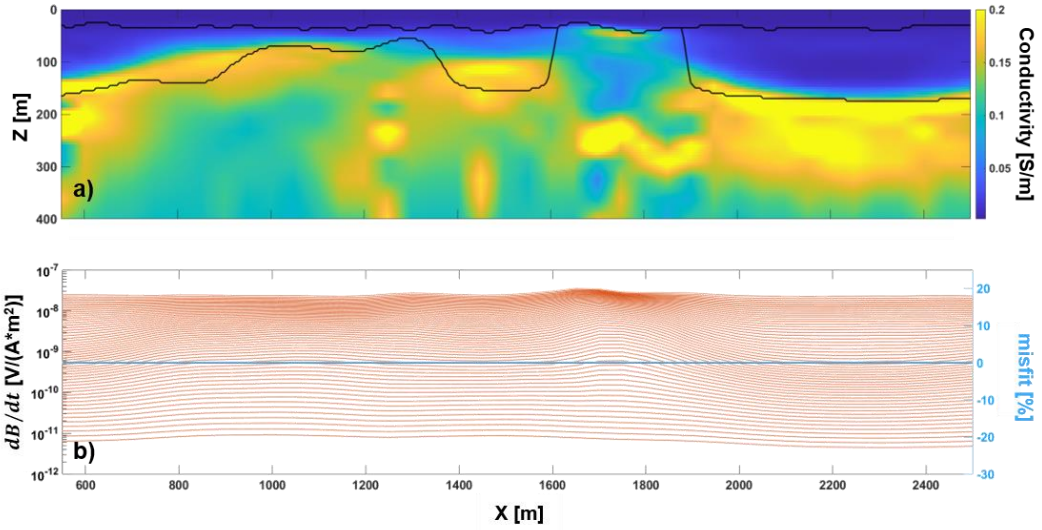

Figure 2-3. 1D deterministic inversion of the 3D data (Figure 2-2c) associated to the conductivity model of test 1 (Figure 2-1a): (a) The solution of the 1D deterministic inversion – the black lines show the interfaces of the original conductivity model to be reconstructed; (b) The 1D responses resulting from the conductivity model in panel (a) – the blue line represents, sounding-by-sounding, the relative misfit between the 3D and 31 1D responses (the corresponding axis is on the right in blue).

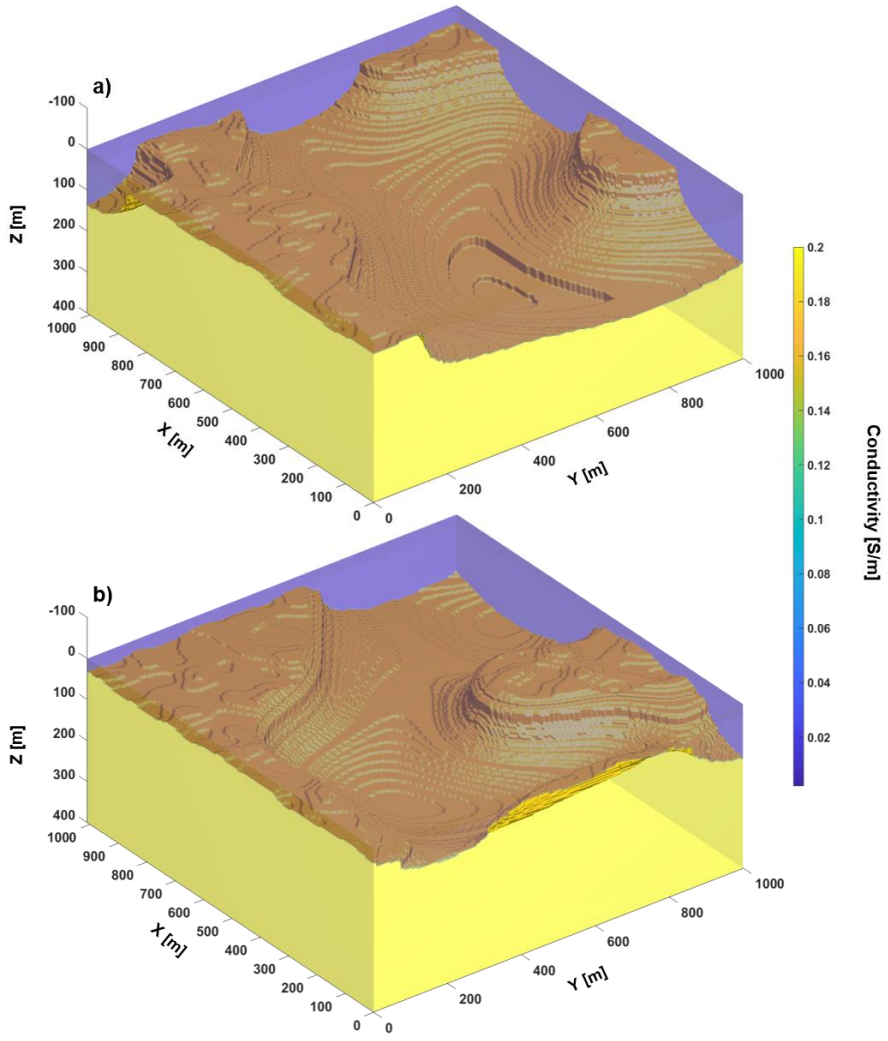

Figure 2-4. Two examples of realizations of the prior distribution used for the stochastic inversion of test 1's dataset.

2.2.1.3 Stochastic inversion incorporating the 1D modelling error

If instead, we use a subset of the 3D prior samples (Figure 2-4) to calculate their actual 3D responses and compare them with the data calculated, this time, by means of the 1D forward modelling applied to the 1D conductivity vertical profile in the center of each selected prior realization, we can estimate the appropriate mean $\mathbf{d}_\Delta$ and covariance $\boldsymbol{C}_\Delta$, and incorporate them into the 1D stochastic inversion scheme. The results of the application of this new scheme to test 1 is showed in Figure 2-6. Now, the result almost perfectly matches the true model. And, when the mean depth of the interfaces does not fit the true conductivity change – for example, near the steep lateral variations around 1000 m and 1400 m – the correct location of the boundaries still lies within the uncertainty bands.

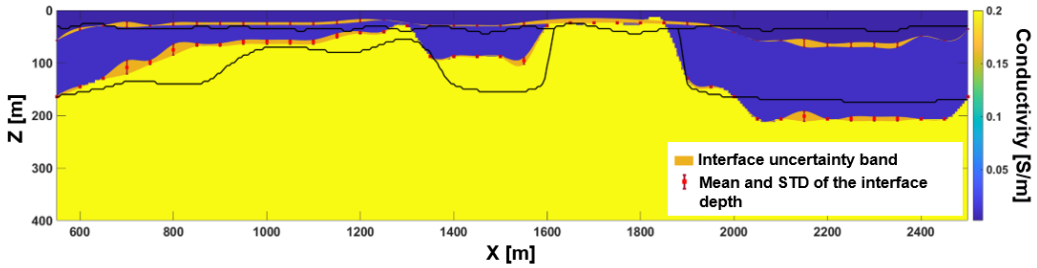

Figure 2-5. 1D stochastic inversion of the 3D data (Figure 2-2c) associated to the conductivity model of test 1 (Figure 2-2a shows one vertical section of that 3D conductivity model). In this case, realistic prior is used (Figure 2-4), but no modelling error has been taken into account. The orange bands represent the reconstruction uncertainty defined by the mean and standard deviation values (red points and vertical bars) deduced by the retrieved realizations of the posterior $p(\mathbf{m}|\mathbf{d})$. As for Figure 2-3a, the black lines show the locations of the interfaces to be reconstructed.

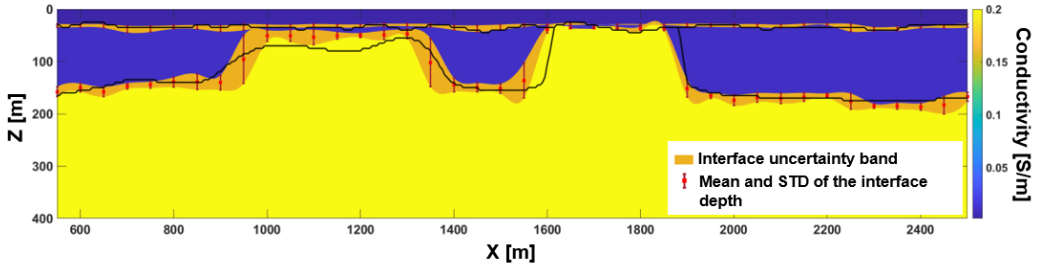

Figure 2-6. 1D stochastic inversion of the 3D data (Figure 2-2c) associated to the conductivity model of test 1 (Figure 2-1a). In this case, realistic prior is used (Figure 2-4) together with the modelling error assessment. As in Figure 2-5, the orange bands represent the uncertainty (the associated mean and standard deviations are plotted as vertical red bars) calculated by the retrieved realizations of the posterior $p(\mathbf{m}|\mathbf{d})$. The black lines show the locations of the interfaces to be reconstructed (Figure 2-2a).

Since we are dealing with 3D conductivity models, it is probably more appropriate to visualize the consequences of the different inversion schemes over several flight lines (Figure 2-7) across the test 1 model. If we examine Figure 2-7b-c, the same conclusions drawn for an individual vertical section are clearly valid also for the other acquisition lines (and, consistently, also for the lateral intra-line resolution – kindly, compare Figure 2-7e-g).

A direct assessment of the performances of the different inversion schemes in terms of data fitting can be performed by looking at Figure 2-8b; in general, the relative mismatch between each of the 54 channels of the observed 3D responses and those calculated (via a 3D forward) from the 3D conductivity distribution obtained via the stochastic inversion (with modelling error appraisal) lays within $\mp 10\%$. It is worth noticing that the relatively poor data fitting on the right side of Figure 2-8b is caused by the higher level of heterogeneity of that end of the model, beyond the surveyed area. In fact, Figure 2-7d shows the rapidly varying morphology for $X > 2500$ m in correspondence of the section considered in Figure 2-8 ($Y \sim 500$ m); that conductivity variation is not in accordance with the inevitable laterally homogeneous extension of the reconstructed

solution (Figure 2-7g). This mismatch affects, not surprisingly, mainly the late-gate measurements. The same does not happen on the other end of the section, where the data fitting is particularly good (Figure 2-8b); in this case, the reason is that, differently from before, the true model continues largely unchanged towards low X values, at least for $Y\sim500$ m (Figure 2-7d). On the other hand, the 3D responses generated by the conductivity volume retrieved by the 1D deterministic inversion (Figure 2-8a) demonstrates, once more, that fitting the data with a 1D forward (as in Figure 2-3b) does not necessarily guarantee that the corresponding 3D calculated data are in agreement with the (3D) observations; indeed, in Figure 2-8a, the relative misfit between the 3D calculated responses and the measurements ranges approximately between $\mp30\%$.

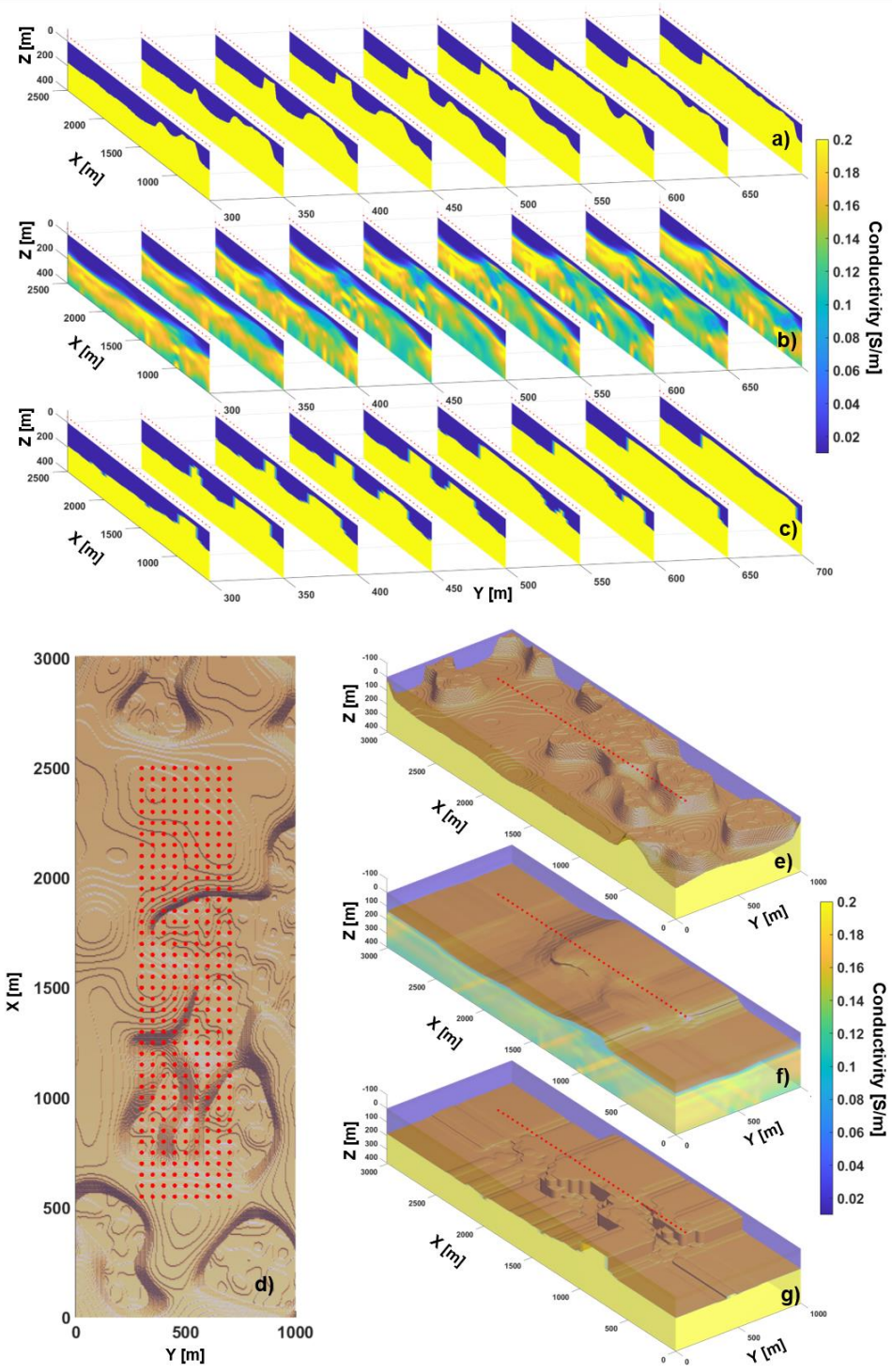

Figure 2-7. The inversion results of the 3D data from (a) test 1's conductivity model (Figure 2-1), and obtained with: (b) Occam's deterministic strategy, and (c) The stochastic strategy incorporating the modelling error. The locations of the inverted soundings are showed as red dots in (d), on top of the plain view of the topography of the second interface of the true model - showed in (e). In (f), the 3D view of the results from (b) is plotted, whereas in (g), it is possible to see a similar 3D view but now based on the stochastic results in (c). For clarity, in panels (e-g), only the sounding locations of the central flight line are showed (as red dots).

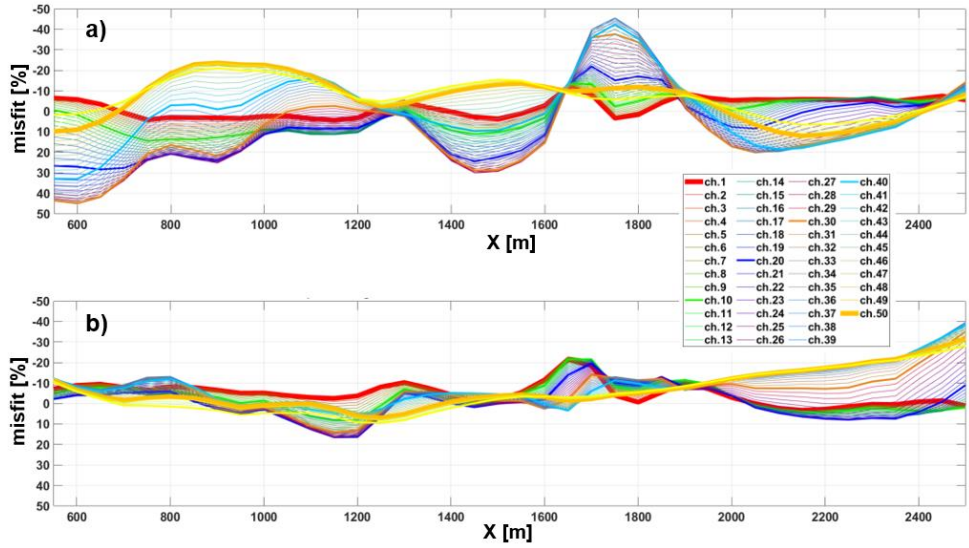

Figure 2-8. Comparison of the percentage misfit between the observed 3D responses and those calculated from: (a) The 3D conductivity model retrieved by the 1D deterministic approach (Figure 2-7b and 7f); (b) The 3D conductivity model obtained via the stochastic inversion accounting for the modelling error (Figure 2-7c and g). Each of the 50 plotted time-gates (channels) is depicted with a different color (for clarity, the last 4 channels – 51 to 54 – are not shown).

2.2.2. Test 2: 3D conductivity distribution with heterogeneous layers

In test 2, we apply the same strategy to a more elaborated 3D conductivity model. test 2's model consists of three layers with similar geometries as in test 1, but, now, characterized by heterogeneous conductivity values (Figure 2-9). For sake of completeness, analogously to what has been done for test 1, also for test 2, we show the 3D responses (Figure 2-10c) along the central profile (Figure 2-10a) of the 3D conductivity model (Figure 2-9a). And, in Figure 2-10b, we display the 1D response as they would result by considering each column of the true conductivity model as independent (for comparison, kindly, see Figure 2-2b concerning test 1). Clearly, for test 2, the importance of taking into account the modelling error is even more evident: the error we introduce when interpreting the 3D model response in terms of 1D data is never below 4% (blue line in Figure 2-10b).

Figure 2-11a presents the result of Occam's inversion of the 3D data (Figure 2-10c). Again, from Figure 2-11b, it is clear that it is not difficult to perfectly fit the 3D data with 1D responses, even with a model barely capable to get the very major features of the conductivity model to be inferred. Also, for this more complex test, a 1D stochastic inversion can be performed by following the previously discussed Metropolis approach making use of precalculated samples. The 10^5 realizations of the prior distribution are very similar to those shown in Figure 2-4 for test 1; the only difference is that, consistently with the new model to be reconstructed, also for the prior realizations, the conductivity of each layer is allowed to vary. Figure 2-12 shows the mean map of

the posterior distribution obtained without taking into consideration the modelling error; as for Figure 2-5 (about test 1), also for test 2, the retrieved mean model (Figure 2-12a) does not capture the lateral variation of the top of the deepest layer and smooth the large majority of the incisions out. And, maybe, worse than that is the fact that, as showed by the standard deviations of the conductivity of each layer (plotted in Figure 2-12b), the leveled-out reconstruction is given for (almost) undeniable.

On the contrary, if we take into account the modelling error, the mean map derived from the 1D stochastic inversion provides a quite satisfactory reconstruction of the true model with all its complex morphology (Figure 2-13a), and when the inferred mean conductivity values do not reflect the true distribution, they are associated with high levels of uncertainty (for example at depth ~100 m and X ~1300 m in Figure 2-13b).

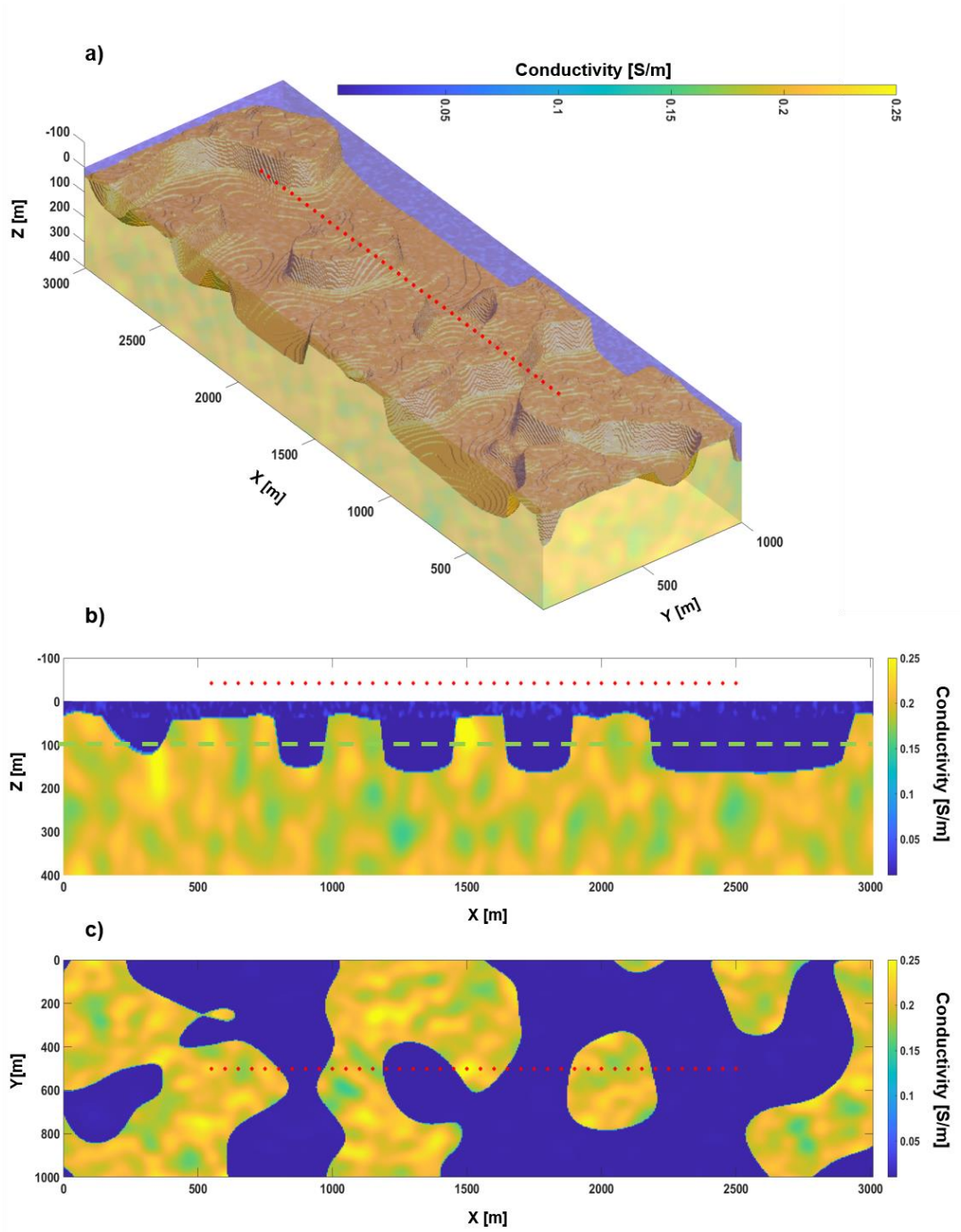

Figure 2-9. Conductivity distribution for test 2: (a) 3D view of the model consisting of a sequence of three heterogeneous layers with varying thicknesses; (b) Vertical section of the model in panel (a), along the survey line highlighted by the red dots indicating the locations of the ATEM soundings; (c) Plain view at 100 m depth (dash green line in panel (b)).

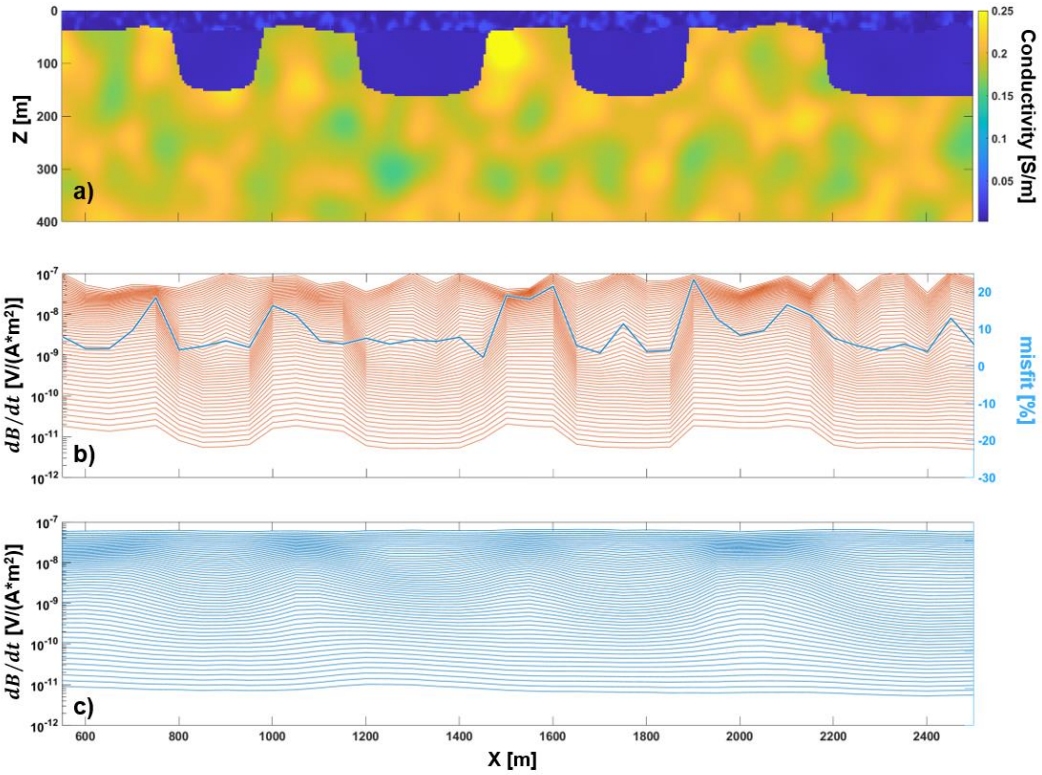

Figure 2-10. Comparison of the 3D and 1D responses for the conductivity model of test 2: (a) Vertical section of the 3D conductivity model in Figure 2-9a (it is a portion of the section in Figure 2-9b); (b) 1D responses calculated for the 1D portions of the original model in Figure 2-9a at the locations of the ATEM soundings (red dots in Figure 2-9b) – the blue line represents, sounding-by-sounding, the relative misfit between the 1D and 3D responses (the corresponding axis is on the right in blue); (c) 3D responses measured at the same location in panel (b), but, here, calculated for the entire 3D conductivity model (Figure 2-9a).

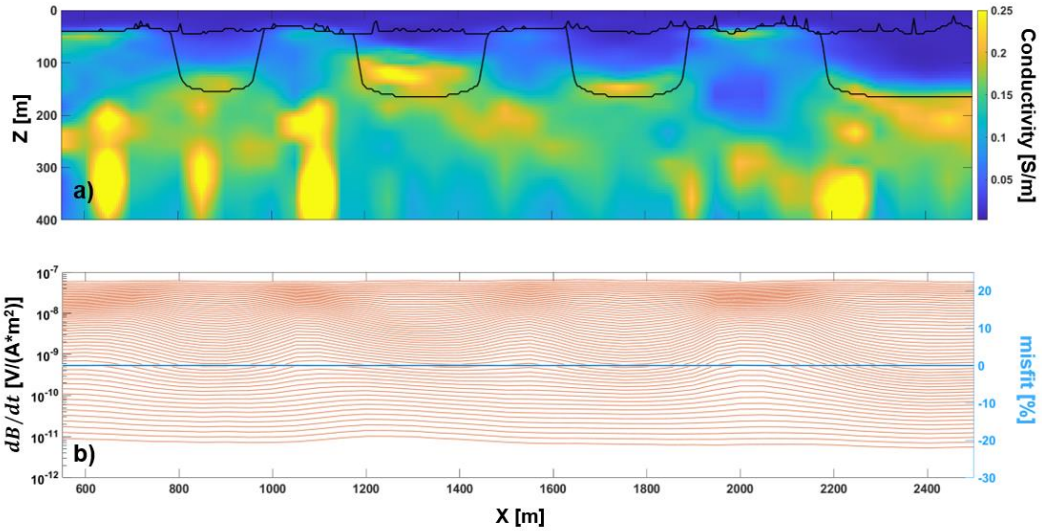

Figure 2-11. 1D deterministic inversion of the 3D data (Figure 2-10c) associated to the conductivity model of test 2 (Figure 2-9a): (a) The solution of the 1D deterministic inversion – the black lines show the interfaces of the original conductivity model to be reconstructed; (b) The 1D responses resulting from the conductivity model in panel (a) – the blue line represents, sounding-by-sounding, the relative misfit between the 3D and 1D responses (the corresponding axis is on the right in blue).

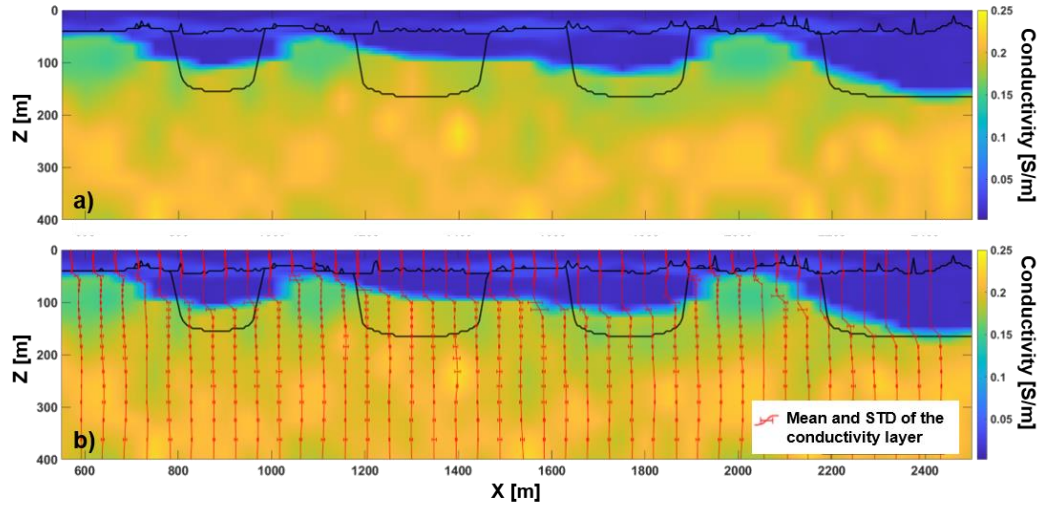

Figure 2-12. (a) Mean map of the 1D stochastic inversion of the 3D data (Figure 2-10c) associated to the conductivity model of test 2 (Figure 2-10a shows one vertical section of that 3D conductivity model). In this case, realistic prior is used, but no modelling error has been taken into account. The black lines show the locations of the interfaces to be reconstructed. (b) The same reconstructed conductivity distribution as in panel (a), but, now, with, superimposed, the mean and standard deviation vertical profile for each vertical conductivity profile.

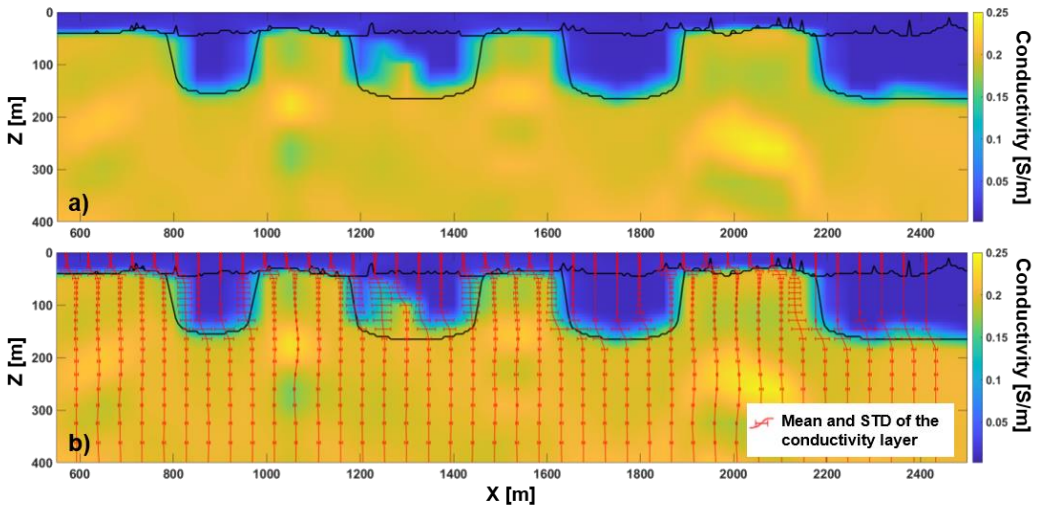

Figure 2-13. (a) Mean map of the 1D stochastic inversion of the 3D data (Figure 2-10c) associated to the conductivity model of test 2 (Figure 2-10a shows one vertical section of that 3D conductivity model). In this case, realistic prior is used together with the modelling error assessment. The black lines show the locations of the interfaces to be reconstructed. (b) The same reconstructed conductivity distribution as in panel (a), but, now, with, superimposed, the mean and standard deviation vertical profiles.

2.3. Analysis of the inversion parameters

Are 10^5 samples from the prior enough to guarantee the convergence of the stochastic inversions? What about the subset of 500 prior 3D realizations used for the assessment of the modelling error for the geological settings considered? Is the retrieved modelling error Gaussian as it should be to be able to use the proposed inversion scheme? In this section, we try to answer all these legitimate questions.

2.3.1. About the numerosity of the prior samples for the convergency of the stochastic inversion

Since the propositional scheme of the adopted Metropolis approach is based on a finite number of precalculated samples of the prior, it is important to establish if the abundance of those samples is sufficient to guarantee the convergence. In this respect, we run several inversions characterized by an increasing number of prior's samples. From Figure 2-14f-h, it is evident that, at least for the simple problem of test 1, convergence is reached with a numerosity of the prior samples of a few thousand. Hence, an abundance of two orders of magnitude higher should reasonably be compatible with our goal. A similar conclusion can be deduced by considering the evolution of the correlation coefficient between the depth of the deepest interface inferred and the true one as showed in Figure 2-15.

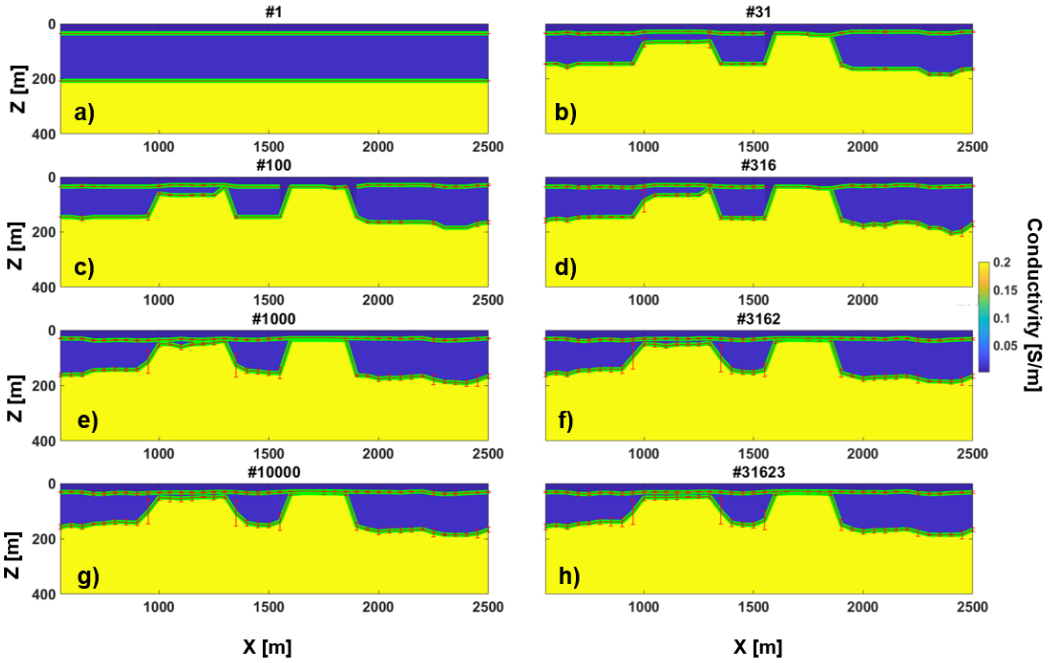

Figure 2-14. Result of the extended Metropolis inversion as a function of the numerosity of the considered precalculated prior samples (the title of each panel reports that numerosity). Clearly, here, we are incorporating the information about the modelling error into the inversion of test 1's data.

2.3.2. About the numerosity of the prior's samples for the estimation of the modelling error

Still considering test 1's dataset, we try to set up a strategy for the evaluation of the minimum number of realizations of the prior to be considered for an effective assessment of the modelling error. For all the tests performed in the present research, a maximum number of 500 models (similar to those in Figure 2-4) have been used to calculate the difference $\boldsymbol{D}_{diff}$ and, in turn, the parameters defining the Gaussian probability density $\mathcal{N}(\mathbf{d}_\Delta, \boldsymbol{C}_\Delta)$ describing the modelling error. If we consider the behavior of the mean vector $\mathbf{d}_\Delta$ calculated for an increasing number of samples number N_Δ, we can plot the results as in Figure 2-16a; from that figure, it appears evident that the assessment of $\mathbf{d}_\Delta$ reaches significant stability after considering a few hundred of realizations of the prior.

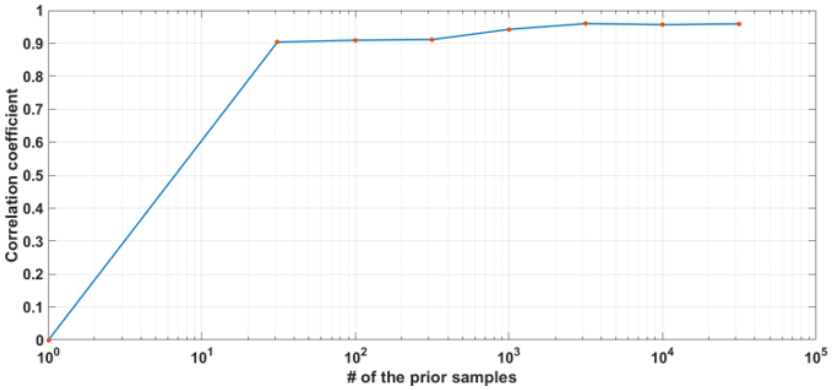

Figure 2-15. Correlation coefficient between the retrieved and the true depth of the deepest layer as a function of the number of precalculated samples of the prior. Clearly, as for Figure 2-14, we are considering the stochastic inversion with modelling error assessment applied to test 1's dataset.

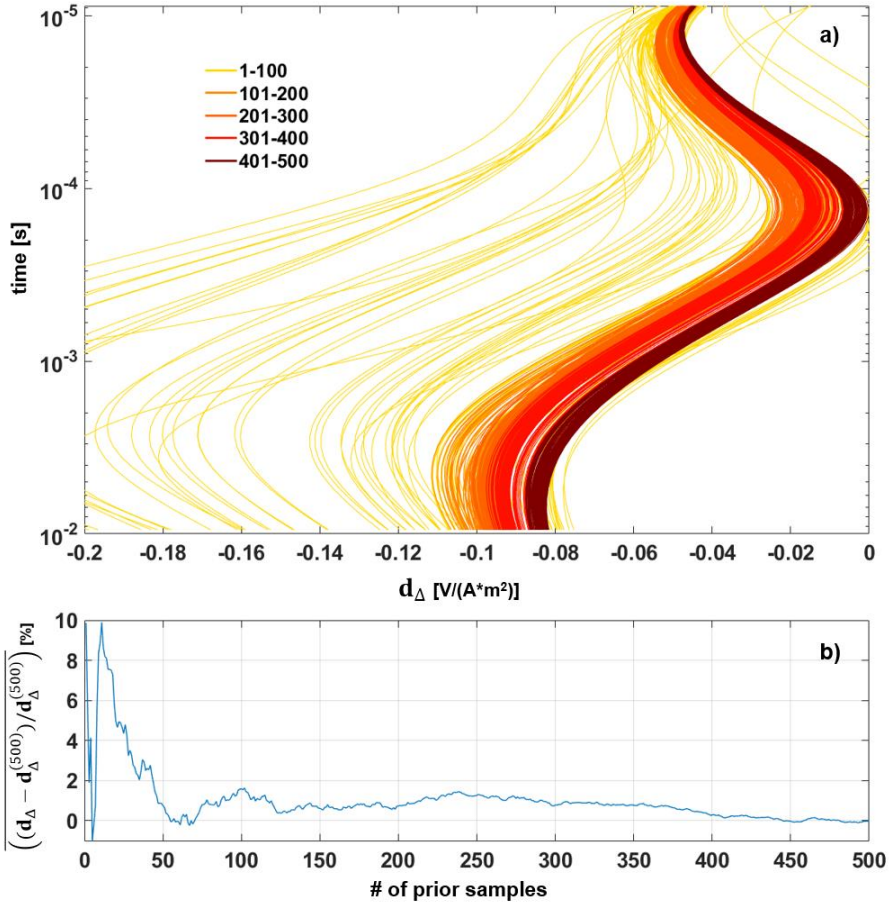

Figure 2-16. Mean of the modelling error as the number of the prior samples used for its estimation increases: (a) the mean $\mathbf{d}_\Delta$ vectors calculated for a number of prior samples ranging, for example, from 1 to 100 are represented by the solid yellow lines, whereas, considering another example, for a number of prior samples between 401 and 500, the same results for the $\mathbf{d}_\Delta$ vectors are plotted in dark red. (b) shows the behavior of the mean misfit between the estimated $\mathbf{d}_\Delta$ and our best assessment $\mathbf{d}_\Delta^{(500)}$ (based on 500 realizations).

A similar conclusion can be even more directly deduced by checking Figure 2-16b, in which the mean of the difference between $\mathbf{d}_\Delta$ and its best estimation $\mathbf{d}_\Delta^{(500)}$ (based on $N_\Delta = 500$ realizations) is plotted against the increasing numerosity N_Δ: approximately after considering 400 samples, $\mathbf{d}_\Delta$ does not show significant variations.

Regarding the evolution of the covariance matrix $\boldsymbol{C}_\Delta$, we can, again, study how it changes over the number of prior samples. Figure 2-17 demonstrates, once more, that, for the considered case, N_Δ =500 should guarantee a reasonable estimation of the modelling error. In particular Figure 2-17b shows that the estimation of $\boldsymbol{C}_\Delta$ has already reached convergence after considering ~400 samples.

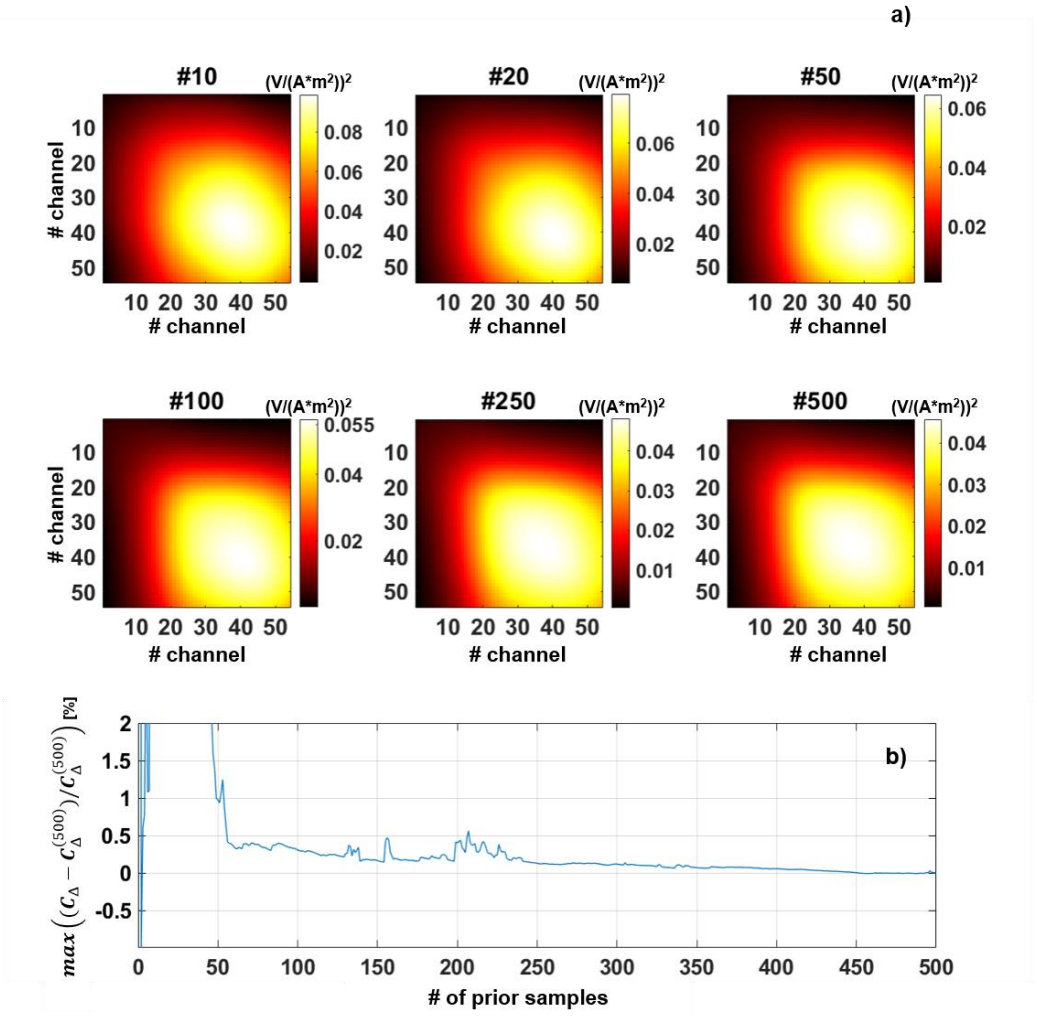

Figure 2-17. Covariance $\boldsymbol{C}_\Delta$ of the modelling error as the number of prior samples used for its estimation increases: (a) different $\boldsymbol{C}_\Delta$'s calculated for the number of prior samples indicated by the title of each subpanel (from $\boldsymbol{N}_\Delta$=10 for the panel on the top-left to $\boldsymbol{N}_\Delta$=500 for our best estimation on the bottom-right corner of panel (a)). (b) shows the behavior of the maximum misfit between all the components of the matrix $\boldsymbol{C}_\Delta$ and the corresponding $\boldsymbol{C}_\Delta^{(500)}$ based on our maximum number of realizations ($\boldsymbol{N}_\Delta$=500).

2.3.3. About the Gaussianity of the modelling error

As mentioned before, the proposed approach is based on the assumption that the modelling error is actually Gaussian. In this section, we demonstrate that this working hypothesis is largely met. In this respect, each subpanel of Figure 2-18 shows one of the 54 histograms (one for each time-gate) of the corresponding component of the vector $\boldsymbol{D}_{diff}$ of the difference between the 3D and 1D responses calculated for the 500 realizations used for the modelling error assessment. In particular, the red lines represent the Gaussian that is better fitting the experimental histograms, whereas the black lines show the Gaussian profile as inferred from the distribution $\mathcal{N}(\mathbf{d}_{\Delta}, \boldsymbol{C}_{\Delta})$. It is worth noticing the excellent agreement between the black and red curves, but, more than that, the fact that for the large majority of the time-gates the modelling error is indeed compatible with Gaussian distributions. Surprisingly, the histograms for the late channels (in particular those for i going from ~49 to 54 – i.e., basically the last row of Figure 2-18) show some sort of bimodal behavior whose possible justification is not evident. A possible reason might be connected with the finite size of the 3D simulation domain. However, this highly hypothetical guess will need to be investigated and verified.

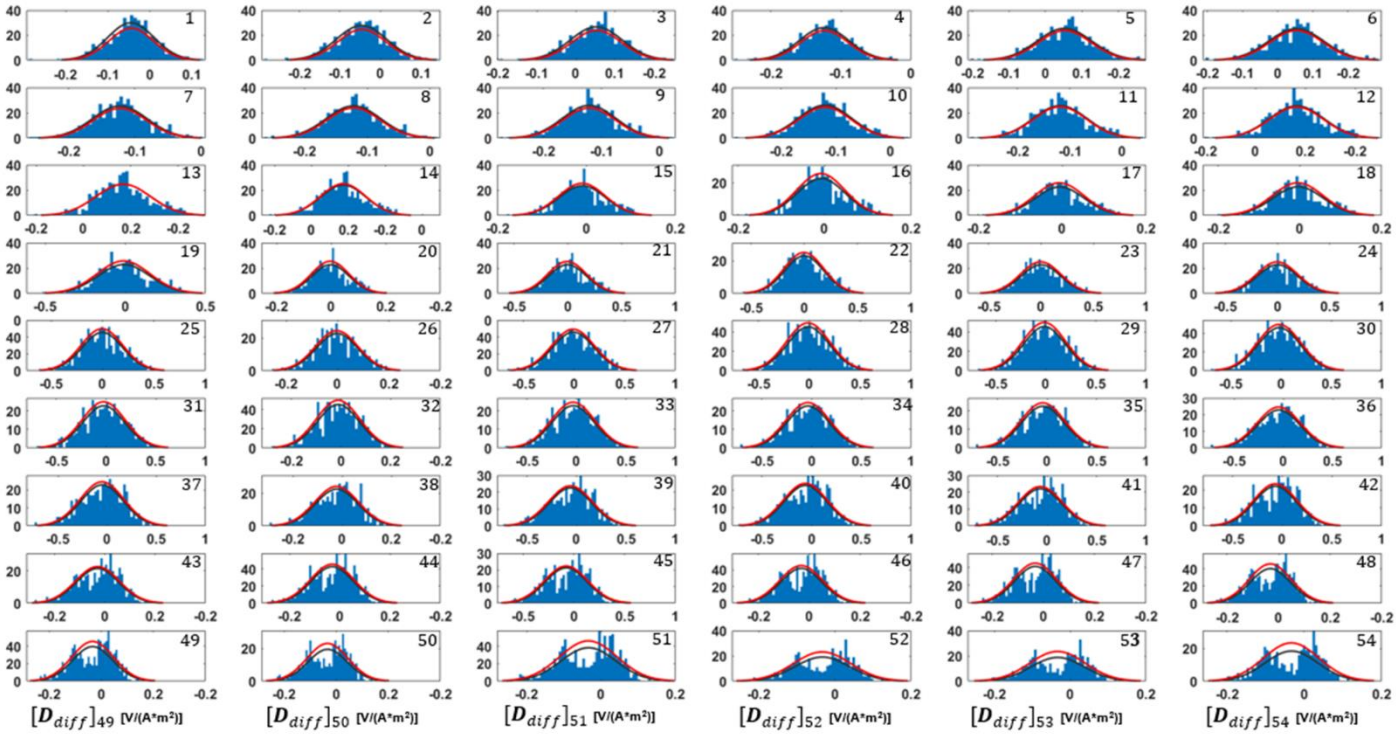

Figure 2-18**.** Each panel j (with j, time-gate's index, varying from 1 to 54) shows the histogram of the corresponding component $[\boldsymbol{D}_{diff}]_j$ of the difference between the 3D and 1D responses for the 500 samples of the prior used for the modeling error estimation. The solid black line is the Gaussian curve better fitting the histogram, whereas the red line is the Gaussian derived by $\mathcal{N}(\mathbf{d}_{\Delta}, \boldsymbol{C}_{\Delta})$.

2.4. Field test

In this section, we show an application on a field dataset of the proposed approach for 1D

stochastic inversion with realistic prior and accounting for the forward modeling error. Like for the above synthetic tests, we use the solution of standard 1D deterministic inversion as a benchmark.

In the considered survey area, the major host and wall rock units of the deposit comprise peridotite, breccia, and volcaniclastic units. Among the wall rock, there are sulfide deposits distributed in massive forms. Massive sulfide deposits are significant sources of Zn, Cu and Ag, Au and other metals. Therefore, Massive sulfides, likely to be highly conductive, are the main targets for the AEM exploration. Clearly, one of the main problems here is the reliable reconstruction of a highly 3D environment, by using efficient forward.

2.4.1. Deterministic Occam's inversion

Figure 2-20 (a) and Figure 2-21 (a) show the result of 1D deterministic inversion - implementing an Occam's regularization strategy (specifically, the Spatially Constrained Inversion - SCI). The deterministic inversion reconstruction is characterized by a high conductivity body (anomaly) embedded in a heterogeneous background significantly more resistive, and, in which, two main structures can be easily detected; in particular, a deepening unit (of approximately 0.0035 S/m) that, roughly speaking, leaves the surface (at small X values) and intersects the most conductive anomaly at Z ~200 m. The shape of the conductive anomaly is characterized by the typical features known as pant-legs artefacts. This makes it particularly evident that the deterministic inversion is definitely distorted by 3D effects due to the sub-optimal forward modelling.

Concerning the data misfit, observations are easy to fit by using the 1D forward response (as showed in Figure 2-22). Nevertheless, when we calculate the 3D responses corresponding to the result retrieved via the deterministic 1D inversion, and we compare them against the actual measurements, we can notice the obvious increase of the relative data misfit (Figure 2-23). More specifically, Figure 2-23a shows the 3D responses of the 1D SCI result calculated at the locations (red dots – upper line - in Figure 2-21a) above the retrieved anomaly ($Y = 500\,m$). The blue line in Figure 2-23a is the chi-square (χ^2) curve between the 3D forward responses and the observed data. Clearly, the "actual" χ^2 based on the 3D responses, in particular over the anomaly location, is significantly higher.

2.4.2. Stochastic inversion without modeling error assessment

Following the same approach tested before on the synthetic dataset, we created a 4-category prior; the categories correspond to the geological units characterizing the investigated site: peridotite; breccia; volcanoclastic and massive sulfide. The geometries and mutual positions of the four categories within each realization of the prior distribution are stochastically modeled in accordance with available geological knowledge of the area. Nine realizations of such a prior are showed in Figure 2-19a. For each category, a distribution of the possible conductivity values has been defined as showed in Figure 2-19b. It is worth noticing that, despite the curves in Figure 2-19b are calculated for $\boldsymbol{N_{\Delta}}$=500 - with 500 being the number of samples used for the subsequent modelling error estimation, for the 1D stochastic inversion, $5 * 10^5$ realizations have been used instead. In

practice, as we did before, the 1D samples of the prior have been picked as the central 1D model of each 3D realization (the picking locations of the 1D models for the nine examples in Figure 2-19a are indicated with black dot).

Figure 2-20b and Figure 2-21b shows the mean map of the posterior distribution retrieved by the 1D stochastic inversion (still, not taking into account the 1D modeling error). The prior knowledge definitely impacts the final results. This is particularly evident by comparing the horizontal slice at $Z = 250$ m of the deterministic result (Figure 2-21a) against the mean map of the stochastic inversion (Figure 2-21b): the conductive body has moved towards larger Y locations. For example, by analyzing the vertical sections at $Y = 800$ (Figure 2-20a-b), whereas no conductive body appears in the deterministic reconstruction, a very conductive anomaly is clearly visible in the stochastic result.

These differences are even more impressive as the data misfits (calculated as the difference between the 3D responses of the solutions) lead to very similar χ^2 values (please, see Figure 2-23a-b).

Actually, by comparing the responses also along the section at Y = 700 m (Figure 2-24) - where, accordingly to the deterministic smooth inversion, the conductive body is barely visible at the bottom of the vertical section (Figure 2-20a), whereas, for the stochastic inversion reconstruction (Figure 2-20b), the anomaly should be significantly shallower - the data misfit (blue line in Figure 2-24b) of the stochastic mean model is on the same range of the deterministic χ^2 (blue line in Figure 2-24a).

2.4.3. Stochastic inversion incorporating the 1D modelling error

What happens when, we include, into the stochastic inversion, also the modelling error associated with the prior we are using for the inversion?

To answer this question, we estimated the mean $\mathbf{d}_\Delta$ and covariance $\boldsymbol{C}_\Delta$ of the modeling error consistent with the 3D prior samples (Figure 2-19) similarly to what we discussed regarding the synthetic test. The calculated covariance $\boldsymbol{C}_\Delta$ is showed in Figure 2-25 and it is clearly very different, both in shape and in values, with respect to its "synthetic" counterpart (Figure 2-17). This is consistent with the much more complex (and much three dimensional) geological settings we are dealing with now.

Figure 2-20c and Figure 2-21c show the mean map resulting from the 1D stochastic inversion incorporating the modeling error: the conductive anomaly is way more focused than in the previous two reconstructions (Figure 2-20a-b and Figure 2-21 a-b) and appears uniquely at $Y = 700$ m and $Y = 800$ m, at relatively shallow depths. In addition, the rest of the investigated volume appears to be quite homogeneous. Clearly, this does not mean that the background is indeed homogeneous, but, simply, that, across all the realizations of the posterior, the features not

affecting significantly the data are largely averaged away. This fact is evident in the probability plot of each category in Figure 2-27 (discussed in more details in the next section).

It is worth highlighting that data misfit for the stochastic inversion with modeling error (Figure 2-23c) is much lower than those of the previous two inversion results (Figure 2-23a-b) across the locations where the conductive anomaly seems to be accordingly to the deterministic result ($Y = 500\ m$ in Figure 2-21a-b). Of course, the assumed noise of the stochastic inversion accounting for the modelling error is significantly higher than for the other two inversion strategies: in the panels (c) of Figure 2-23 and Figure 2-24, the data noise does not include only the random component but also the correlated portion due to the 1D modelling approximation. Still, where, accordingly to the deterministic and stochastic inversion without modelling error, the massive sulfide anomaly should be (Figure 2-21a), the agreement with the observed data is in larger in the case of the proposed scheme (Figure 2-23c) compared to the in the "standard" approaches (Figure 2-23a-b).

On the other hand, the χ^2 values in Figure 2-24c (Y= 700 m) is slightly higher than those in Figure 2-24a-b and homogeneously distributed with no difference between areas where we are almost sure to find the sulfide anomaly or not (Figure 2-27).

2.4.4. Stochastic inversion (w/ and w/o 1D modelling error) as petrophysical inversion tool

Because of the way the stochastic inversions have been designed and implemented, they can naturally provide information directly about the categories rather than the conductivity values. This is another, very significant, advantage with respect to the more traditional deterministic inversion. In fact, the prior is defined throughout realizations in which each category can be labelled with a conductivity value (accordingly to the distribution in Figure 2-19b), and retrieving the conductivity, automatically, implies that we are capable to reconstruct the distributions of the categories as well.

Figure 2-26 and Figure 2-27 demonstrate that we can easily infer what we are more interested in: the category rather than the conductivity distribution. In particular, Figure 2-26 and Figure 2-27 show the probability of having each category (panel (a) - volcaniclastic; panel (b) – peridotite; panel (c) – breccia lithologies and panel (d) - massive sulfide rocks) as retrieved by the stochastic inversion, respectively, without and with modelling error.

By comparing the probability of having massive sulfide rocks in Figure 2-26d and Figure 2-27d, it is clear how the presence of this type of rock is associated with high level of conductivity and that the probability map concerning the massive sulfide is in agreement with our previous conclusions; i.e., the stochastic inversion with modelling error detects the massive sulfide inclusion between $Y = 700$ and $Y = 800$ m (in contrast with the deterministic SCI inversion).

On the other hand, the other categories (Figure 2-27a-c) are characterized by an almost homogeneous probability across the entire investigated volume (except, of course, where the

presence of the massive sulfide rock is certain), which means that, except for the anomaly, the other conductivity features have a very high level of uncertainty.

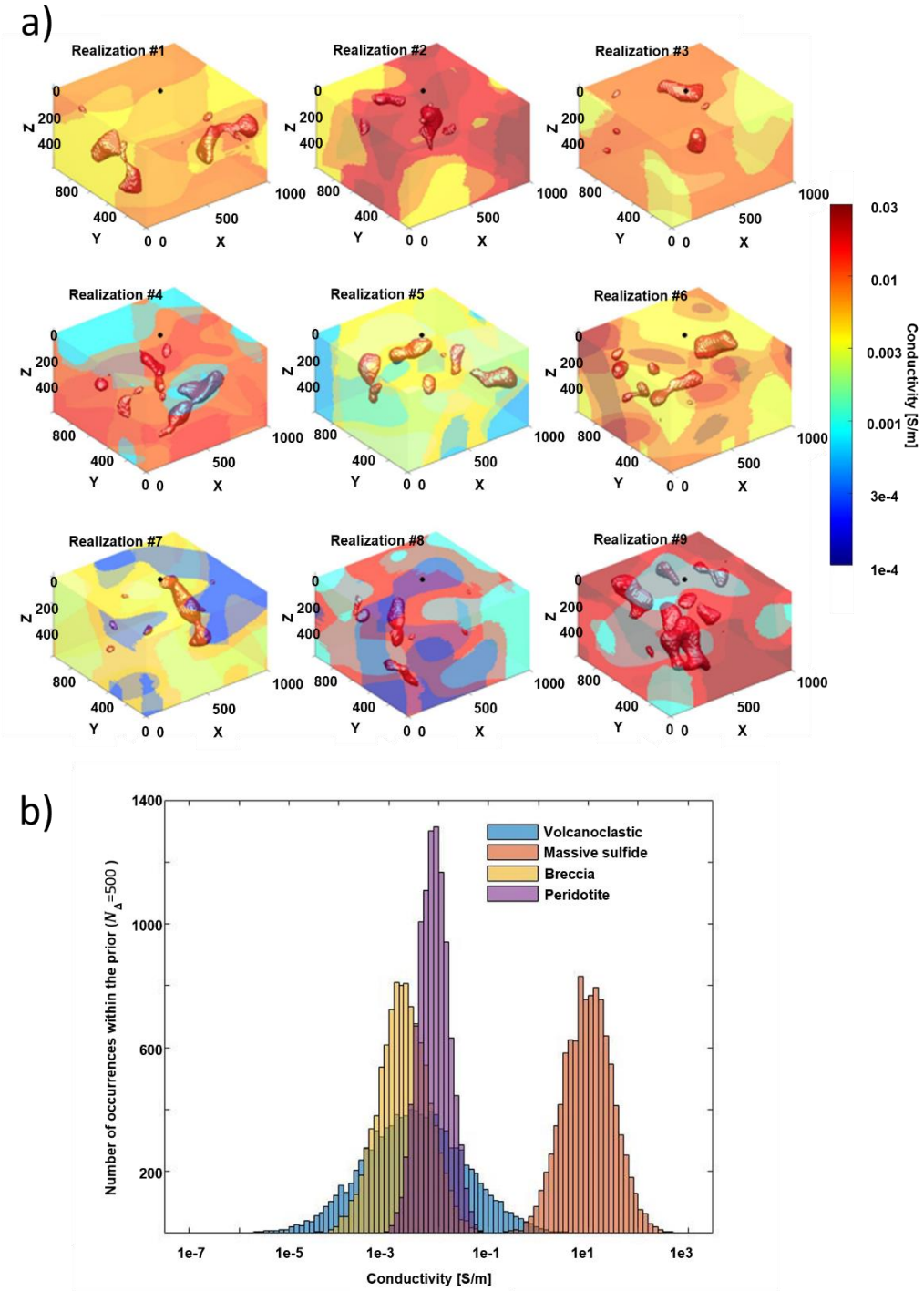

Figure 2-19. (a) Nine samples of the prior 4-category distribution used for the stochastic inversion of field data (and, consistently, used also for the modelling error estimation). (b) Conductivity distributions of the 4 categories as they are in the 500 realizations defining the N_Δ=500 prior.

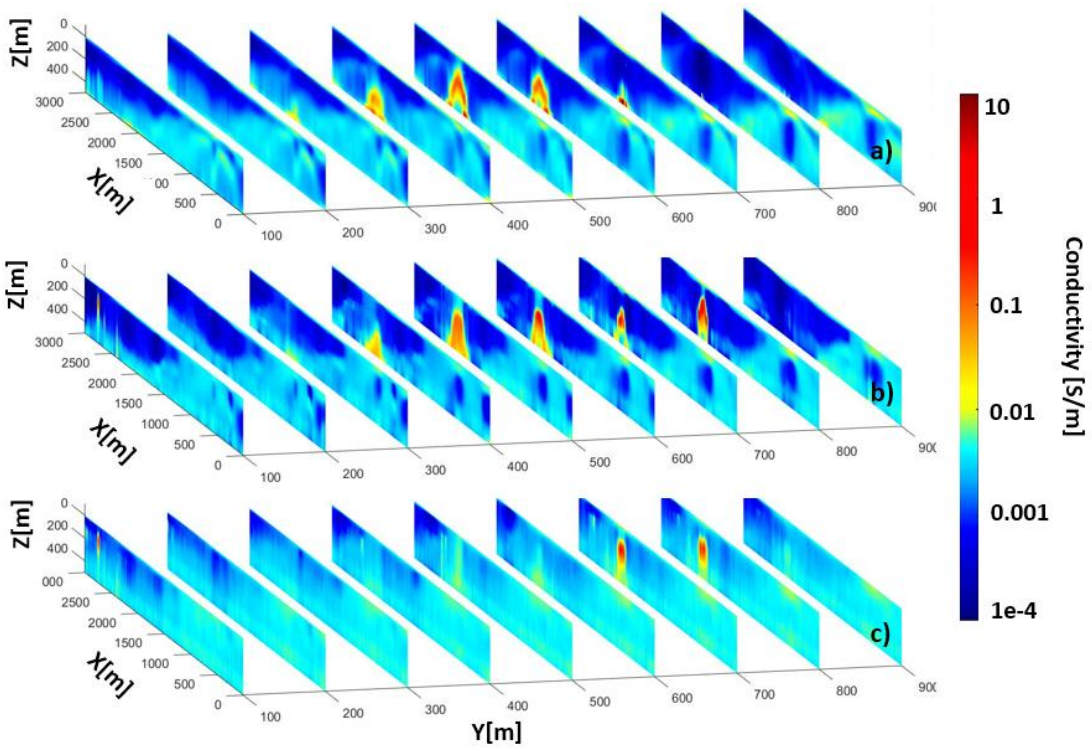

Figure 2-20. The inversion results (vertical section of the inversion model) of the observed data from the survey area and obtained with: (a) 1D deterministic Occam's inversion; (b) 1D stochastic inversion without taking into account modeling error and (c) 1D stochastic inversion (specifically, the mean map) taking into account modeling error.

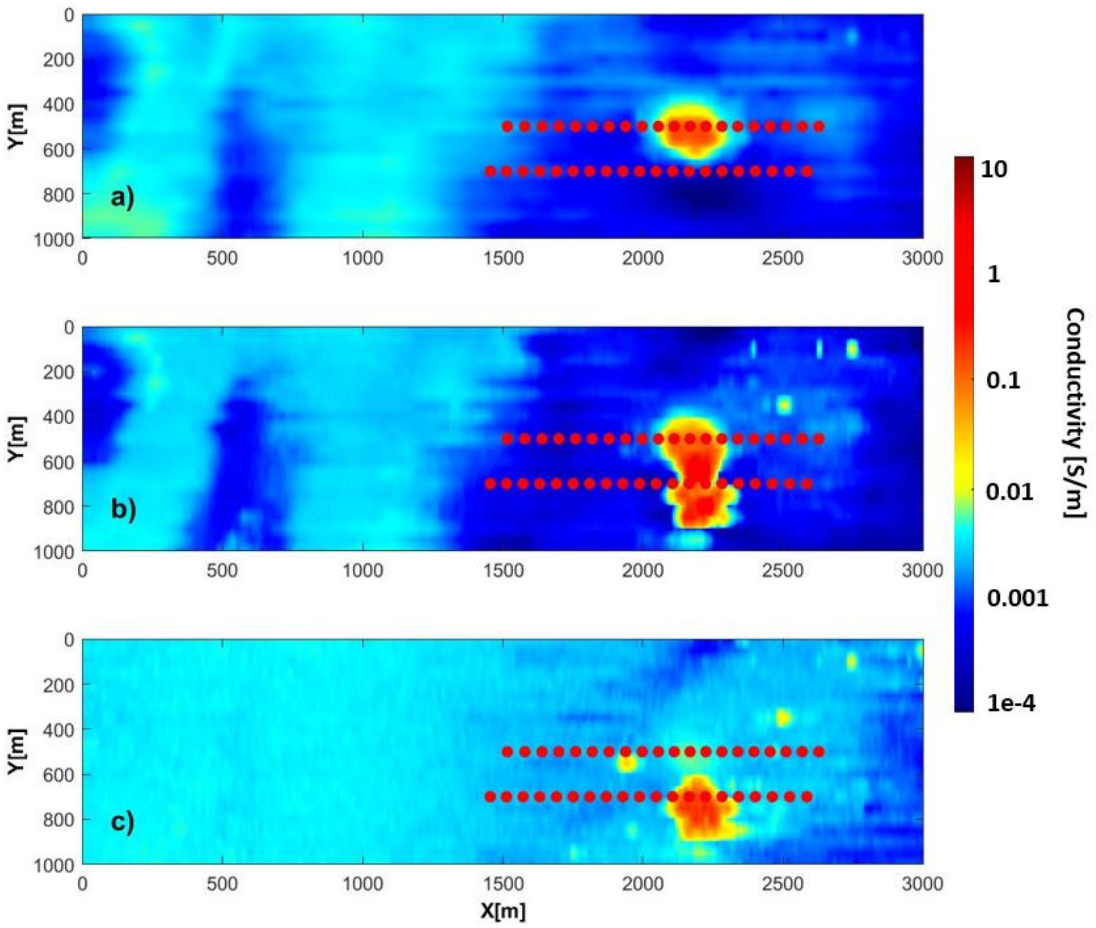

Figure 2-21. The plain view (at 250m depth) of the inversion results associated with Figure 2-20: (a) the conductivity model of 1D deterministic Occam's inversion; (b) the conductivity model (mean map) of 1D stochastic inversion without taking into account modeling error, and (c) the conductivity model (mean map) of 1D stochastic inversion taking into account modeling error. The red dots are the locations where we calculated the 3D forward responses for each inversion result (Figure 2-23 and Figure 2-24).

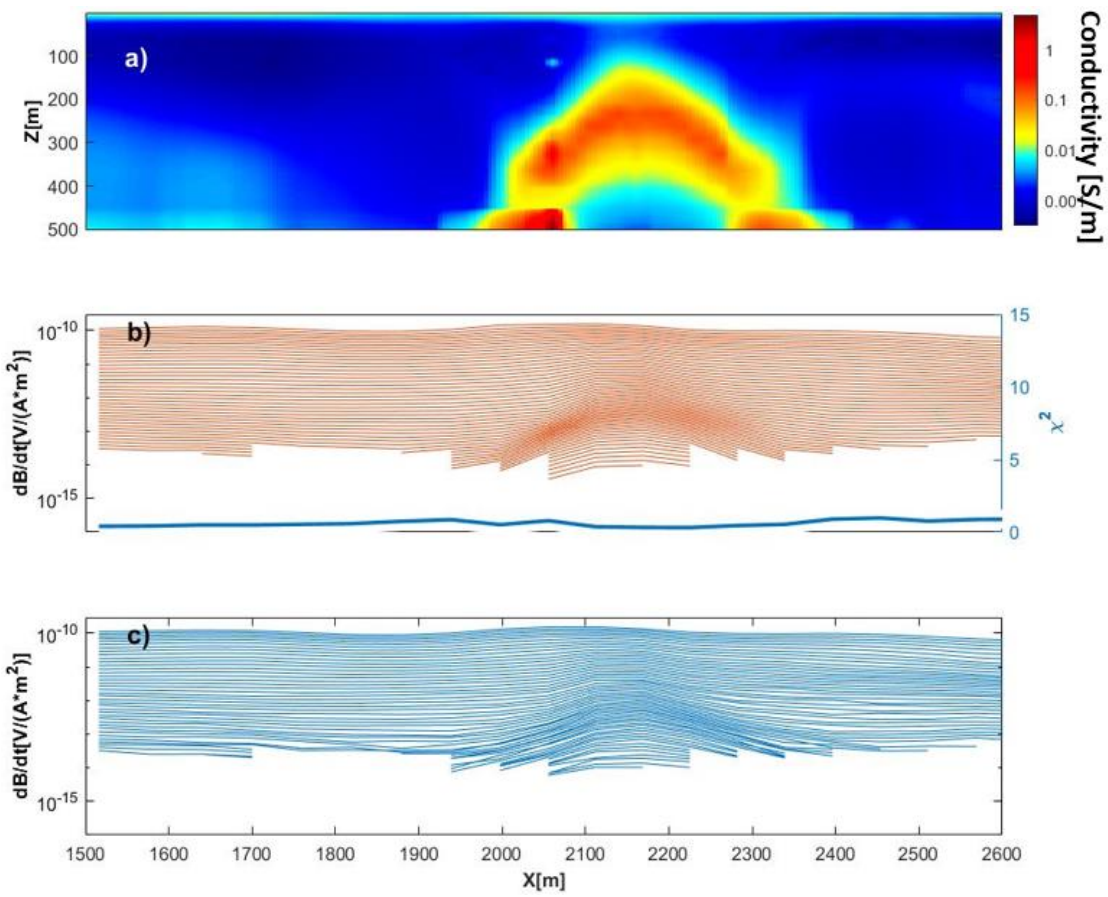

Figure 2-22. Comparison of the observed data and 1D responses for the deterministic conductivity model in Figure 2-20a: (a) Vertical section of the conductivity model in Figure 2-20a (at $Y = 500$ m); (b) 1D responses calculated for the conductivity model in Figure 2-20a (the simulation locations are indicated by the upper row (Y= 500 m) of red dots in Figure 2-21a) – the blue line in the panel (b) represents, sounding-by-sounding, the relative misfit between the observation and 1D responses (the corresponding axis is on the right, in blue); (c) the observation measured at the same location in panel (b).

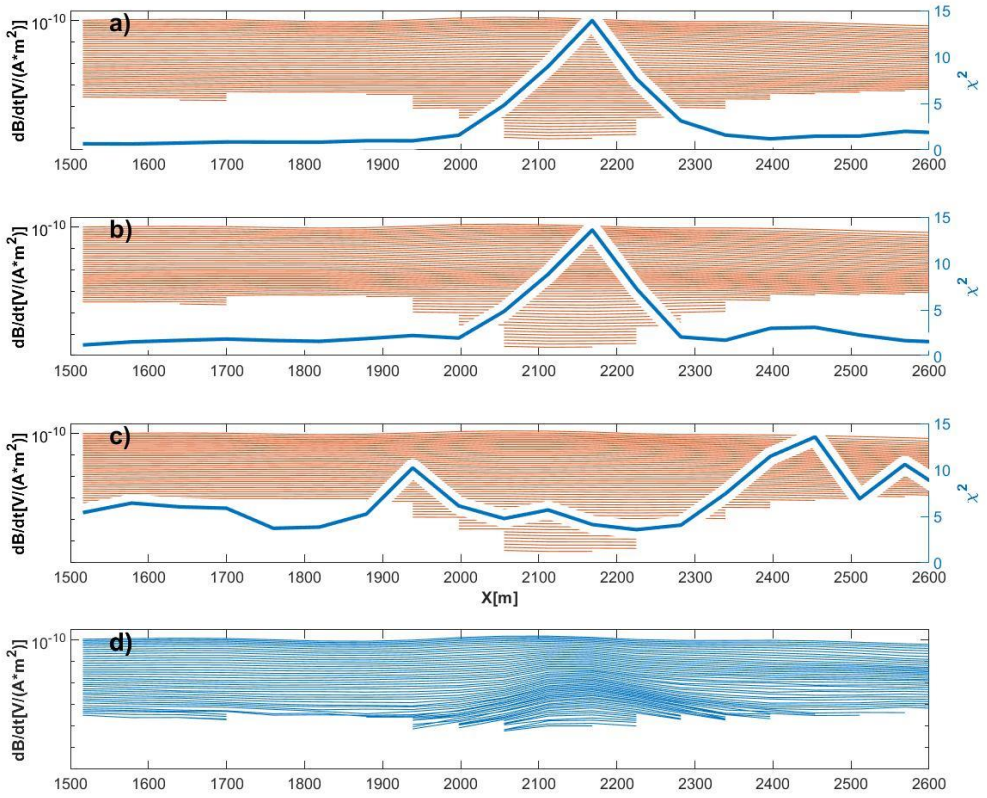

Figure 2-23. Comparison between the observed data - panel (d) - and 3D forward responses calculated from: (a) the 3D conductivity model retrieved by the 1D deterministic approach – the simulation locations are indicated by the upper row (Y= 500 m) of red dots in Figure 2-21a; (b) the 3D conductivity (mean) model from the stochastic inversion not accounting for the modeling error; (c) the 3D (mean) conductivity model from the stochastic inversion now accounting for the modeling error. The blue lines in the panels (a-c) are the χ^2 between the observed data and corresponding 3D forward responses.

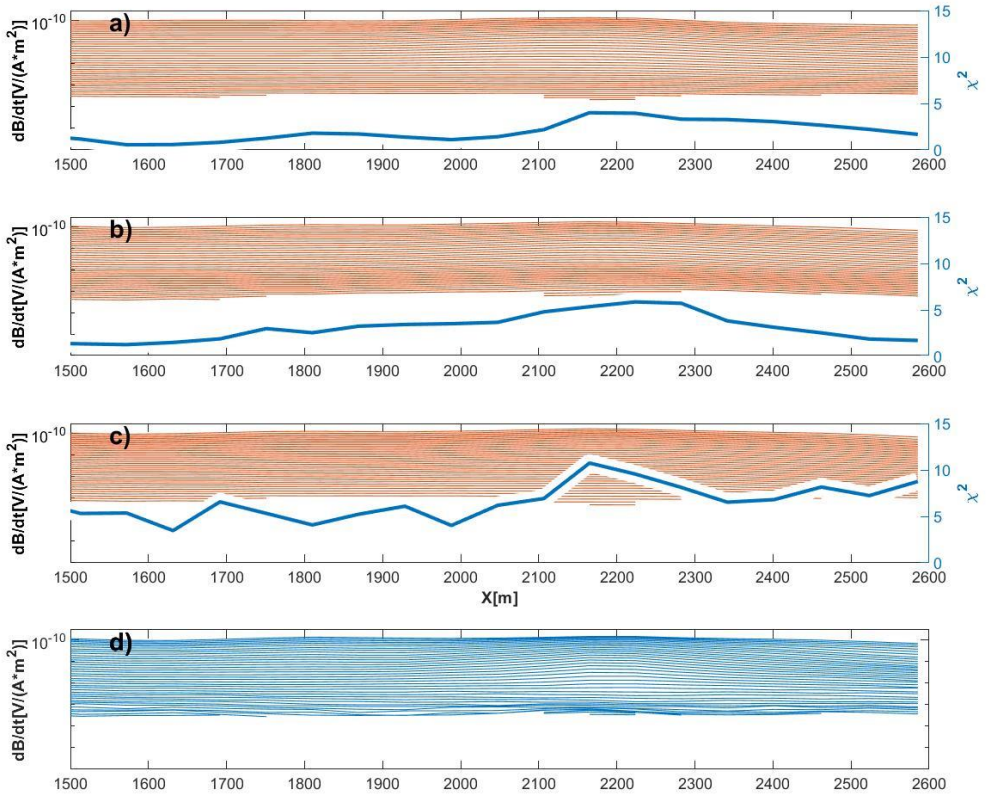

Figure 2-24. Comparison between the observed data - panel (d) - and 3D forward responses calculated from: (a) the 3D conductivity model retrieved by the 1D deterministic approach – the simulation locations are indicated by the lower row (Y= 700 m) of red dots in Figure 2-21a; (b) the (mean) 3D conductivity model obtained via the stochastic inversion without accounting for the modeling error; (c) the (mean) 3D conductivity model obtained via the stochastic inversion accounting for the modeling error. The blue lines in the panels (a-c) are the χ^2 between the observed data and corresponding 3D forward responses.

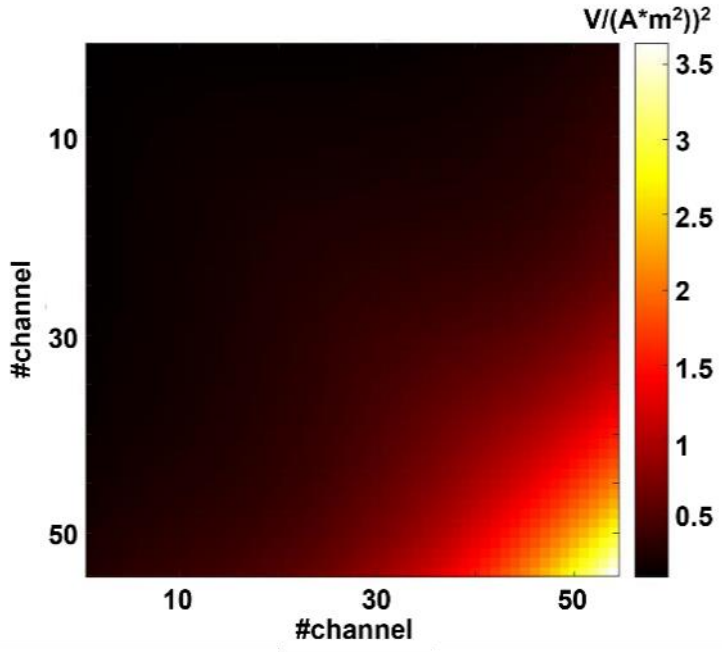

Figure 2-25. Covariance $\boldsymbol{C_\Delta}$ of the modelling error calculated based on 500 samples of the prior (nine of which are showed in Figure 2-19b)

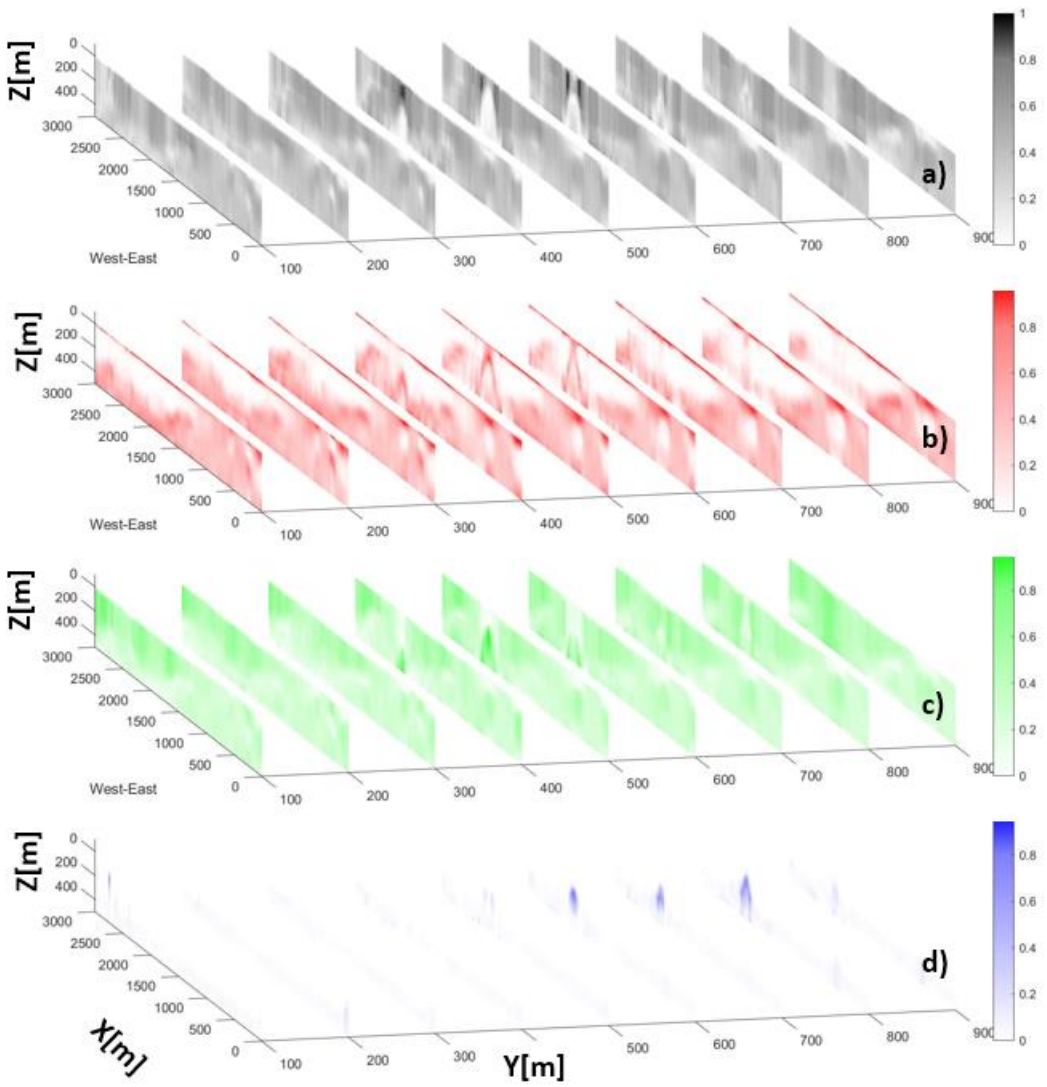

Figure 2-26. Probability associated with the category (for the stochastic inversion without modeling error): (a) volcaniclastic, (b) peridotite, (c) breccia and (d) massive sulfide.

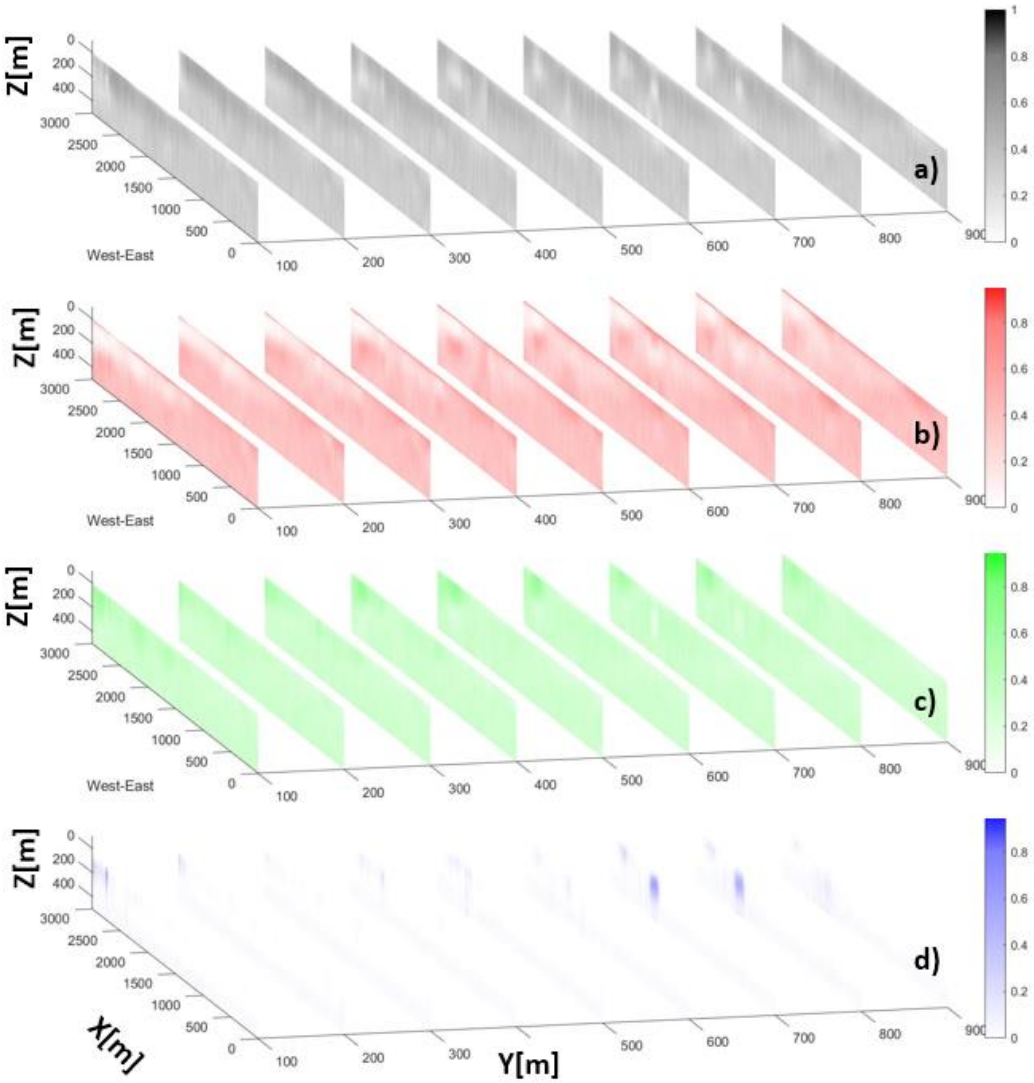

Figure 2-27. Probability associated with the category (for the stochastic inversion with modeling error): (a) volcaniclastic, (b) peridotite, (c) breccia and (d) massive sulfide.

2.5. Summary

Throughout this chapter, two synthetic and one field tests are used to demonstrate the capabilities (and limitations) of stochastic inversion with geologically informed prior distribution to properly reconstruct the complex target conductivity distributions and the associated uncertainties.

In particular, we show how crucial the correct quantification of the modelling error (based on the prior choices) is. In our specific cases, we deal with ATEM data inverted via a 1D stochastic approach with realistic prior and with the assessment of the corresponding modelling error. In the synthetic examples, we test our approach on data mimicking the collection of VTEM measurements over geologies recalling glacial sedimentary environments typical, for example, of some regions in Northern Europe. Regarding the field measurements, they are VTEM data acquired for mineral exploration purposes on quite complex highly 3D geologies. The conclusion is that, even in the case of stochastic approaches (already improving the results, for example, when compared with 1D

deterministic approaches relying merely on the regularization term for including the prior knowledge about the targets), neglecting the fact that we are using a brute 1D approximation, instead of a more sophisticated 3D one, leads to unrealistically low level of uncertainty in correspondence of those features that might turn out to be just artifacts. On the other hand, the assessment (and utilization) of the modelling error allows a more effective reconstruction of the true models and their associated reliability levels.

This research shows how the initial working hypotheses – concerning the minimum possible number of realizations defining the prior distribution and the numerosity of the smallest subset useful for an effective estimation of the modelling error – can be checked. Moreover, also the ansatz regarding the Gaussianity of the modelling error is largely verified (even if it is not shown here, the Gaussianity test for the field measurement inversion led to similar conclusion with respect to the synthetic cases).

Thus, the discussed workflow - presented and tested before on other kinds of data (Hansen et al., 2014) - paves the way to the implementation of 1D probabilistic inversions of ATEM measurements capable to incorporate the complex pieces of geological information available and overcomes many of the difficulties connected with the utilization of efficient 1D approximations.

It is evident that the inclusion of the modelling error would not slowdown the already available (and extremely fast) algorithms for 1D inversions (it does not matter if stochastic or deterministic). Hence, this approach will possibly remain useful also when fully 3D stochastic inversions will be practical; in fact, it will not be possible to consider any forward modelling tool perfect and, consequently, accounting for the modelling error will be, most likely, always beneficial.

It is also worth being highlighted that, at least for the investigated tests, simply a few hundreds of 3D forward simulations are needed to retrieve a robust assessment of $\mathbf{d}_\Delta$ and $\boldsymbol{C}_\Delta$, and, actually, the same estimation for $\mathbf{d}_\Delta$ and $\boldsymbol{C}_\Delta$ can be used, in principle, in any survey characterized by similar conditions (i.e., similar prior). Hence, in those cases, the efforts for the calculation of $\mathbf{d}_\Delta$ and $\boldsymbol{C}_\Delta$ would impact merely the first survey and, clearly, would not increase with the size of the survey. On the contrary, a full 3D inversion requires at least a few tens of iterations (i.e., 3D calculations) for each sounding location; this easily results in thousands of expensive 3D forward simulations. From these considerations, it clearly appears how convenient the proposed approach is. On the other hand, it is probably true that, severely 3D targets will be, in any case, poorly reconstructed by using 1D approaches; however, the proper inclusion of the modelling error will be always useful in correctly estimating the high uncertainty of the 1D reconstruction of 3D inclusions, whereas not taking into account the modelling error will, most likely, lead to wrong solutions that looks (incorrectly) certain.

2.6. Reference

Airo, M.-L., 2015, Geophysical signatures of mineral deposit types in Finland, Geological survey of Finland.

Alpaydin, E., 2020, Introduction to machine learning, MIT press.

Andersen, K. K., Kirkegaard, C., Foged, N., Christiansen, A. V., and Auken, E., 2016, Artificial neural networks for removal of couplings in airborne transient electromagnetic data: Geophysical Prospecting, v. 64, no. 3, p. 741-752.

Auken, E., and Christiansen, A. V., 2004, Layered and laterally constrained 2D inversion of resistivity data: Geophysics, v. 69, no. 3, p. 752-761.

Auken, E., Christiansen, A. V., Kirkegaard, C., Fiandaca, G., Schamper, C., Behroozmand, A. A., Binley, A., Nielsen, E., Effersø, F., and Christensen, N. B., 2015, An overview of a highly versatile forward and stable inverse algorithm for airborne, ground-based and borehole electromagnetic and electric data: Exploration Geophysics, v. 46, no. 3, p. 223-235.

Bai, P., Vignoli, G., and Hansen, T. M., 2021, 1D stochastic inversion of airborne time-domain electromagnetic data with realistic prior and accounting for the forward modeling error: Remote Sensing, 13(19), p.3881.

Bhuiyan, M., and Sacchi, M., Optimization for sparse acquisition, *in* Proceedings 2015 SEG Annual Meeting2015, OnePetro.

Biggio, B., Russu, P., Didaci, L., and Roli, F., 2015, Adversarial biometric recognition: A review on biometric system security from the adversarial machine-learning perspective: IEEE Signal Processing Magazine, v. 32, no. 5, p. 31-41.

Bishop, C. M., 2006, Pattern recognition: Machine learning, v. 128, no. 9.

Brownscombe, W., Ihlenfeld, C., Coppard, J., Hartshorne, C., Klatt, S., Siikaluoma, J., and Herrington, R., 2015, The Sakatti Cu-Ni-PGE sulfide deposit in northern Finland, Mineral deposits of Finland, Elsevier, p. 211-252.

Brykov, M. N., Petryshynets, I., Pruncu, C. I., Efremenko, V. G., Pimenov, D. Y., Giasin, K., Sylenko, S. A., and Wojciechowski, S., 2020, Machine learning modelling and feature engineering in seismology experiment: Sensors, v. 20, no. 15, p. 4228.

Christiansen, A. V., Auken, E., and Viezzoli, A., 2011, Quantification of modeling errors in airborne TEM caused by inaccurate system description: Geophysics, v. 76, no. 1, p. F43-F52.

Constable, S. C., Parker, R. L., and Constable, C. G., 1987, Occam's inversion: A practical algorithm for generating smooth models from electromagnetic sounding data: Geophysics, v. 52, no. 3, p. 289-300.

Cox, L. H., Wilson, G. A., and Zhdanov, M. S., 2010, 3D inversion of airborne electromagnetic data using a moving footprint: Exploration Geophysics, v. 41, no. 4, p. 250-259.

Curtis, A., 1999, Optimal design of focused experiments and surveys: Geophysical Journal International, v. 139, no. 1, p. 205-215.

Dentith, M., and Mudge, S. T., 2014, Geophysics for the mineral exploration geoscientist, Cambridge University Press.

Duda, R. O., Hart, P. E., and Stork, D. G., 2000, Pattern Classification (2nd Edition), Wiley-Interscience.

Dzikunoo, E. A., Vignoli, G., Jørgensen, F., Yidana, S. M., and Banoeng-Yakubo, B., 2020, New regional stratigraphic insights from a 3D geological model of the Nasia sub-basin, Ghana, developed for hydrogeological purposes and based on reprocessed B-field data originally collected for mineral exploration: Solid Earth, v. 11, no. 2, p. 349-361.

Eidsvik, J., Bhattacharjya, D., and Mukerji, T., 2008, Value of information of seismic amplitude and CSEM resistivity: Geophysics, v. 73, no. 4, p. R59-R69.

Goldman, M., Tabarovsky, L., and Rabinovich, M., 1994, On the influence of 3-D structures in the interpretation of transient electromagnetic sounding data: Geophysics, v. 59, no. 6, p. 889-901.

Gunnink, J., Bosch, J., Siemon, B., Roth, B., and Auken, E., 2012, Combining ground-based and airborne EM through Artificial Neural Networks for modelling glacial till under saline groundwater conditions: Hydrology and Earth System Sciences, v. 16, no. 8, p. 3061-3074.

Han, D., Lee, J., Im, J., Sim, S., Lee, S., and Han, H., 2019, A novel framework of detecting convective initiation combining automated sampling, machine learning, and repeated model tuning from geostationary satellite data: Remote Sensing, v. 11, no. 12, p. 1454.

Hansen, T. M., 2021a, Efficient probabilistic inversion using the rejection sampler—exemplified on airborne EM data: Geophysical Journal International, v. 224, no. 1, p. 543-557.

Hansen, T. M., 2021b, Probabilistic inverse problems using machine learning-applied to inversion of airborne EM data.

Hansen, T. M., Cordua, K. S., Jacobsen, B. H., and Mosegaard, K., 2014, Accounting for imperfect forward modeling in geophysical inverse problems—exemplified for crosshole tomography: Geophysics, v. 79, no. 3, p. H1-H21.

Hansen, T. M., Cordua, K. S., Looms, M. C., and Mosegaard, K., 2013, SIPPI: A Matlab toolbox for sampling the solution to inverse problems with complex prior information: Part 2—Application to crosshole GPR tomography: Computers & Geosciences, v. 52, p. 481-492.

Hansen, T. M., and Minsley, B. J., 2019, Inversion of airborne EM data with an explicit choice of prior model: Geophysical Journal International, v. 218, no. 2, p. 1348-1366.

Hauser, J., Gunning, J., and Annetts, D., 2015, Probabilistic inversion of airborne electromagnetic data under spatial constraints: Geophysics, v. 80, no. 2, p. E135-E146.

Hohmann, G. W., 1975, Three-dimensional induced polarization and electromagnetic modeling: Geophysics, v. 40, no. 2, p. 309-324.

Høyer, A.-S., Jørgensen, F., Sandersen, P., Viezzoli, A., and Møller, I., 2015, 3D geological modelling of a complex buried-valley network delineated from borehole and AEM data: Journal of Applied Geophysics, v. 122, p. 94-102.

Høyer, A.-S., Vignoli, G., Hansen, T. M., Vu, L. T., Keefer, D. A., and Jørgensen, F., 2017, Multiple-point statistical simulation for hydrogeological models: 3-D training image development and conditioning strategies: Hydrology and Earth System Sciences, v. 21, no. 12, p. 6069-6089.

Jørgensen, F., and Sandersen, P. B., 2006, Buried and open tunnel valleys in Denmark—erosion beneath multiple ice sheets: Quaternary Science Reviews, v. 25, no. 11-12, p. 1339-1363.

Karshakov, E. V., Podmogov, Y. G., Kertsman, V. M., and Moilanen, J., 2017, Combined frequency domain and time domain airborne data for environmental and engineering challenges: Journal of Environmental and Engineering Geophysics, v. 22, no. 1, p. 1-11.

Kehew, A. E., Piotrowski, J. A., and Jørgensen, F., 2012, Tunnel valleys: Concepts and controversies—A review: Earth-Science Reviews, v. 113, no. 1-2, p. 33-58.

Kesselring, M., Wagner, F., Kirsch, M., Ajjabou, L., and Gloaguen, R., 2020, Development of sustainable test sites for mineral exploration and knowledge spillover for industry: Sustainability, v. 12, no. 5, p. 2016.

Kwan, K., Prikhodko, A., Legault, J. M., Plastow, G. C., Kapetas, J., and Druecker, M., 2016, VTEM airborne EM, aeromagnetic and gamma-ray spectrometric data over the Cerro Quema high sulphidation epithermal gold deposits, Panama: Exploration Geophysics, v. 47, no. 3, p. 179-190.

Latiff, A. H. A., Ghosh, D. P., and Latiff, N. M. a. A., 2017, Optimizing acquisition geometry in shallow gas cloud using particle swarm optimization approach: International Journal of Computational Intelligence Systems, v. 10, no. 1, p. 1198-1210.

Le Ravalec, M., Noetinger, B., and Hu, L. Y., 2000, The FFT moving average (FFT-MA) generator: An efficient numerical method for generating and conditioning Gaussian simulations: Mathematical Geology, v. 32, no. 6, p. 701-723.

Legault, J. M., Izarra, C., Prikhodko, A., Zhao, S., and Saadawi, E. M., 2015, Helicopter EM (ZTEM–VTEM) survey results over the Nuqrah copper–lead–zinc–gold SEDEX massive sulphide deposit in the Western Arabian Shield, Kingdom of Saudi Arabia: Exploration Geophysics, v. 46, no. 1, p. 36-48.

Ley-Cooper, A. Y., Brodie, R. C., and Richardson, M., 2020, AusAEM: Australia's airborne electromagnetic continental-scale acquisition program: Exploration geophysics, v. 51, no. 1, p. 193-202.

Liu, G., and Becker, A., 1990, Two-dimensional mapping of sea-ice keels with airborne electromagnetics: Geophysics, v. 55, no. 2, p. 239-248.

Liu, Y., Starzyk, J. A., and Zhu, Z., 2008, Optimized approximation algorithm in neural networks without overfitting: IEEE transactions on neural networks, v. 19, no. 6, p. 983-995.

Moilanen, E., Karshakov, E., and Volkovitsky, A., Time domain helicopter EM system Equator: Resolution, sensitivity, universality, *in* Proceedings 6th International AEM Conference & Exhibition2013, European Association of Geoscientists & Engineers, p. cp-383-00041.

Mosegaard, K., and Tarantola, A., 1995, Monte Carlo sampling of solutions to inverse problems: Journal of Geophysical Research: Solid Earth, v. 100, no. B7, p. 12431-12447.

Núñez-Nieto, X., Solla, M., Gómez-Pérez, P., and Lorenzo, H., 2014, GPR signal characterization for automated landmine and UXO detection based on machine learning techniques: Remote sensing, v. 6, no. 10, p. 9729-9748.

Oldenburg, D. W., Haber, E., and Shekhtman, R., 2013, Three dimensional inversion of multisource time domain electromagnetic data: Geophysics, v. 78, no. 1, p. E47-E57.

Palacky, G., 1993, Use of airborne electromagnetic methods for resource mapping: Advances in space research, v. 13, no. 11, p. 5-14.

Rymarczyk, T., Kłosowski, G., and Kozłowski, E., 2018, A non-destructive system based on electrical tomography and machine learning to analyze the moisture of buildings: Sensors, v. 18, no. 7, p. 2285.

Siemon, B., Christiansen, A. V., and Auken, E., 2009, A review of helicopter-borne electromagnetic methods for groundwater exploration: Near Surface Geophysics, v. 7, no. 5-6, p. 629-646.

Sørense, K., and Auken, E., 2004, SkyTEM? A new high-resolution helicopter transient electromagnetic system: Exploration Geophysics, v. 35, no. 3, p. 194-202.

Tarantola, A., 2005, Inverse problem theory and methods for model parameter estimation, SIAM.

Tikhonov, A. N., and Arsenin, V. Y., 1977, Solutions of ill-posed problems: New York, v. 1, no. 30, p. 487.

Vallée, M. A., and Smith, R. S., 2009, Application of Occam's inversion to airborne time-domain electromagnetics: The leading edge, v. 28, no. 3, p. 284-287.

Van der Baan, M., and Jutten, C., 2000, Neural networks in geophysical applications: Geophysics, v. 65, no. 4, p. 1032-1047.

Viezzoli, A., Christiansen, A. V., Auken, E., and Sørensen, K., 2008, Quasi-3D modeling of airborne TEM data by spatially constrained inversion: Geophysics, v. 73, no. 3, p. F105-F113.

Vignoli, G., Deiana, R., and Cassiani, G., 2012, Focused inversion of vertical radar profile (VRP) traveltime data: Geophysics, v. 77, no. 1, p. H9-H18.

Vignoli, G., Fiandaca, G., Christiansen, A. V., Kirkegaard, C., and Auken, E., 2015, Sharp spatially constrained inversion with applications to transient electromagnetic data: Geophysical

Prospecting, v. 63, no. 1, p. 243-255.

Vignoli, G., Guillemoteau, J., Barreto, J., and Rossi, M., 2021, Reconstruction, with tunable sparsity levels, of shear wave velocity profiles from surface wave data: Geophysical Journal International, v. 225, no. 3, p. 1935-1951.

Vignoli, G., Sapia, V., Menghini, A., and Viezzoli, A., 2017, Examples of improved inversion of different airborne electromagnetic datasets via sharp regularization: Journal of Environmental and Engineering Geophysics, v. 22, no. 1, p. 51-61.

Volkovitsky, A., and Karshakov, E., Airborne EM systems variety: what is the difference?, *in* Proceedings 6th International AEM Conference & Exhibition2013, European Association of Geoscientists & Engineers, p. cp-383-00014.

Yuan, S., Liu, J., Wang, S., Wang, T., and Shi, P., 2018, Seismic waveform classification and first-break picking using convolution neural networks: IEEE Geoscience and Remote Sensing Letters, v. 15, no. 2, p. 272-276.

Zhang, F., Chan, P. P., Biggio, B., Yeung, D. S., and Roli, F., 2015, Adversarial feature selection against evasion attacks: IEEE transactions on cybernetics, v. 46, no. 3, p. 766-777.

Chapter 3. (Quasi-)real-time inversion of AEM data via artificial neural network

This Chapter is based on the material discussed in the manuscript Bai et al. (2020).
The possibility to have results very quickly after, or even during, the collection of electromagnetic data would be important, not only for quality check purposes, but also for adjusting the location of the proposed flight lines during an airborne time-domain acquisition. This kind of readiness could have a large impact in terms of optimization of the Value of Information of the measurements to be acquired. In addition, the importance of having fast tools for retrieving resistivity models from airborne time-domain data is demonstrated by the fact that Conductivity-Depth Imaging methodologies are still the standard in mineral exploration. In fact, they are extremely computationally efficient, and, at the same time, they preserve a very high lateral resolution. For these reasons, they are often preferred to inversion strategies even if the latter approaches are generally more accurate in terms of proper reconstruction of the depth of the targets and of reliable retrieval of true resistivity values of the subsurface. In this Chapter, we discuss a novel approach, based on neural network techniques, capable of retrieving resistivity models with a quality comparable with the inversion strategy, but in a fraction of the time. We demonstrate the advantages of the proposed novel approach on synthetic and field datasets.

The approach is based on data-driven Machine Learning (ML) algorithms and, specifically, Artificial Neural Networks (ANNs) that potentially combines the advantages of both imaging and inversion as it allows near real-time reconstructions of the resistivity distribution of the subsurface with an accuracy comparable with the physically based inversion. ANNs are clearly not new in the processing of geophysical data (Brykov et al., 2020; Núñez-Nieto et al., 2014; Rymarczyk et al., 2018; Van der Baan and Jutten, 2000; Yuan et al., 2018). However, the attempts to apply them to AEM observations are limited to the data processing (Andersen et al., 2016) and geological interpretation of the geophysical results (Gunnink et al., 2012). In this chapter, we discuss the application of ANNs for the reconstruction of the pseudo-3D electrical resistivity distribution in the subsurface from the data collected during typical AEM surveys. We test the proposed workflow on both synthetic and field datasets and prove that the corresponding results are comparable to an inversion based on a full-nonlinear 1D forward modelling algorithm. Moreover, the main advantage of our approach is that the geophysical model of the subsurface is obtained almost instantaneously on a standard laptop. These levels of accuracy, reconstruction speed, and flexibility could pave the road to real-time adjustments of survey planning. In seismic exploration, it is not unusual that dedicated optimizations of the survey design are performed in order to save significant resources and, at the same time, enhance the value-of-information of the collected data (Bhuiyan and Sacchi, 2015; Curtis, 1999; Latiff et al., 2017). By having at hand the capability to invert the data in real-time, we can think of survey plans adapting while the data are collected. Potentially this can save the time and efforts connected to subsequent data acquisitions (in the AEM case, maybe, ground based) as follow-ups of the original survey.

3.1. Methodology

In the deterministic framework, the inversion problem is solved by minimizing an objective function – Eq.1-1 (see the details in Chapter 1.). In order to have a term of comparison to effectively assess the performances of the alternative approach based on ANN, we consider the 1D deterministic SCI used in Chapter 2. Hence, $\mathbf{m}$ (and consistently also F – see, for example, Eq.2-1 in Chapter 2.) is based on the assumption that (locally) the subsurface is not varying laterally. Therefore, each individual data sounding, and each associated model, is handled independently from the adjacent ones. Still, whereas the forward modelling F is always one dimensional, in the deterministic inversion there is a connection between the neighboring models imposed through the regularization term. Hence, concerning the stabilizer choice, we adopt the probably most common option of $\phi_m(\boldsymbol{m})$ (in Eq.1-1) being equal to the minimum gradient stabilizer:

$$\phi_m(\boldsymbol{m}) = \|\nabla \boldsymbol{m}\|_{L2}^2 \qquad 3\text{-}1$$

Thus, despite the conductivity distribution is considered locally 1D, the stabilizer acts both along the vertical (z) and the horizontal (x) direction, promoting solutions that are laterally coherent (without being truly 2D/3D). This is indeed the essence of the SCI mentioned in Chapter 1. (Vignoli et al., 2015; Vignoli et al., 2017). Moreover, in the 1D deterministic inversion scheme we are using, the value of β is calculated in order to guarantee a chi-squared value:

$$\chi^2 = \left(\frac{1}{N_d}\right) \|\boldsymbol{W}_d(\boldsymbol{d}_{obs} - F(\boldsymbol{m}))\|_{L2}^2 \qquad 3\text{-}2$$

approximately equal 1 (with N_d being the number of time gates) (Vignoli et al., 2012; Vignoli et al., 2021).

The ANN is built in order to perform a similar task with respect to the minimization of objective functional in Eq.1-1. ANNs use continuous and differentiable activation functions at each unit of the network, which makes the network output ($\mathbf{m}$) a continuous and differentiable function of the network input ($\mathbf{d}$); this, in turn, leads to the possibility of defining a continuous and differentiable error function for the evaluation of the difference between the network output and the target output. Consequently, the error function can be minimized over a training set using a relatively simple gradient-based procedure. Hence, the problem of building an effective ANN to map the recorded measurements into resistivity vector is reduced to the minimization of an error functional:

$$E(\boldsymbol{w}) = \|K(\boldsymbol{D}, \boldsymbol{w}) - \boldsymbol{M}\|_{L2'}^2 \qquad 3\text{-}3$$

where $\mathbf{D}$ and $\mathbf{M}$ consist of the elements of the (data, model) couples ($\mathbf{d}_t$, $\mathbf{m}_t$) constituting the Training Dataset (TD) (Bishop, 2006). Of course, in this case, the minimization aims at finding the optimal weights $\mathbf{w}$ of the connections between the network units. Thus, the ANN K is found via the minimization with respect to $\mathbf{w}$. Once K is built based on the TD, it can be applied to the elements dobs of the observed dataset to infer the corresponding conductivity models $\mathbf{m}$. In this respect, it is worth noting that the retrieved K—and, therefore, the corresponding final resistivity distribution obtained via the application of K on the observed data—depends on the selection of the TD. ML approaches are based on the stationarity assumption: the couples in the TD and in the solution, dataset need to be independent and identically distributed (i.i.d.) random variables. In this sense, TD formalizes the available prior information about the studied system. Consistently,

the TD should be selected in order to be representative of the targets (therefore, coherent with our expectations about the geology to be reconstructed) (Alpaydin, 2020; Bishop, 2006). Data stationarity and TD's representativeness are very well-known issues of ML (Han et al., 2019). In a further attempt to reconcile the ANN approach and the (regularized) deterministic inversion, we could think about the selection of the conductivity models for the development of the TD as some sort of regularization: the solution provided by the ANN cannot be too different from the models (and the associated data) used to train the ANN. Hence, for example, the TD should be based on the prior (geological) knowledge available about the investigated area. This might sound tautological, but it is actually the key point of regularization theory (and, clearly, also of ML approaches).

In the present chapter, the ANN consists of a multilayer perceptron with (i) an input layer with 54 (i.e., the number of time gates) units; (ii) three hidden layers with, respectively, 100, 500, 200 units; and (iii) an output layer characterized by 30 (i.e., the number of conductivity model parameters) units. As TD we took the $\mathbf{d}_t$ data generated via the forward modelling F for each of the 1D resistivity models $\mathbf{m}_t$ making up a realistic resistivity section (Figure 3-1). It is important to stress that, despite the apparent lateral coherence of the 1D model, the elements of the TD are, indeed, handled as independent soundings and resistivity models. Plotting the TD data and the models as 2D sections made it easier to assess the representativeness of the (geologically informed) training dataset with respect to the actual measurements to be inverted.

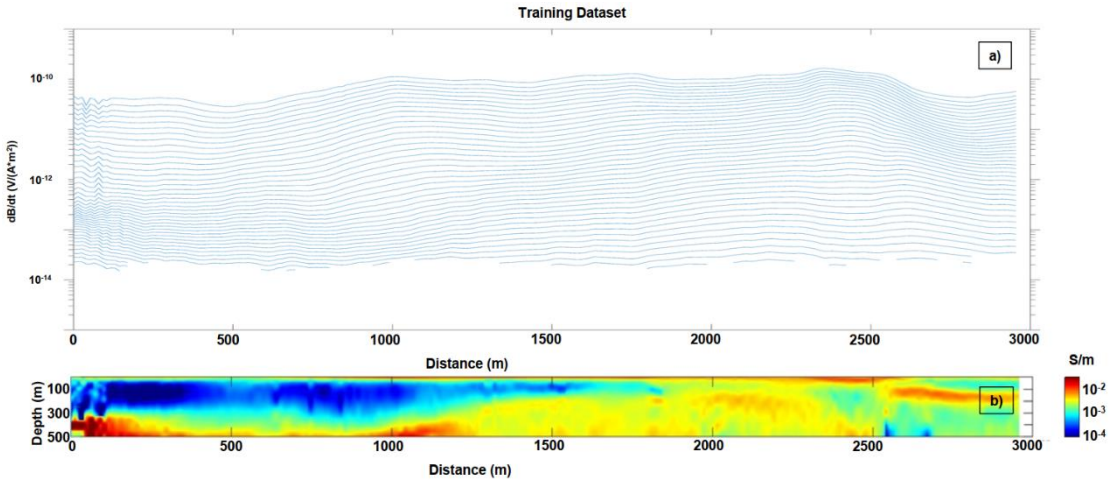

Figure 3-1. Portion of the Training Dataset. Panel (a) shows the airborne time-domain electromagnetic (AEM) responses associated with the 1D models constituting the conductivity section in panel (b).

It is also important to highlight that the TD used in the present research is based on the technical specifications of the particular system used for the experimental data collection. Thus, the $\mathbf{d}_t$'s are calculated from the corresponding $\mathbf{m}_t$'s by using, for example, the waveform and time gates provided by the contractor together with the survey measurements. In total, the utilized TD consisted of around 12,000 ($\mathbf{d}_t$, $\mathbf{m}_t$) couples (a sample of which is plotted in Figure 3-1). In the training phase, a multi-start approach has been adopted to minimize the effect of local minima of the error functional. Additionally, following a standard procedure (Liu et al., 2008), the optimal number of epochs was selected by studying the error functional value when applied on validation subsets (Duda et al., 2000). Differently from the 1D deterministic inversion case (in which the

stabilizing terms connect adjacent 1D models), in the inversion performed through K, no lateral information is included, and the individual soundings are inverted separately. The inclusion of this further piece of knowledge would be surely beneficial (if available) and should be included in future developments.

3.2. Synthetic test: the ANN result vs. the known model

In order to assess the effectiveness of the ANN approach, we applied the neural network (based on the previously discussed TD) to a known verification dataset. Figure 3-2 shows the true conductivity sections whose 1D models were used to generate the noise-free synthetic data to be inverted. Therefore, in short, and by using a neural network lingo, Figure 3-2 (together with its associated data) is our verification dataset. Figure 3-3 consists of the conductivity sections reconstructed via the proposed ANN. In turn, the inferred conductivities (Figure 3-3) have been used to calculate their associated electromagnetic response; the comparison between the original synthetic data and the calculated response is shown, model-by-model, with a red dot (red axis on the right in Figure 3-3). From this data misfit estimation, it is clear that the conductivity distribution recovered by the neural network is generally compatible with the inverted data within 4%.

Considering the retrieved conductivity distribution, the ANN reconstruction captures almost all the features present in the original model. In addition, Figure 3-3 demonstrates that the proposed approach is quite robust as it retrieves the lateral coherence of the conductivity sections despite the individual models are inverted separately. A quantitative assessment of the model agreement between the reconstructed and the original model can be done through the Figure 3-4 showing, in the log-scale, the ratio between the ANN reconstruction and the true model. In general, the values in Figure 3-4 are around one, demonstrating the overall accuracy of the ANN reconstruction. The areas in Figure 3-4 characterized by major discrepancies between the ANN solution and the true model are generally localized at depth (where, in any case, because of the physics of the method, the sensitivity of the data to the conductivity values is lower) and on the right side of the conductivity sections. This is not surprising if we look at the electromagnetic responses. Regarding this, Figure 3-5 shows the original data (blue lines) compared to the calculated measurements (red lines) for each of the sections in Figure 3-2 and Figure 3-3; it is clear that many of the soundings on the right side of the sections are characterized by a smaller number of time gates (indeed, to simulate more realistic conditions, in several of the original soundings, the late time gates have been removed, mimicking what often happens with field noisy observations). Of course, with a reduced number of time gates, the depth at which the conductivity affects the data values is shallower. This is consistent with the larger model misfit on the right side of the panels in Figure 3-4.

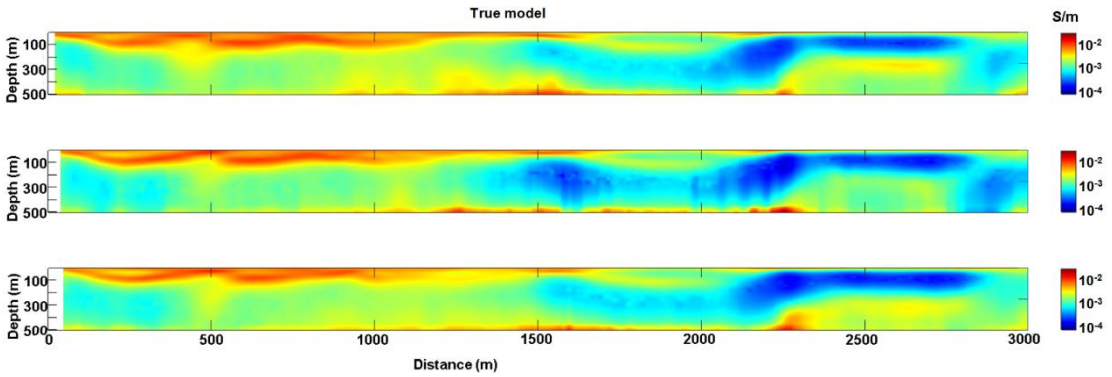

Figure 3-2. The verification dataset. The individual 1D conductivity models of these sections have been used to generate the noise-free synthetic data to be subsequently inverted with the Artificial Neural Networks (ANN) discussed in the section "Methods".

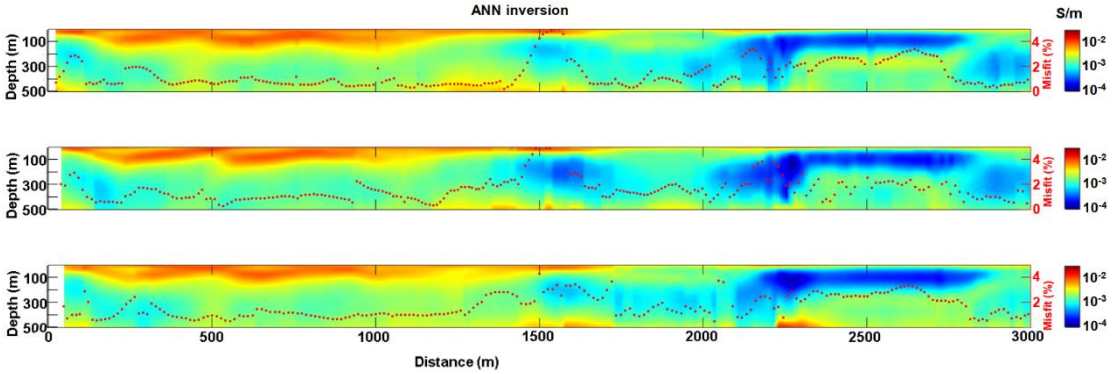

Figure 3-3. The inversion results obtained by applying the ANN trained on the training dataset (TD) in Figure 3-1 to the data generated by the conductive models in Figure 3-2. The data misfit between the calculated and the original measurements is shown for each individual 1D model location as a red dot (the corresponding axis is on the right in red).

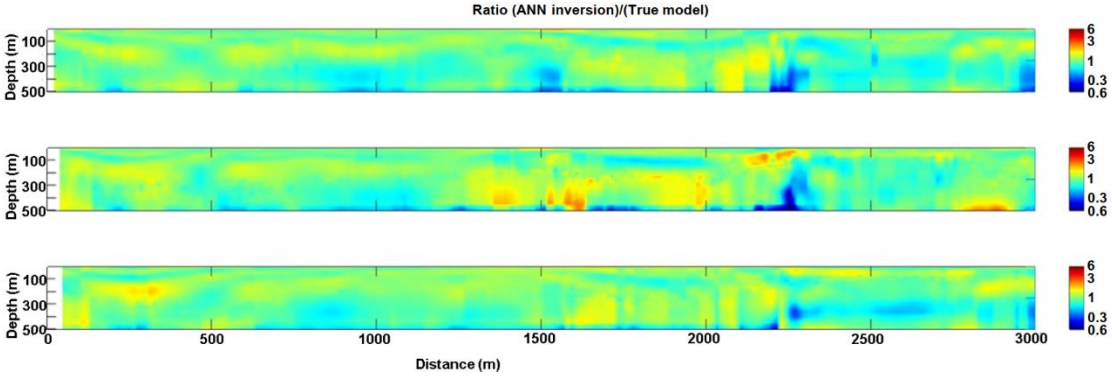

Figure 3-4. The ratio between the conductivity models in Figure 3-3 (the ANN result) and in Figure 3-2 (the true conductivity distribution).

3.3. Field example: the ANN result against the "standard" deterministic inversion

The survey area we investigate is rich in Cu-Ni-PGE (Platinum Group Elements) minerals and has been selected as one of the test sites aiming at the development of cutting-edge technologies for mineral exploration. Time-domain electromagnetic data have been acquired by Geotech using a

VTEM system.

In this section, we compare the results obtained with the ANN—already used for the previous synthetic test and trained on the TD in Figure 3-1—against a more traditional 1D deterministic inversion based on the forward modelling utilized for simulating, for example, the responses in Figure 3-5.

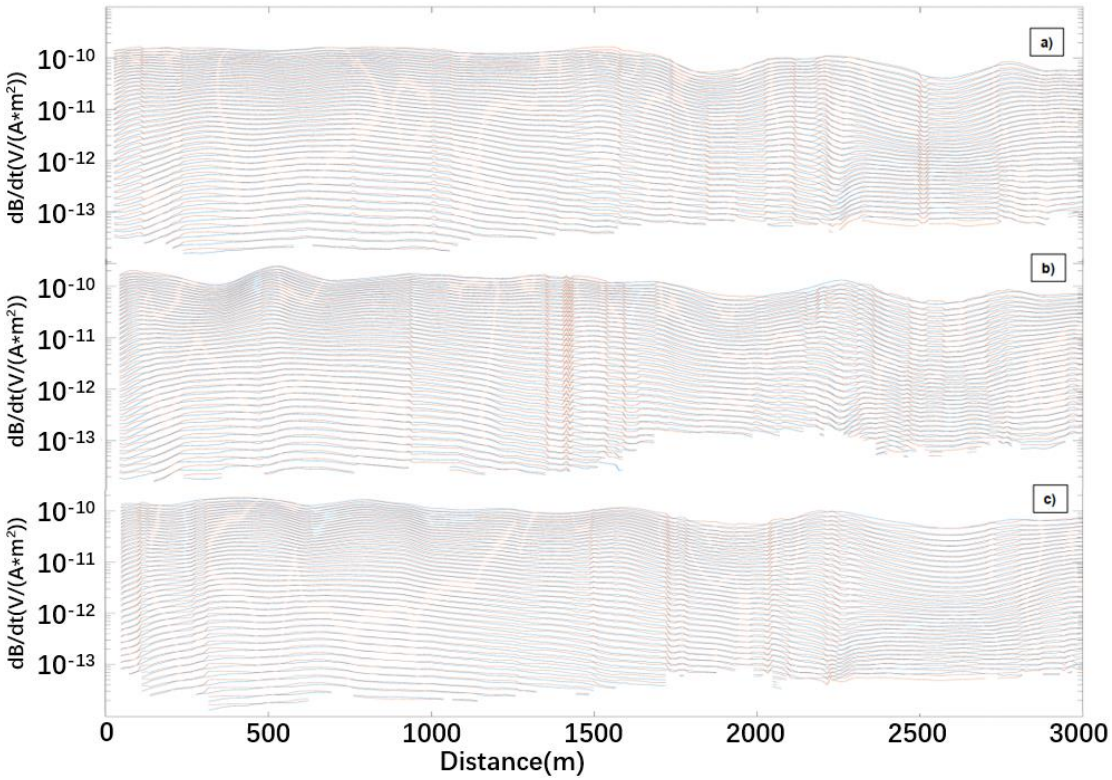

Figure 3-5. Comparison between the synthetic data from the true model in Figure 3-2 (blue lines) and the calculated data from the conductivity sections retrieved by the ANN in Figure 3-3 (red lines). The data in the panels (a–c) in the present figure correspond to the conductivity sections shown in the three panels in each of the Figure 3-2 and Figure 3-3.

Therefore, Figure 3-6 demonstrates that the inversion performed via the developed ANN can infer reasonable 1D models whose responses fit the observation within a 5% threshold (for each model, the data misfit value is represented as a red dot, and the associated red axis is on the right side of the panel). When the ANN result is compared with the corresponding 1D deterministic inversion in Figure 3-7, it is possible to see that the "traditional" deterministic inversion with vertical and lateral smooth constrained is often superior in fitting the data (the data misfit is generally below 2%, as it is clearly visible from the red dots representing the data misfit). Figure 3-8 might be helpful in quantitatively evaluating the differences between the two results as it shows the ratio between the different solutions; it worth noting how the larger discrepancies between the two solutions occur where the data fitting of the deterministic inversion is larger (e.g., between 1850 and 2400 m) and/or in areas characterized by high resistivity values. Therefore, the areas in which also the deterministic inversion has difficulties in fitting the observations and that are characterized by relatively high resistivity values are those where the differences with the ANN solution are more pronounced. This is in agreement with the fact that, in general, AEM methods have difficulties in

accurately distinguish between different high resistivity values.

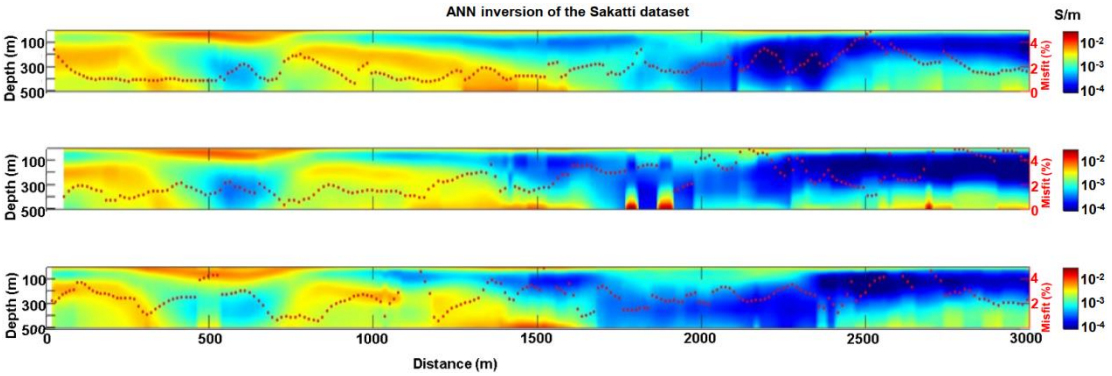

Figure 3-6. The ANN inversion of the field data.

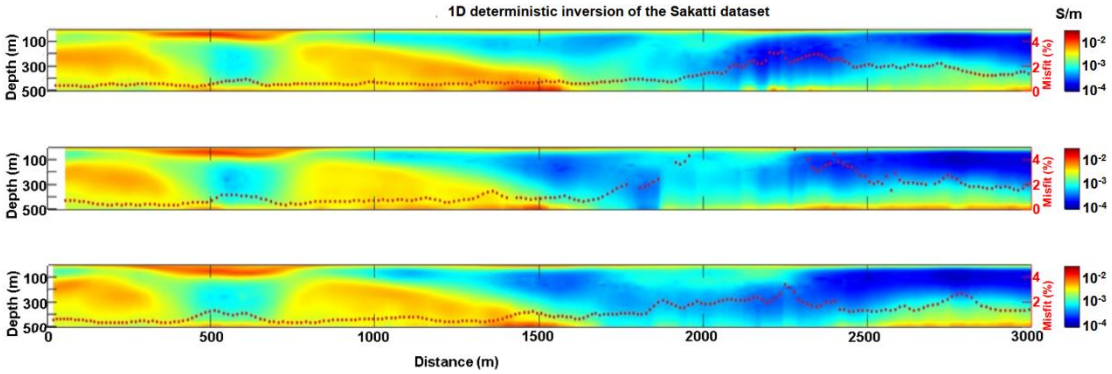

Figure 3-7. The 1D deterministic inversion of the field data.

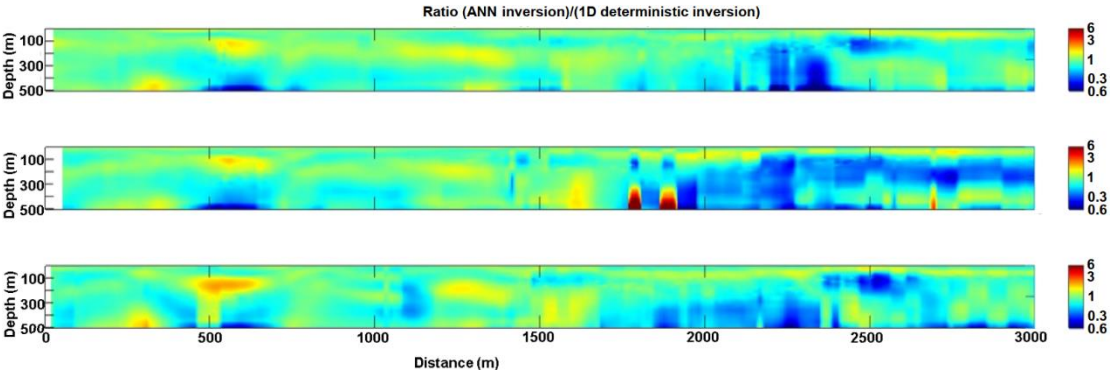

Figure 3-8. The ratio between the conductivity models in Figure 3-6 (the ANN inversion result) and in Figure 3-7 (the deterministic inversion result).

3.4. Summary and discussion

Clearly, the indubitable advantages of the deterministic inversion come at a price: the ANN inversion takes approximately 24 s to invert the entire survey dataset (consisting of 14,346 soundings with 54-time gates each) by using a standard laptop (equipped with an Intel Core i5-8250U processor), whereas hours (so an amount of time of the order of magnitude of 104 s) are necessary to perform the same task by using the 1D deterministic approach and a 64-CPU server. To be fair, it is true that the training phase—crucial for the development of the ANN—requires several hours. Despite that, we believe that the proposed workflow has at least a few main pros:

1. It can allow the optimization of the survey design while the acquisition of the ATEM is on-going. In fact, the development of an effective training dataset and the associate ANN can

be performed before the survey—or it can be even based on the outcomes from the first flight(s) of the survey if the area is assumed to be relatively "stationary"—and, once the ANN is available, reliable results can be almost instantaneously obtained just after each flight. In turn, this can lead to real-time rearrangements of the original tentative survey plans in order to maximize the VoI (Value of Information) of the measurements to be further collected (Eidsvik et al., 2008).

2. The ANN speed can be extremely useful for effective Quality Check (QC) of the data during the survey.
3. The availability of a good starting model (derived from the ANN inversion) can be used to speed-up the 1D deterministic inversion by reducing the number of iterations.

Of course, if, for producing the final results, post-processing analyses are necessary (e.g., in 3D environments), the same will be true also when adopting the proposed ANN approach: ANN based on a 1D forward modelling approach cannot guarantee better results compared with the corresponding deterministic inversion; it can only provide solutions of similar quality within a fraction of the time and by using cheaper computational tools. Moreover, clearly, at least in principle, the presented ANN scheme can be extended in order to also include, for example, induce polarization (IP) effects: it is a matter of incorporating them in the forward modelling algorithm used in the development of the TD. However, as before, we cannot expect the ANN to solve all the issues connected IP in ATEM data. Reasonably, we can only expect to solve the same problem, but much faster.

We present a novel approach to the inversion of airborne time-domain electromagnetic data based on neural networks. We demonstrate the effectiveness of the proposed inversion strategy by testing it on both synthetic and field data. Based on these outcomes, we conclude that the proposed neural network approach is capable of retrieving the conductivity distribution of the subsurface from the measurements collected by the airborne geophysical system with an accuracy that is largely comparable with the most commonly used (in the academia and in the industry) inversion strategies and that relies on 1D deterministic inversion approaches. These results are particularly noticeable as the neural network inversion takes only a fraction of the time required for the deterministic inversion (a few seconds versus hours).

The performances of the neural network discussed in the chapter can be potentially enhanced in terms of data fitting via data augmentation techniques expanding the TD and building more accurate models, provided that effective ways to generate artificial data getting closer to the behavior of the test dataset can be found (Biggio et al., 2015; Zhang et al., 2015). In addition, an aspect that has not been investigated here is the dependence on the training dataset; in future works, studying the robustness of the result as a function of the training dataset would be extremely relevant: after all, the definition of the proper training dataset is a way to include prior (geological) information into the inversion.

Clearly, the neural network strategy discussed in the chapter deals with each sounding independently and does not make use of the possible available knowledge concerning the lateral coherence of the targets; it is a pity not to exploit these additional pieces of information in order

to get even more effective results. In this perspective, pseudo-2D/3D approaches should be explored as well. The dramatic speed up of the inversion by means of the application of the neural network (seconds vs. hours, on a standard laptop) potentially paves the road to on-the-fly inversion with possible applications on real-time survey design optimizations. On the other hand, in the most conservative scenario, the discussed neural network inversion can serve as a starting model for faster deterministic inversions and/or as a QC tool during the data collection phases.

3.5. Reference

Airo, M.-L., 2015, Geophysical signatures of mineral deposit types in Finland, Geological survey of Finland.

Alpaydin, E., 2020, Introduction to machine learning, MIT press.

Andersen, K. K., Kirkegaard, C., Foged, N., Christiansen, A. V., and Auken, E., 2016, Artificial neural networks for removal of couplings in airborne transient electromagnetic data: Geophysical Prospecting, v. 64, no. 3, p. 741-752.

Auken, E., and Christiansen, A. V., 2004, Layered and laterally constrained 2D inversion of resistivity data: Geophysics, v. 69, no. 3, p. 752-761.

Auken, E., Christiansen, A. V., Kirkegaard, C., Fiandaca, G., Schamper, C., Behroozmand, A. A., Binley, A., Nielsen, E., Effersø, F., and Christensen, N. B., 2015, An overview of a highly versatile forward and stable inverse algorithm for airborne, ground-based and borehole electromagnetic and electric data: Exploration Geophysics, v. 46, no. 3, p. 223-235.

Bai, P., Vignoli, G., Viezzoli, A., Nevalainen, J. and Vacca, G., 2020. (Quasi-) Real-Time Inversion of Airborne Time-Domain Electromagnetic Data via Artificial Neural Network. Remote Sensing, 12(20), p.3440.

Bhuiyan, M., and Sacchi, M., Optimization for sparse acquisition, *in* Proceedings 2015 SEG Annual Meeting2015, OnePetro.

Biggio, B., Russu, P., Didaci, L., and Roli, F., 2015, Adversarial biometric recognition: A review on biometric system security from the adversarial machine-learning perspective: IEEE Signal Processing Magazine, v. 32, no. 5, p. 31-41.

Bishop, C. M., 2006, Pattern recognition: Machine learning, v. 128, no. 9.

Brownscombe, W., Ihlenfeld, C., Coppard, J., Hartshorne, C., Klatt, S., Siikaluoma, J., and Herrington, R., 2015, The Sakatti Cu-Ni-PGE sulfide deposit in northern Finland, Mineral deposits of Finland, Elsevier, p. 211-252.

Brykov, M. N., Petryshynets, I., Pruncu, C. I., Efremenko, V. G., Pimenov, D. Y., Giasin, K., Sylenko, S. A., and Wojciechowski, S., 2020, Machine learning modelling and feature engineering in seismology experiment: Sensors, v. 20, no. 15, p. 4228.

Christiansen, A. V., Auken, E., and Viezzoli, A., 2011, Quantification of modeling errors in airborne TEM caused by inaccurate system description: Geophysics, v. 76, no. 1, p. F43-F52.

Constable, S. C., Parker, R. L., and Constable, C. G., 1987, Occam's inversion: A practical algorithm for generating smooth models from electromagnetic sounding data: Geophysics, v. 52, no. 3, p. 289-300.

Cox, L. H., Wilson, G. A., and Zhdanov, M. S., 2010, 3D inversion of airborne electromagnetic data using a moving footprint: Exploration Geophysics, v. 41, no. 4, p. 250-259.

Curtis, A., 1999, Optimal design of focused experiments and surveys: Geophysical Journal International,

v. 139, no. 1, p. 205-215.

Dentith, M., and Mudge, S. T., 2014, Geophysics for the mineral exploration geoscientist, Cambridge University Press.

Duda, R. O., Hart, P. E., and Stork, D. G., 2000, Pattern Classification (2nd Edition), Wiley-Interscience.

Dzikunoo, E. A., Vignoli, G., Jørgensen, F., Yidana, S. M., and Banoeng-Yakubo, B., 2020, New regional stratigraphic insights from a 3D geological model of the Nasia sub-basin, Ghana, developed for hydrogeological purposes and based on reprocessed B-field data originally collected for mineral exploration: Solid Earth, v. 11, no. 2, p. 349-361.

Eidsvik, J., Bhattacharjya, D., and Mukerji, T., 2008, Value of information of seismic amplitude and CSEM resistivity: Geophysics, v. 73, no. 4, p. R59-R69.

Goldman, M., Tabarovsky, L., and Rabinovich, M., 1994, On the influence of 3-D structures in the interpretation of transient electromagnetic sounding data: Geophysics, v. 59, no. 6, p. 889-901.

Gunnink, J., Bosch, J., Siemon, B., Roth, B., and Auken, E., 2012, Combining ground-based and airborne EM through Artificial Neural Networks for modelling glacial till under saline groundwater conditions: Hydrology and Earth System Sciences, v. 16, no. 8, p. 3061-3074.

Han, D., Lee, J., Im, J., Sim, S., Lee, S., and Han, H., 2019, A novel framework of detecting convective initiation combining automated sampling, machine learning, and repeated model tuning from geostationary satellite data: Remote Sensing, v. 11, no. 12, p. 1454.

Hansen, T. M., 2021a, Efficient probabilistic inversion using the rejection sampler—exemplified on airborne EM data: Geophysical Journal International, v. 224, no. 1, p. 543-557.

Hansen, T. M., 2021b, Probabilistic inverse problems using machine learning-applied to inversion of airborne EM data.

Hansen, T. M., Cordua, K. S., Jacobsen, B. H., and Mosegaard, K., 2014, Accounting for imperfect forward modeling in geophysical inverse problems—exemplified for crosshole tomography: Geophysics, v. 79, no. 3, p. H1-H21.

Hansen, T. M., Cordua, K. S., Looms, M. C., and Mosegaard, K., 2013, SIPPI: A Matlab toolbox for sampling the solution to inverse problems with complex prior information: Part 2—Application to crosshole GPR tomography: Computers & Geosciences, v. 52, p. 481-492.

Hansen, T. M., and Minsley, B. J., 2019, Inversion of airborne EM data with an explicit choice of prior model: Geophysical Journal International, v. 218, no. 2, p. 1348-1366.

Hauser, J., Gunning, J., and Annetts, D., 2015, Probabilistic inversion of airborne electromagnetic data under spatial constraints: Geophysics, v. 80, no. 2, p. E135-E146.

Hohmann, G. W., 1975, Three-dimensional induced polarization and electromagnetic modeling: Geophysics, v. 40, no. 2, p. 309-324.

Høyer, A.-S., Jørgensen, F., Sandersen, P., Viezzoli, A., and Møller, I., 2015, 3D geological modelling of a complex buried-valley network delineated from borehole and AEM data: Journal of Applied Geophysics, v. 122, p. 94-102.

Høyer, A.-S., Vignoli, G., Hansen, T. M., Vu, L. T., Keefer, D. A., and Jørgensen, F., 2017, Multiple-point statistical simulation for hydrogeological models: 3-D training image development and conditioning strategies: Hydrology and Earth System Sciences, v. 21, no. 12, p. 6069-6089.

Jørgensen, F., and Sandersen, P. B., 2006, Buried and open tunnel valleys in Denmark—erosion beneath multiple ice sheets: Quaternary Science Reviews, v. 25, no. 11-12, p. 1339-1363.

Karshakov, E. V., Podmogov, Y. G., Kertsman, V. M., and Moilanen, J., 2017, Combined frequency domain and time domain airborne data for environmental and engineering challenges: Journal of

Environmental and Engineering Geophysics, v. 22, no. 1, p. 1-11.

Kehew, A. E., Piotrowski, J. A., and Jørgensen, F., 2012, Tunnel valleys: Concepts and controversies—A review: Earth-Science Reviews, v. 113, no. 1-2, p. 33-58.

Kesselring, M., Wagner, F., Kirsch, M., Ajjabou, L., and Gloaguen, R., 2020, Development of sustainable test sites for mineral exploration and knowledge spillover for industry: Sustainability, v. 12, no. 5, p. 2016.

Kwan, K., Prikhodko, A., Legault, J. M., Plastow, G. C., Kapetas, J., and Druecker, M., 2016, VTEM airborne EM, aeromagnetic and gamma-ray spectrometric data over the Cerro Quema high sulphidation epithermal gold deposits, Panama: Exploration Geophysics, v. 47, no. 3, p. 179-190.

Latiff, A. H. A., Ghosh, D. P., and Latiff, N. M. a. A., 2017, Optimizing acquisition geometry in shallow gas cloud using particle swarm optimization approach: International Journal of Computational Intelligence Systems, v. 10, no. 1, p. 1198-1210.

Le Ravalec, M., Noetinger, B., and Hu, L. Y., 2000, The FFT moving average (FFT-MA) generator: An efficient numerical method for generating and conditioning Gaussian simulations: Mathematical Geology, v. 32, no. 6, p. 701-723.

Legault, J. M., Izarra, C., Prikhodko, A., Zhao, S., and Saadawi, E. M., 2015, Helicopter EM (ZTEM–VTEM) survey results over the Nuqrah copper–lead–zinc–gold SEDEX massive sulphide deposit in the Western Arabian Shield, Kingdom of Saudi Arabia: Exploration Geophysics, v. 46, no. 1, p. 36-48.

Ley-Cooper, A. Y., Brodie, R. C., and Richardson, M., 2020, AusAEM: Australia's airborne electromagnetic continental-scale acquisition program: Exploration geophysics, v. 51, no. 1, p. 193-202.

Liu, G., and Becker, A., 1990, Two-dimensional mapping of sea-ice keels with airborne electromagnetics: Geophysics, v. 55, no. 2, p. 239-248.

Liu, Y., Starzyk, J. A., and Zhu, Z., 2008, Optimized approximation algorithm in neural networks without overfitting: IEEE transactions on neural networks, v. 19, no. 6, p. 983-995.

Moilanen, E., Karshakov, E., and Volkovitsky, A., Time domain helicopter EM system Equator: Resolution, sensitivity, universality, *in* Proceedings 6th International AEM Conference & Exhibition2013, European Association of Geoscientists & Engineers, p. cp-383-00041.

Mosegaard, K., and Tarantola, A., 1995, Monte Carlo sampling of solutions to inverse problems: Journal of Geophysical Research: Solid Earth, v. 100, no. B7, p. 12431-12447.

Núñez-Nieto, X., Solla, M., Gómez-Pérez, P., and Lorenzo, H., 2014, GPR signal characterization for automated landmine and UXO detection based on machine learning techniques: Remote sensing, v. 6, no. 10, p. 9729-9748.

Oldenburg, D. W., Haber, E., and Shekhtman, R., 2013, Three dimensional inversion of multisource time domain electromagnetic data: Geophysics, v. 78, no. 1, p. E47-E57.

Palacky, G., 1993, Use of airborne electromagnetic methods for resource mapping: Advances in space research, v. 13, no. 11, p. 5-14.

Rymarczyk, T., Kłosowski, G., and Kozłowski, E., 2018, A non-destructive system based on electrical tomography and machine learning to analyze the moisture of buildings: Sensors, v. 18, no. 7, p. 2285.

Siemon, B., Christiansen, A. V., and Auken, E., 2009, A review of helicopter‐borne electromagnetic methods for groundwater exploration: Near Surface Geophysics, v. 7, no. 5-6, p. 629-646.

Sørense, K., and Auken, E., 2004, SkyTEM? A new high-resolution helicopter transient electromagnetic system: Exploration Geophysics, v. 35, no. 3, p. 194-202.

Tarantola, A., 2005, Inverse problem theory and methods for model parameter estimation, SIAM.

Tikhonov, A. N., and Arsenin, V. Y., 1977, Solutions of ill-posed problems: New York, v. 1, no. 30, p. 487.

Vallée, M. A., and Smith, R. S., 2009, Application of Occam's inversion to airborne time-domain electromagnetics: The leading edge, v. 28, no. 3, p. 284-287.

Van der Baan, M., and Jutten, C., 2000, Neural networks in geophysical applications: Geophysics, v. 65, no. 4, p. 1032-1047.

Viezzoli, A., Christiansen, A. V., Auken, E., and Sørensen, K., 2008, Quasi-3D modeling of airborne TEM data by spatially constrained inversion: Geophysics, v. 73, no. 3, p. F105-F113.

Vignoli, G., Deiana, R., and Cassiani, G., 2012, Focused inversion of vertical radar profile (VRP) traveltime data: Geophysics, v. 77, no. 1, p. H9-H18.

Vignoli, G., Fiandaca, G., Christiansen, A. V., Kirkegaard, C., and Auken, E., 2015, Sharp spatially constrained inversion with applications to transient electromagnetic data: Geophysical Prospecting, v. 63, no. 1, p. 243-255.

Vignoli, G., Guillemoteau, J., Barreto, J., and Rossi, M., 2021, Reconstruction, with tunable sparsity levels, of shear wave velocity profiles from surface wave data: Geophysical Journal International, v. 225, no. 3, p. 1935-1951.

Vignoli, G., Sapia, V., Menghini, A., and Viezzoli, A., 2017, Examples of improved inversion of different airborne electromagnetic datasets via sharp regularization: Journal of Environmental and Engineering Geophysics, v. 22, no. 1, p. 51-61.

Volkovitsky, A., and Karshakov, E., Airborne EM systems variety: what is the difference?, *in* Proceedings 6th International AEM Conference & Exhibition2013, European Association of Geoscientists & Engineers, p. cp-383-00014.

Yuan, S., Liu, J., Wang, S., Wang, T., and Shi, P., 2018, Seismic waveform classification and first-break picking using convolution neural networks: IEEE Geoscience and Remote Sensing Letters, v. 15, no. 2, p. 272-276.

Zhang, F., Chan, P. P., Biggio, B., Yeung, D. S., and Roli, F., 2015, Adversarial feature selection against evasion attacks: IEEE transactions on cybernetics, v. 46, no. 3, p. 766-777.

Chapter 4. Conclusions

The initial goal of this thesis was the development of a 3D stochastic inversion algorithm for massive airborne time-domain datasets. This is clearly an overwhelming task, especially for a PhD program. So, our expectations had to be lowered. Still, the implementation and availability of a 3D forward modelling allowed us to incorporate into existing 1D inversion frameworks the assessment of the modelling error that inevitably contaminates the inversion process.

Since the assessment of the modelling error is based on available geological information and it basically consists of the prior to be used in stochastic frameworks, we decided to exploit the full potential of probabilistic approaches in which samples of the prior distribution are used: 1) for the construction of the modelling error and 2) to feed the stochastic inversion.

In the present thesis, through two synthetic and one field test, the effectiveness of the proposed methodology is discussed and verified. The results with respect to the more standard deterministic inversion based on Occam's regularization are significant. This is true also with respect to the stochastic inversion performed without including the modelling error assessment demonstrating that it is not only a matter of selecting the correct prior (but is also a matter of exploiting the full information content connected with that prior, namely, the associated modelling error).

In short, we can conclude that:

1. when inverting measurements collected in complex 3D geological regions, the effect of approximate forward modelling cannot be ignored;
2. stochastic inversion approaches can be very useful in incorporating complex prior information otherwise very difficult to be formalized in deterministic frameworks (in this respect, please, compare the complexity of the prior samples in Chapter 2 with respect to simple smooth or sharp spatial constraints of the regularized inversions); still, to fully use the information of the prior, we need to include the assessment of the modelling error associated with that prior (and, clearly, with the forward modelling used for the actual inversion);
3. Without including modelling error, the inversion might be able to fit the data very well, but in doing that it will also fit the coherent noise connected with the dimensionality of the target; this will lead to apparently very well resolved features that are, indeed, just artifacts;
4. Incorporating the modelling error is a step towards 3D stochastic inversion, and, still, even when efficient 3D forward modelling tools will be available, as they will always be approximations, our framework can be useful in avoiding data misinterpretations.

Together with the advancements on the inversion side, in order to cope with the impeding computational costs of the 3D forward, we tried to develop extremely efficient inversion schemes based on Neural Networks. Preliminary tests on 1D inversion are very promising and outperform the state-of-the-art deterministic inversion by several orders of magnitude (tens of seconds against tens of hours). It is clear that the stochastic inversion and the neural network approach rely on similar principles: after all the prior and the training dataset concepts are not that different.

Concerning this second part of the thesis, the conclusions that can be drawn can be:

1. Based on the outcomes from previous surveys or even from the first flight(s) of an on-going survey (under the assumption that the investigated area is relatively “stationary”), the proposed Neural Network can be trained. In turn, the obtained Neural Network can invert the just acquired airborne electromagnetic data almost real-time; hence, even during the collection process. Therefore, the proposed Neural Network inversion can allow the optimization of the survey design while the acquisition of the airborne data is on-going (literally, on the fly).
2. The fast and high-quality Neural Network inversion can be effectively used for the Quality Check of the data during the data acquisition.
3. In the most conservative scenarios, the Neural Network inversion results could be utilized as a good initial model for the 1D deterministic inversion; this can shorten the deterministic inversion time by reducing the overall iterations number.

Acknowledgement

At the end of my Ph.D., I would like to thank an important person in my life – my supervisor, dear Dr. Giulio Vignoli. I remember, at the beginning of my Ph.D., I often fell into clueless, tedious tests, very rarely get the expected experimental results. Giulio told me do the tests step by step following a designed plan and be organized when you finished the tests. After one and half year, I just could conduct tests effectively. Due to my poor English and expression ability, I often failed express my tests clearly and correctly when giving reports in front of people. Giulio modified the presentations for me time by time patiently, helped me organize the lines word by word, and listened to my practice tirelessly. Moreover, many times, he helped me a lot in small things, such as writing emails, and I learned a lot from them.

In terms of research, he always respected and encouraged my ideas, and let me realize my ideas as much as possible. Also, he often held meetings for me with other tutors to discuss our research results. Nevertheless, my achievements and all of published papers are based on his original ideas, and follow his guide step by step. In terms of life, he also helped me a lot, especially when I was sick. In short, he spent huge energy, time and even money on me. The word “thanks” cannot fully express my feelings.

Second, I would like to thank one of my co-tutors, Dr. Thomas Mejer Hansen. From his papers, I learned the basics of my Ph.D. project, and my implementation is based on his code. He taught me a lot of practical skills, such as how to build a Gaussian 3D model, and give me a lot of advice on the parameters of the 3D model.

The third, I would like to thank my other co-tutor, Dr. Andrea Viezzoli. He provides me an important field data. All my field tests are based on those high-quality data that are very suitable for my research. Furthermore, I am deeply impressed by his friendliness and enthusiasm, and very happy to communicate with him face to face.

Last but not the least, I want to thank all my classmates, roommates and friends, especially, Jeniffer Barreto. They helped me in many ways, especially how to survive abroad. They encouraged me a lot, especially when I was depressed and give me a lot of inspiration when my research fell into confusion.

If this thesis is a small apple, I am the short apple tree surrounded by sunshine, air, water, and soil. Without the support of all these kind people, I wouldn’t be able to complete the thesis. At this moment, I want to thank you, all of you.

La borsa di dottorato è stata cofinanziata con risorse del
Programma Operativo Nazionale Ricerca e Innovazione 2014-2020 (CCI 2014IT16M2OP005),
Fondo Sociale Europeo, Azione I.1 “Dottorati Innovativi con caratterizzazione Industriale”

UNIONE EUROPEA
Fondo Sociale Europeo